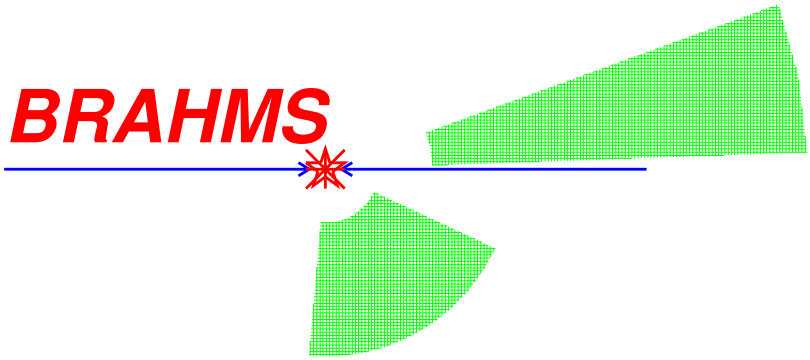

Conceptual Design Report

October 1994

Forward Angle and Midrapidity Hadron Spectrometers at RHIC

The BRAHMS collaboration

K. Ashktorab, D. Beavis, C. Chasman, Z. Chen, Y.Y. Chu, R. Debbe, M. Gonin,
S. Gushue, J.H. Lee, M.J. LeVine, B. Moskowitz, J.W. Olness,
L.P. Remsberg, F. Videbaek and F.Zhu
Brookhaven National Laboratory, Upton, NY 11973

J.-P. Coffin, P. Fintz, G. Guillaume, F. Jundt,
C. Maazouzi, F. Rami and P. Wagner
Centre de Recherches Nucleaires, Strasbourg, FRANCE

J.P. Bondorf, H. Bøggild, J.J. Gaardhøje and O. Hansen
Niels Bohr Institute for Astronomy,Physics and Geophysics
University of Copenhagen, DENMARK

Cheng-lie Jiang
China Institute of Atomic Energy, Beijing, CHINA

B. Budick
Physics Department, New York University, NY 10003

K. Hagel, J. Natowitz and R. Wada
Texas A&M University, College Station, TX 77843-3366

H.J. Crawford and J. Engelage
Space Sciences Laboratory, University of California, Berkeley, CA 94720

Individual participation
D. Roehrich (University of Frankfurt)

Contents

1 Introduction **7**

2 Physics Overview **9**
- 2.1 Motivation . . . 10
- 2.2 Physics Goals and Experimental Criteria . . . 12
- 2.3 Pair Correlations . . . 14
- 2.4 $\phi(1020)$ Measurement . . . 15
- 2.5 References . . . 17

3 Detector Overview **19**
- 3.1 Forward Spectrometer . . . 19
- 3.2 Midrapidity Spectrometer . . . 21
- 3.3 Rapidity Coverage . . . 21
- 3.4 Global detectors . . . 23

4 Magnets **25**
- 4.1 Design Features . . . 26
- 4.2 Estimated Costs . . . 26
- 4.3 Magnet Support Carriages . . . 27

5 Facilities and Experimental Layout **35**
- 5.1 Shielding layout . . . 36
- 5.2 Support Buildings . . . 37
- 5.3 RF cavities and the experiment . . . 37
- 5.4 Beam Pipe . . . 40
- 5.5 Utilities . . . 41
- 5.6 4 O'clock Facilities and Improvements . . . 41
- 5.7 2 O'clock Facility . . . 42

6 Tracking **45**
6.1 Forward Spectrometer . . . 45
6.1.1 General tracking considerations . . . 46
6.1.2 Tracking Detectors . . . 51
6.2 Midrapidity Spectrometer . . . 53
6.3 Time Projection Chambers . . . 55
6.3.1 Design of the Midrapidity TPC's . . . 55
6.3.2 Electronics . . . 59
6.3.3 TPC Characteristics . . . 61
6.3.4 TPC Simulations . . . 62
6.3.5 Present Status . . . 66

7 Particle Identification **69**
7.1 Forward spectrometer . . . 69
7.2 Midrapidity spectrometer . . . 72
7.3 Time-of-flight . . . 73
7.3.1 TOFW design . . . 73
7.3.2 TOF tests . . . 74
7.4 RICH detector . . . 75
7.4.1 Design Requirements and Detector Performance . . . 77
7.4.2 Expected performance . . . 82
7.5 References . . . 83

8 Global Detectors **85**
8.1 Beam-Beam Counters . . . 85
8.2 Centrality detector . . . 87
8.2.1 Phase-space Coverage . . . 88
8.2.2 Concept for a Silicon Strip Detector . . . 90
8.2.3 The Backup Option: A Gas Proportional Counter . . . 94
8.2.4 Potential Upgrades . . . 94
8.3 References . . . 96

9 Data Acquisition and Triggers **97**
9.1 Data Acquisition . . . 97
9.2 Triggers . . . 100

10 Cost and Schedule **103**
10.1 Cost . . . 103
10.2 Schedule . . . 104

A Prototype RICH Test Results **109**
A.1 The Multi-anode PMT 109
A.2 PMT Single-photon Response 110
A.3 The Test Box 110
A.4 Gas Handling System 112
A.5 In-Beam Testing 112

B Simulation programs **117**

C Rate Estimates **119**

Chapter 1

Introduction

The Broad RAnge Hadron Magnetic Spectrometers experiment (BRAHMS) is designed to measure charged hadrons over a wide range of rapidity and transverse momentum for all available beams and energies.

One of the physics goals is to study the reaction mechanisms of the relativistic heavy ion reactions at RHIC energies and the properties of the highly excited nuclear matter formed in these reactions. The amount of stopping will be studied through the net baryon distributions. The expansion and freeze-out characteristics of the hot nuclear system formed in the reaction will be established by studying the spectral shapes and particle abundances. At higher p_t values (1-2.5 GeV/c) the measurements will give insight into the earlier reaction phases through the properties of the hadron spectra. Some information concerning the space-time characteristics of the system will be obtained from interferometry measurements in a limited rapidity and p_t range.

Another goal is to look for evidence of the QGP phase transition as it may manifest itself in the final hadronic stages, e.g. through study of the $< p_t >$ dependence on centrality, and the strange particle production via K^+ and K^-, both in the relatively baryon free mid-rapidity region and in the baryon rich fragmentation region. These goals are achieved by using two small solid angle spectrometers which operate from $2^o - 20^o$ and $20^o - 90^o$, respectively. The rapidity range will be from 0 to 4 with p_t up to 2.5 GeV/c over most of this y range. A measure of the centrality of the collisions will be obtained from a multiplicity array.

This conceptual design report describes the BRAHMS detector and how it will be installed and operated at RHIC. Chapter 2 presents an overview of the physics program to be achieved with the BRAHMS Experiment. This is an extended text of what was given previously in Letter of Intent #8 from January 1992. This is followed in Chapter 3 by an overview of the detector systems, a description which is close to earlier designs

but changed to reflect updates.

The magnet design is reviewed in Chapter 4. Considerable work has gone into a more detailed study of the magnets in the forward arm spectrometer. These studies have confirmed the design originally proposed in LOI8. A detailed first-design of all magnets has been completed.

Chapter 5 describes the requirements that the BRAHMS Experiment sets for the intersection region. The arguments for the proposed positioning of the two magnet arms are presented. The needed support buildings and their possible placements are discussed.

Chapter 6 examines the requirements on the elements of the forward arm, and demonstrates the feasibility of the proposed combination of magnets and tracking detectors. Most of the detectors are small TPC's, and several features of a prototype TPC and the testing thereof are described.

The particle identification in BRAHMS is achieved by time-of-flight techniques and Čerenkov counters. This is described in Chapter 7. It is shown that a RICH detector is well suited to and capable of handling the high momentum particle identification.

The global detectors, i.e., the beam-beam counters and the multiplicity detector, are described next in Chapter 8. The concept for a centrality detector based on silicon strips is presented; a backup scheme employs an array of proportional gas counters.

Considerations on data aquisition and triggers, as given next in Chapter 9, are fairly conventional and should not pose any major problems for development.

The cost estimate for the experiment is given last; the total budget for BRAHMS is within the original goal. Conservative cost estimates have been used throughout. The schedule for construction has yet to be worked out in detail. Attention is drawn to the need for the larger magnets to be procured in FY96 in order to be installed before RHIC commissioning in the fall of 1998.

Chapter 2

Physics Overview

As a consequence of the presently accepted theory of strong interactions it is expected that a deconfined state of quark and gluon matter, the quark–gluon plasma, exists. Such a plasma should occur over a broad range in density and temperature. The underlying mechanism that brings about this deconfined state is the screening of the color field, not unlike the Debye screening of the electric field in a solid. QCD lattice calculations confirm the existence of a well defined phase transition signaling the onset of this state.

It is generally conjectured that the quark–gluon plasma may be created in high energy nucleus–nucleus collisions under a broad range of conditions which are bounded in one direction by high baryon density and low temperature, and in the other by zero net baryon density and temperatures above the Hagedorn limit. The first situation, according to current wisdom, is appropriate to the stopping regime of up to $\sqrt{s}$ $\approx$10 GeV per pair of nucleons, where stopping of the projectile results in high baryon and energy density. This regime is now being studied in the heavy ion fixed target experiments at the AGS and the CERN–SPS.

The creation of the baryon–poor, high–temperature plasma, on the other hand, depends on attaining collision energies far above the stopping regime. The colliding nuclei will then pass through one another and the baryon-rich regions will be close to the original nuclei in rapidity. After the collision has occurred, a strong color field is created in the space between the nuclei which is anticipated to create a quark–gluon plasma with about an equal number of baryons and anti-baryons. It may be pointed out that while the phase transition to the quark–gluon plasma with zero net baryon density has been modeled in lattice QCD calculations, this has not as yet been possible for the baryon-rich situation. The phase transition to the plasma is expected to be more likely for central collisions, with most of the colliding nucleons participating in the process, while peripheral collisions should behave more like elementary nucleon–nucleon interactions.

At RHIC opportunities exists for experiments investigating both the relatively baryon–poor quark-gluon plasma in the midrapidity region and the baryon-rich plasma in the fragmentation regions of rapidity.

2.1 Motivation

The most basic information available for understanding the phenomena that occur in heavy ion collisions comes from the momentum spectra and yields of the various emitted particles as a function of transverse momentum, p_t, and rapidity, y. It is one goal of this experiment to measure these spectra in the kinematic regions in which they are most sensitive to model predictions. Particle yields, as a function of y, are important indicators of the densities obtained in the collisions and of the produced entropy. The spectral shapes and slopes and their y-dependence reveal the reaction dynamics and the degree of thermalization attained. The high p_t parts of the spectra are indicators of the early phases of the reaction. Enhancement of strangeness and/or antibaryons may signal the creation of the quark–gluon plasma.

As an example of the importance of these measurements, the expectations for the "baryon free" region for Au+Au central collisions at RHIC are compared for three different calculations, all of which are based in part on theoretical string models and in part on scaling from p+p data, particularly from the CERN ISR ($\sqrt{s} = 64$ GeV.) Plotted in Fig. 2.1 is the rapidity density for the net baryon number, namely the multiplicity of $\mathrm{p} - \bar{\mathrm{p}} + \mathrm{n} - \bar{\mathrm{n}}$ (after all unstable particles have decayed).

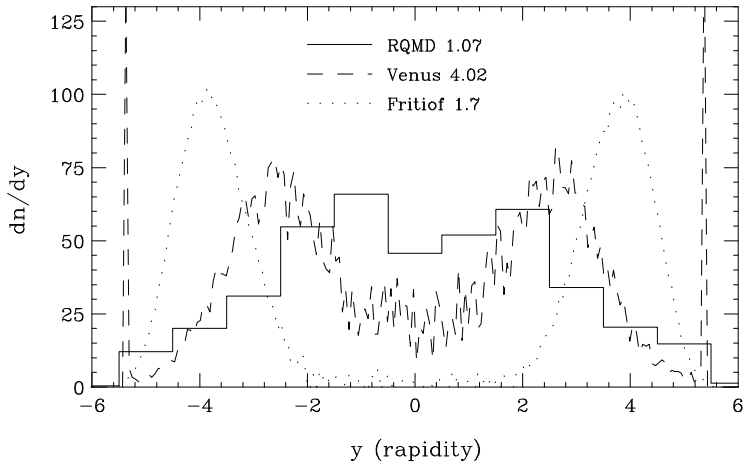

Figure 2.1: Net baryons from central Au+Au collisions

The FRITIOF 1.7 model[1], which describes the p+p data of the ISR quite well, pre-

dicts a flat, baryon-poor region in midrapidity for central Au+Au collisions at RHIC, and peaks at $y = \pm 3.8$, shifted 1.6 units from the beam rapidity of ± 5.4. The prediction of the VENUS 4.02 code[2] for the same system is dramatically different from FRITIOF, showing no baryon free region, and smaller peaks at $y = \pm 2.6$. Thus the increased "stopping" inherent in VENUS has spread the colliding baryons over the whole rapidity region. RQMD[3] is a transport model which also incorporates a string breaking scheme. It predicts[4] even more piling up of net baryon number at midrapidity than does VENUS. Thus this important indicator of baryon density is very much model-dependent, emphasizing the need for measurements in as broad a rapidity range as possible.

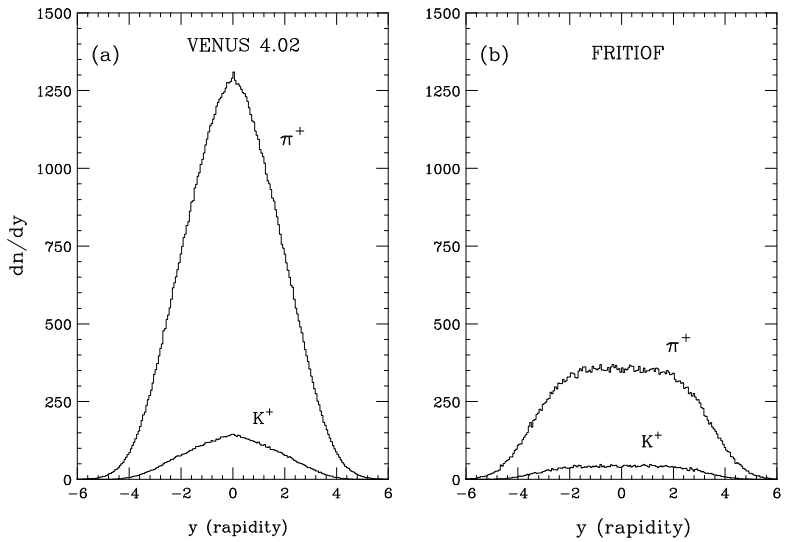

Figure 2.2: Distributions of dn/dy for positive pions and kaons in central Au+Au collisions

Figure 2.2 shows a comparison of the rapidity distributions for π^+ and K^+ mesons, from VENUS (Fig. 2.2a), and from FRITIOF (Fig. 2.2b). Again FRITIOF yields a flat, boost-invariant, midrapidity region, while VENUS predicts distributions that are nowhere flat. Also the overall π^+ multiplicity is larger in VENUS by a factor of 2. In the VENUS model the baryon and energy densities change with rapidity over the entire range, and hence the physics of the collision system also depends on rapidity.

This discussion has shown the importance of measuring the actual rapidity dependence of the baryon and meson yields, but equally strong arguments can be made for also measuring the baryon and meson p_t distributions over as wide a range of rapidity as possible. Furthermore, it is important to systematically study these distributions as a function of the mass of the projectiles as well as the violence (impact parameter) of the collision. Such information is critically needed to establish constraints on the theoretical models and for understanding the basic physical processes for heavy ion collisions at

RHIC.

Global measurements of charged particles give information on the multiplicity density, and thus the energy density achieved in the reactions. It is anticipated that a sufficiently large density, which is a necessary condition for the formation of QGP, can be reached in central Au+Au collisions at RHIC. Thus the multiplicity information is an integral part of the measurements of the hadronic spectra in the BRAHMS Experiment. As an example of this, the dependence of $< p_t >$ on $dN/d\eta$ may signal a phase transition (Ref. 6).

2.2 Physics Goals and Experimental Criteria

In the present section the physics motivation is translated into performance criteria for the Forward and Midrapidity Spectrometers of BRAHMS. The required rapidity and p_t coverages come in part from model calculations and in part from extrapolations of p+p data, particularly from the ISR. The spectrometers are designed so as to handle the predictions from the models in terms of both kinematical coverage and particle densities in the detectors, and have a considerable safety margin.

The criterion adopted for the selection of a forward rapidity limit for created particles is that the measurements should extend over a sufficiently large range that the predicted distributions change by at least a factor of two from their midrapidity values. For protons the maximum rapidity is chosen to be $y = 3.5$. Although it is desirable to come closer to $y = 4$, the technical difficulties are formidable because of the extreme forward angles needed ($\theta \approx 1^\circ$). The more realistic limit of $y = 3.5$ is a compromise which will certainly allow us to establish the trend of the net proton multiplicity $< p > - < \bar{p} >$ at large rapidities.

As mentioned above (see Figs. 2.1 and 2.2) the models predict rapidity distributions which vary from a flat midrapidity plateau to distributions which change over the whole rapidity range. It is thus critically important to measure the complete rapidity distribution (down to $y = 0$) under the same trigger conditions.

At each rapidity the accepted p_t range should be at least large enough to determine the integral over the $dN/d(p_t^2)$ distribution to good accuracy (5%) and to determine the shape of the spectrum (i.e., its slope). In addition, it is desirable to have enough range (and counting statistics) to observe deviations from the shape expected from p+p collisions; this is exponential at low p_t and a power law at larger values (Ref. 7). Model predictions are used to judge the p_t coverage needed. Figure 2.3 shows some momentum spectra at selected angles, 3°, 5°, 15°, 25°, 45°, and 90°, for Au+Au$\rightarrow \pi^+ + X$ and p+X, all from VENUS.

The cross section integrals are determined sufficiently by measurements to ≈ 2 times the mean value in p_t, while a good determination of the shape requires a measurement down to $\approx 10^{-2}$ of the maximum of the distribution and thus sets the wider range. At

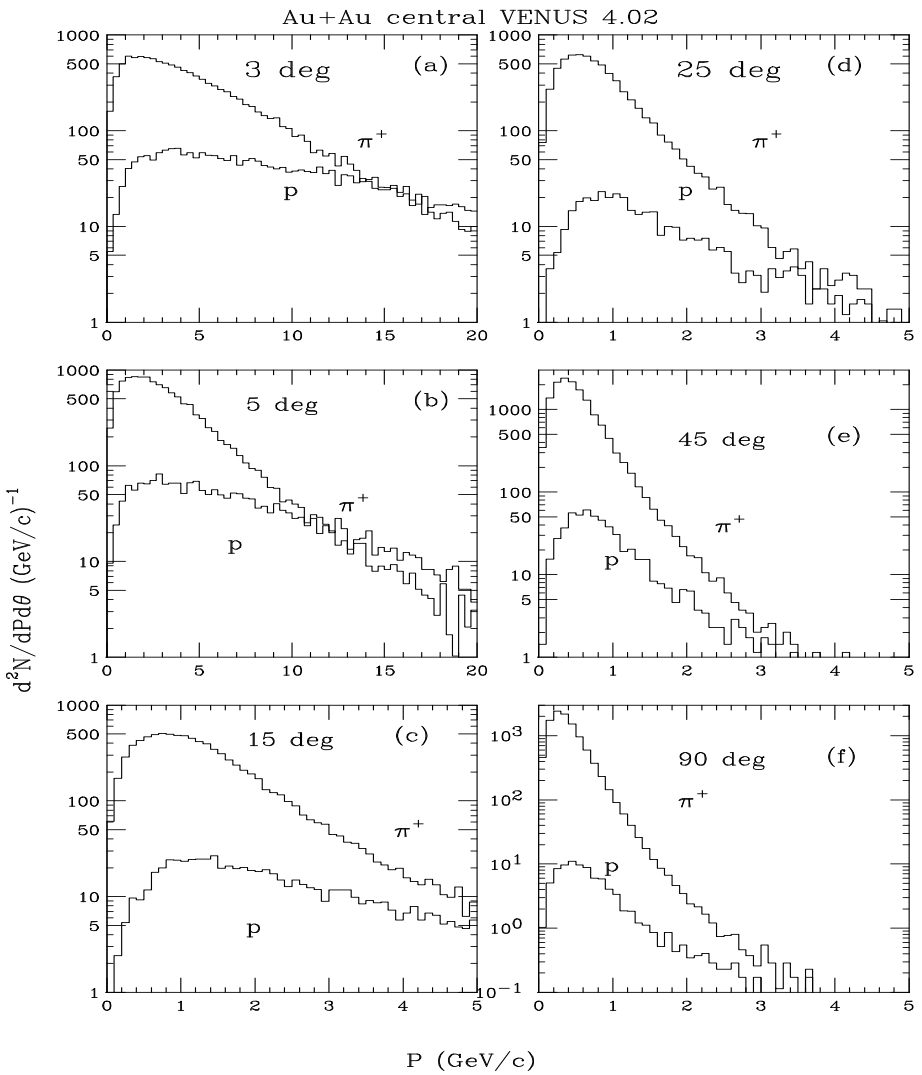

Figure 2.3: $d^2n/dpd\theta$ for several angle settings in central Au+Au collisions

5° the slope criterion gives a required maximum momentum of ≈ 17 GeV/c for π^+ and a corresponding value for protons of ≈25 GeV/c. Generally, the momentum range thus determined varies roughly as $\approx 1/\sin\theta$ and corresponds to a p_t–range that is independent of angle (and rapidity). The most difficult cases, e.g., a 25 GeV/c particle at 2°, will have p_t ≈1.5 GeV/c, corresponding to an invariant cross section that is between 2 and 3 orders of magnitude down from the maximum (using a slope parameter of 250 GeV/c). However, it is emphasized that apart from the very forward angles (2°–3°) the p_t range of the instrument is much larger than 1.5 GeV/c. At 10°, e.g., p_t up to 4.3 GeV/c can be measured. The instrumental limit is in momentum, not in transverse momentum. At

90° the acceptance can be up to a p_t of 5 GeV/c.

It is difficult to establish a criterion for the lower value of measurement in p_t. To avoid missing important spectral components it should be as low as possible. Momenta of $\simeq$2 GeV/c for protons and pions can be measured at forward angles, which leads to the very low p_t cutoff of $\simeq$100 MeV/c. At midrapidity the low momentum limit is determined more by identification problems due to decay losses, multiple scattering and energy losses. It can be $\sim$100 MeV/c for pions.

The measurement of composite baryons and in particular anti-baryons ($\bar{\mathrm{d}}$, $\bar{\mathrm{t}}$, and $^3\bar{\mathrm{He}}$) is possible in BRAHMS. The latter may constitute a very sensitive probe of the production of nonstrange anti-baryons through the mechanism of coalescence.

2.3 Pair Correlations

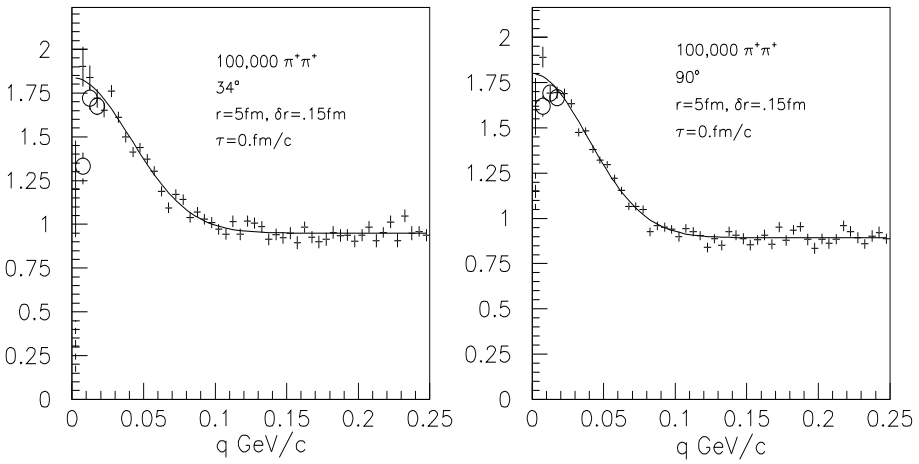

Figure 2.4: The $\pi^+\pi^+$ correlation function for the midrapidity spectrometer at 34 and 90°. The open circles at small q show the distortion caused if all pairs are lost with a spatial separation less than 1 cm in the front TPC.

The correlation of like-bosons as a function of relative momentum can provide a measure of the space-time structure of the emission source. Measurement of spatial source size combined with particle spectra and yields can provide insight into the dynamics which controlled the evolution from an initial hot dense phase to the final hadronized state. To illustrate the capability of the midrapidity spectrometer to measure like-boson correlations, we have simulated a Gaussian source with a radius of 5 fm and a lifetime of 0 fm/c. Figure 2.4 shows the resultant correlation functions obtained from π^+ pairs with the spectrometer at 34° and 90°. It is expected that a correlation function of 100,000

like sign pairs could be obtained in less than eight hours. Figure 2.5 shows the correlation function obtained from 100,000 K^+ pairs with the spectrometer at 34°. Also shown is the two-particle density as a function of q and q_0. Typically a few days of running would be required to obtain 100,000 K^+ pairs. Naturally, the modest aperture of our experiment does not enable the type of systematic measurements that a large solid angle detector can perform, but it should provide complementary results. We are presently investigating the systematics involved in this type of analysis.

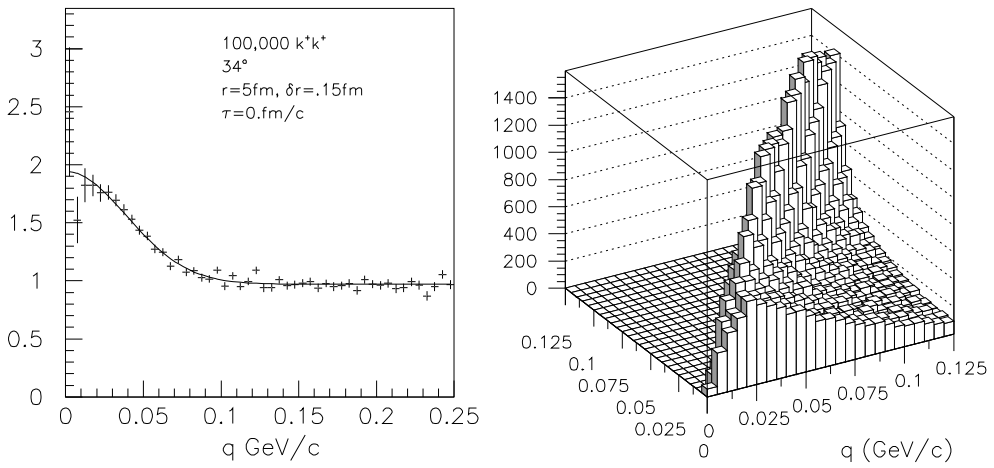

Figure 2.5: The K^+K^+ correlation function obtained with the midrapidity spectrometer at 34°. The pair density as a function of q and q_0 is also shown.

2.4 $\phi(1020)$ Measurement

One of the potential signatures of QGP involves the measurements of ϕ production in ultra-relativistic heavy-ion collisions[8,9,10]. Modifications to the width and mass of the ϕ, e.g. caused by a chiral symmetry restoration, and in particular a study of the p_t dependence of such effects, might constitute a signature of QGP formation, since the low p_t ϕ's will decay inside the hadronic fireball.

The BRAHMS midrapidity spectrometer (see Section 3.2), with its reasonable solid angle and good hadron identification, can be utilized to study ϕ meson production dynamics from Au+Au collisions at RHIC energy via its decay to K^+K^-.

Figure 2.6 shows the distributions of the accepted ϕ mesons in p_t and y (rapidity) space. The calculation is for ϕ detection via the K^+K^- decay mode with the midrapidity spectrometer at 34° and 90° and $\int B \cdot d\ell$ = 0.28 T-m. A momentum resolution, $\delta p/p$ = 1.0%, for each component of the momentum is assumed in the calculation, and the

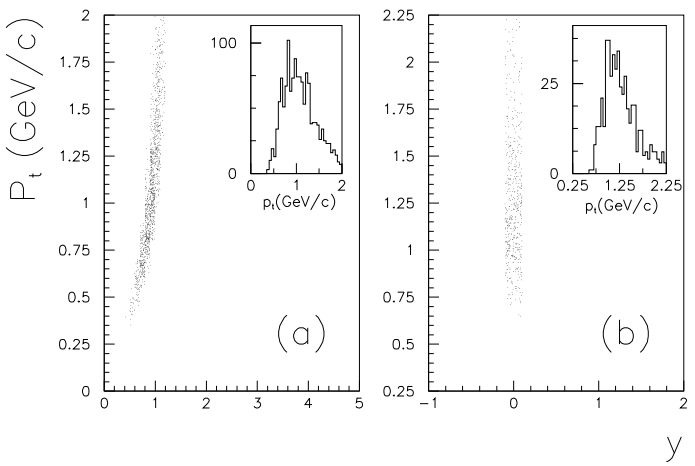

Figure 2.6: Distributions in (y,p_t) space of the accepted ϕ mesons detected through the K^+K^- decay mode, with the midrapidity spectrometer at (a) 34° and (b) 90°. Insets show the accepted p_t distributions.

ϕ mass is distributed according to a Breit-Wigner function with a known width[11]. The expected invariant mass distributions of K^+K^- pairs are shown in Fig. 2.7 for 10 million central Au+Au events with the midrapidity spectrometer at 34° (40 million at 90°) using the prediction of VENUS. 20% of the $K^\pm$'s are assumed to come from ϕ's. The solid curve shows the combination of all K^+K^- pairs, and the dashed line in the figure corresponds to the background distribution from the combinations of all the single K^+'s and K^-'s. The insert shows the difference of the solid and dashed curves. This shows that the ϕ can be well reconstructed with $\Gamma \sim 5.7$ MeV from high multiplicity events.

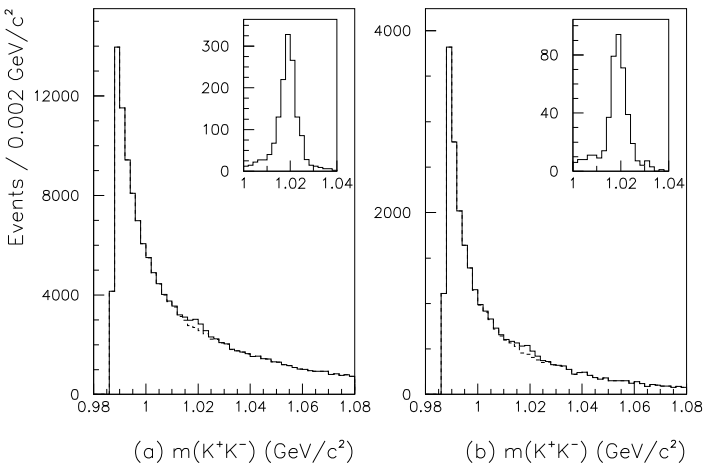

Figure 2.7: The expected invariant mass distributions of K^+K^- pairs with the midrapidity spectrometer at (a) 34° and (b) 90°. The solid curve shows the combination of all K^+K^- pairs, whereas the dashed curve shows the combinatoric background distribution. The inset shows the difference of the solid and dashed curves.

2.5 References

1. B. Andersson, G. Gustafson and B. Nielsson-Almqvist, Nucl. Phys. **B281**, 289 (1987).
2. K. Werner, Z. Physics **C42**, 85 (1989).
3. H. Sorge, H. Stöcker and W. Greiner, Ann. Phys. (N.Y.) **192**, 266 (1989).
4. Th. Schönfeld, *et al.*, Nucl. Phys. **A544**, 439c (1992).
5. D. Beavis, *et al.*, RHIC Letter of Intent #8, Brookhaven National Laboratory, 1990; Addendum, 1991; Revised, 1992.
6. L.Van Hove, Physics Lett **B118**, 138 (1982).
7. C. Albajar *et al.*, Nucl. Phys. **B335**, 261 (1990).
8. A. Shor, Phys. Rev. Lett. **18**, 1122 (1985).
9. P. Koch, U. Heinz and J. Pisút, Phys. Lett. **B243**, 149 (1990).
10. D. Lissauer and E. Shuryak, Phys. Lett. **B253**, 15 (1991).
11. Particle Data Group, Phys. Rev. **D50**, 1173 (1994).

Chapter 3

Detector Overview

In this chapter we present the design of the BRAHMS experimental setup which will measure inclusive and semi–inclusive $p^{\pm}$, $\pi^{\pm}$, and $K^{\pm}$ spectra in the pseudorapidity interval $0 \leq \eta \leq 4$ ($2^{\circ} \leq \theta_{lab} \leq 90^{\circ}$). The quite different experimental conditions at midrapidity and at forward rapidity lead to a natural division into two regions. The region 30°-90° (or 20°-90° for lighter ions) will be measured with a simple, rather short spectrometer covering the momentum region up to 5 GeV/c, while the region from 2° to 30° will be measured with a small solid angle device which can measure momenta and identify particles up to ≈25 GeV/c.

The same technology will be used for detector components in the two spectrometers wherever possible.

Figure 3.1 shows the floor plan of the spectrometers, which are both freely rotating, with the forward arm placed at the 2° angle setting and the mid-rapidity arm placed at 75°. The labeled detector components are described in the following paragraphs. Considerations of rates for inclusive measurements are given in Appendix C.

3.1 Forward Spectrometer

The forward spectrometer arm will contain four magnets, D1–D4, for sweeping and analyzing primary particles emerging from the reaction. In order to fit in the space by the beampipe at the most forward setting of 2°, D1 is of a septum design; in order to bend 25 GeV/c particles, it will have a field of up to 1.2 T. The other magnets, D2–D4, as well as D5 on the midrapidity arm, are of conventional design. All the movements of the magnet platforms will be remotely controlled, and absolutely positioned to better

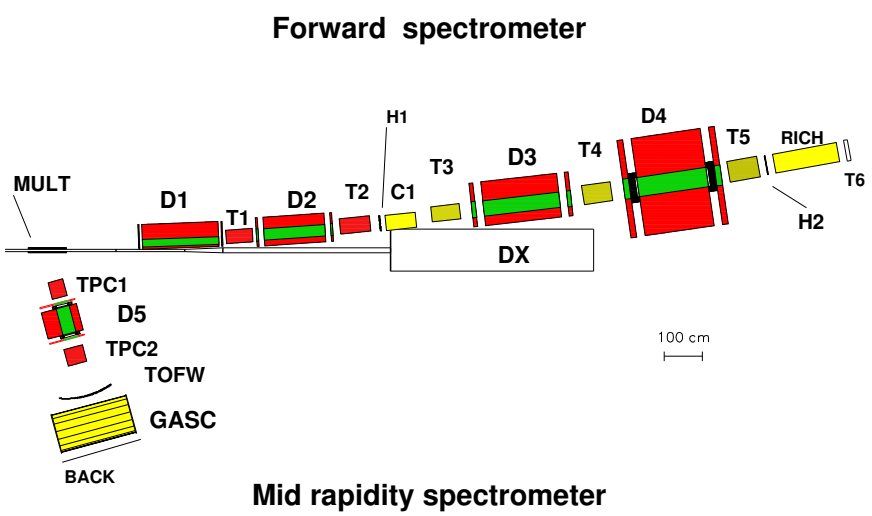

Figure 3.1: Layout of the BRAHMS spectrometers. Both spectrometers are freely rotating: the forward arm is shown at $\theta = 2°$ and the midrapidity arm at 75°. Further details concerning the individual components labeled here are given in the text.

than 1 mm.

The forward arm tracking detectors T1 and T2 are small time projection chambers (TPC's) which provides good three-dimensional track recognition and rejection of background. The TPC's operate outside the magnetic field and have quite small drift distances (≈20 cm) . The requirements for T1 are the most stringent since it has to deal with estimated particle densities up to the order of order 0.2 particles/cm^2. For T2 the estimated number can be up to 0.05 particles/cm^2. The tracking detectors T3–T5 will be conventional drift chambers with $\approx 16 - 22$ planes per detector. The results from recent tracking simulations indicates that T3 might also be a TPC. The positions of tracks are determined locally to better than 0.3 mm and their direction to better than 0.5 mrad.

The lower momentum part of the particle identification for the forward arm is based on two time-of-flight hodoscopes, H1 and H2. Each of the 60 staves (40 for H1 and 20 for H2) will be instrumented with a fast photomultiplier at both ends, with a time resolution of $\sigma \leq 75$ ps. The H1 array at 9 m from the vertex will provide 4σ separation of π and K to 3.3 GeV/c and K/p to 5.7 GeV/c. The H2 array at 20 m, after D4 will have 4σ separation of π/K to 5.0 GeV/c and K/p to 8.5 GeV/c.

High momentum particles will be identified at two places in the forward spectrometer: namely after D2, covering the range of 2.5–6 GeV/c, and behind D4 with coverage from 4 to 25 GeV/c. The first region, behind D2, will be instrumented with a conventional segmented Čerenkov tank, C1. A ring-imaging Čerenkov detector (RICH) with C_4F_{10} as the radiator gas will sit behind H2 to perform K/π separation up to $\approx$ 25 GeV/c

and K/p separation to much higher momentum. This is accomplished by determining the ring radius with an accuracy of $\Delta r/r \approx 2\%$. A readout scheme using four large (10×10 cm^2), highly segmented photomultiplier tubes will be used for this detector. T6 is a back counter to confirm hits behind the RICH counter.

3.2 Midrapidity Spectrometer

The midrapidity arm is a single-dipole magnetic spectrometer of 8 msr solid angle designed to cover the angular region from $\theta = 30^\circ$ up to 90° and to measure and identify particles with momenta in the range of $p \sim 0.2$ GeV/c to 5 GeV/c. The limitation of 30° is set by the maximum allowable particle density in the front TPC for central Au-Au events; for lighter beams the spectrometer can cover down to 20°. The magnet D5 will have a gap of $\sim 10 \times 35$ cm^2 (h$\times$w) at a distance of 190 cm from the nominal interaction point, with the width of the opening chosen so as to accept particles from a significant part of the interaction "diamond".

Since many particles detected behind the magnet arise from decays and secondary interactions, it is necessary to have tracking in front of the magnet. This purpose will be served by a time-projection chamber, TPC1, read out by approximately 1200 pad channels. A second time-projection chamber behind the magnet, TPC2, will have to deal with fewer particles than TPC1, but will be physically larger, resulting in 1000 channels. The front TPC will also provide a vertex determination to approximately 1 mm.

The time-of-flight detection will be done with TOFW, an array of 225 plastic scintillators placed at 4 m. Each element will be 22 cm high with a cross section of 0.6×0.6 cm^2 and will be instrumented with two fast tubes with a time resolution of $\sigma \leq 75$ ps. This will give π/K separation up to 2 GeV/c, and K/p to about 3.5 GeV/c. A pressurized gas Čerenkov threshold detector with segmentation ≈ 15 will give π/K separation up to ≈ 6 GeV/c. This will be augmented with a suitable back counter (BACK) to measure K conversions in the Čerenkov tank.

3.3 Rapidity Coverage

The overall coverage in y-p_t of the spectrometers is shown in Fig. 3.2 for π, K, and p. Such coverage will fully enable the experiment to follow the baryon and meson distributions from the midrapidity region to the onset of the fragmentation region and thus establish strong constraints on the physics at RHIC. The specific acceptance with all the various cuts imposed by the particle identification in y-p_t for pions and kaons using all the PID detectors is described in more detail in the chapter on particle identification. Note that

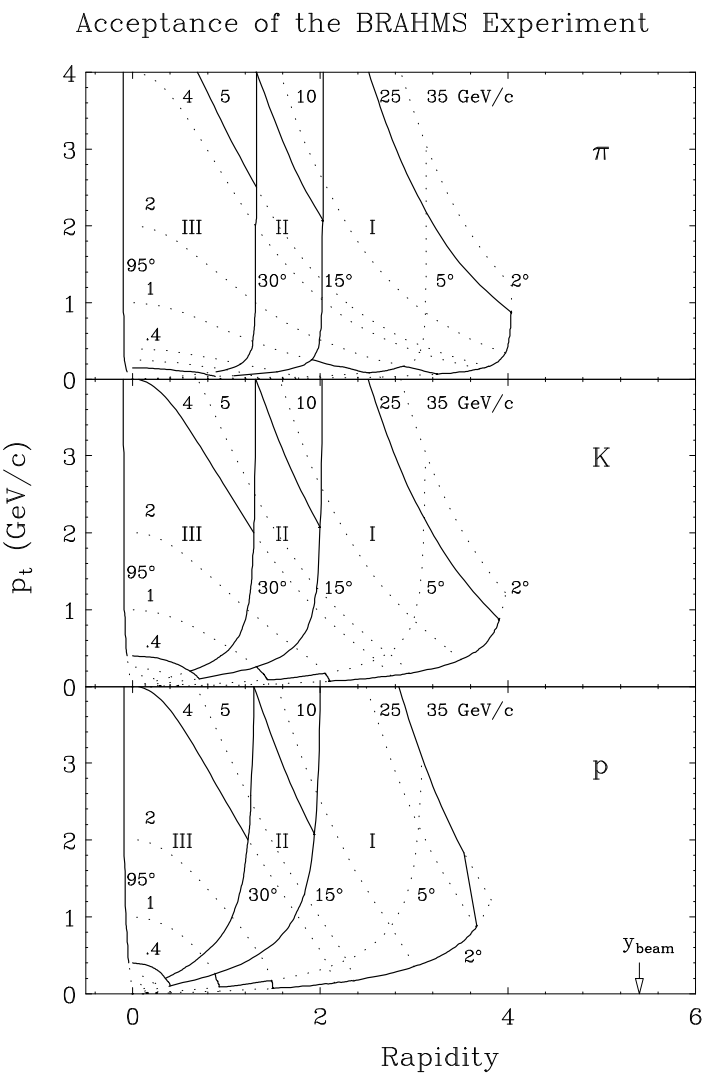

Figure 3.2: Acceptance of BRAHMS experiment for pion, kaon and protons. Region I is measured with the full forward arm, Region II with the D1-D2 complex alone, and Region III with the mid-rapidity arm.

the proton identification does not extend from p=25 GeV/c to 35 GeV/c at the 2° due to a limitation on the bending power of the magnets at that setting.

3.4 Global detectors

A charged-particle multiplicity counter (MULT) with nominal pseudorapidity coverage $|\eta| \leq 2.5$ will provide a global trigger, determining the degree of centrality of the event. The detector will also provide a measure of the $dN/d\eta$ for charged particles. An array of beam-beam counters at 2.25 m backwards and forwards of the beam vertex will provide a start-time for the time-of-flight counters, and will determine the vertex position to roughly 1 cm. The beam-beam counters will provide additional coverage in pseudo-rapidity for the charged particle multiplicity. The beam-beam counters will be phototubes with Čerenkov radiators in front.

Chapter 4

Magnets

The two spectrometer arms of the BRAHMS Experiment have a total of five dipole magnets. The magnets are conventional iron-dominated magnets with coils constructed of copper conductor and epoxy/glass insulation. The design considerations, preliminary cost estimates, and the support utilities for the magnets will be presented below.

Several parameters control the overall design of the magnets. The desired angular acceptance is the main determining factor in the horizontal and vertical gaps of the magnets and the momentum resolution determines the necessary integrated Bdl of the dipoles. The magnets are of window frame design with return yoke on one side, with the exception of D4, to accommodate the forward operating angles of the spectrometers. The window frame design provides good field quality in the magnet aperture and reduces the fringe field on the collider beam. The maximum operating field has been chosen to minimize the effects of the stray field but be high enough to achieve the needed integrated Bdl in the allotted space. Typically, the magnets have a maximum operating field of 12 kG. A summary of magnet parameters is given in Table 4.1.

The final physical parameters of the magnets are controlled by the design of the return steel and the coil. The return steel dimensions have been established by requiring that the iron thickness be one half of the horizontal gap and coil width multiplied by the ratio of the maximum operating field to 12 kG. Thus, at the maximum field the return iron is starting to saturate. The coil dimensions and conductor size are established by the available space, required Ampere-turns, and cooling requirements. The top and bottom saddle coils are run in series. The cooling paths in the conductors have been sized to provide sufficient cooling and have pressure drops and temperature rises consistent with similar systems at the AGS. The parameters of the steel and the coils are presented in Table 4.1.

4.1 Design Features

The physical layout of the magnets in the experimental area of the 4 O'clock hall is shown in Figure 4.1. The plan view of the magnets depicts their present conceptual design with the criteria summarized in Table 4.1. Detailed designs of several of the magnets have begun. Figure 4.2 shows the preliminary details of steel for D5 and Fig 4.3 details of the D5 coils.

Magnetic modeling of each of the conceptual designs will be done in both two and three dimensions to quantify the magnetic properties of the design and to aid in considering design alternatives. 2-D modeling has been completed on the five magnets using the program POISSON. Since the magnets are long relative to the gap, the two dimensional modeling will provide a good characterization of the gap field and also the fringe field on the beam side of the magnet. We present a few results for magnet D1 to demonstrate the magnet modeling. The permeability table for Inland steel 1001 has been used to reduce the fringe field. The vertical field component across the gap is shown in Figure 4.4. The good field quality across the gap is evident. The vertical component of the fringe field on the collider side of the magnet as a function of distance is shown in Figure 4.5. It is seen that the field on the collider beam is about 7 Gauss (near the front of the magnet), while the central field in the gap exceeds 12 kG. 3-D modeling has started with the program TOSCA. The three dimensional modeling will provide for estimates of the field clamp thickness, end fields into detector volumes and fringe fields which may affect the collider beam. A preliminary TOSCA result for the vertical field along the center of the D1 magnet gap is shown in Figure 4.6. The magnetic modeling will continue in conjunction with the magnet design effort.

4.2 Estimated Costs

A preliminary cost estimate has been done for the magnets. A price of $2 per pound for the machined magnet steel has been assumed. This should be a conservative estimate, but will vary based on the size of the magnet, the amount of machining and the quality of steel specified. It is expected that most of the magnet iron will be a low carbon steel such as 1006 but several magnets may be constructed of higher quality magnet steel such as 1001. Preliminary designs of the magnet coils were submitted to a vendor for estimation. The cost for assembly, testing, and cabling of the magnets is contained in the estimates for the experiment installation. It is anticipated that possible changes in the magnet designs will be well within the allowed contingency.

The present design of D4 utilizes an existing magnet. The steel will be modified to increase the vertical gap. The existing coil is sufficient for the desired 12kG field. An option to upgrade the coil package for 17kG has been considered but at present is unnecessary. The final design of the collider magnet, DX, may affect this decision. If

the close proximity of DX and D3 limits the D3 design below the designed 24kG-m, then an increase in the D4 field with an upgraded coil package could compensate for the decreased bending in D3. The present solution is the most cost effective and meets the experimental requirements.

Several alternatives were considered for magnet power supplies. We are obtaining magnet power supplies from the decommissioned LBL Bevalac Facility. These supplies will require considerable work to repackage for use in BRAHMS. However, new water cooled supplies would be considerably more expensive. Finally, the option of using existing power supplies from the AGS program has been examined, although the availability of such supplies will probably not be known for several years. This option is the most cost effective but the least certain. Therefore, we have chosen the option of repackaging LBL supplies but will continue to examine future options to minimize costs.

4.3 Magnet Support Carriages

The intended ranges of angular motion are shown in Fig. 4.1 for both the Forward and Mid-rapidity spectrometer arms. For the Forward arm, note that the symmetry axes defined by the magnet opening gaps (D1 through D4) do not lie on a straight line, but are necessarily articulated in angle. The separate carriages required to support these elements (3 in number) are outlined briefly below.

(1) MID-RAPIDITY ARM

Elements of the Mid-rapidity arm will be mounted on a carriage platform positioned to rotate (on wheels) about a vertical axis through the nominal vertex position. The platform is extended on its outboard side in order to support three equipment racks containing the power supplies and electronics needed for the detector elements as indicated: TPC1, TPC2, TOFW, GASC and BACK.

(2) FORWARD ARM - Front Section

Dipole magnets D1 and D2 are mounted on a platform pivoted at the vertex, but with a provision which allows D2 to be offset relative to the axis of D1. This can be accomplished using a single support carriage, but using a remotely controlled motor-driven adjustment which slips D2 between two previously defined positions. This front carriage element of the Forward arm will also support detector elements T1, T2, H1, and C1, so that this section can be de-coupled from the trailing part of the spectrometer in order to extend measurements to larger angles.

(3) FORWARD ARM - Rear Section

Elements D3 and D4 will be mounted on a separate carriage, which also supports the detector elements T3, T4, T5, H2, RICH and T6. The most plausible scheme assumes the carriage will be tracked on rails (independent of the front section) to predetermined stops, or remotely measured positions, to obtain the desired configurations over the limited angular range selected for this rear section.

DESIGN EFFORTS

Preliminary discussions with design engineers indicate the desired movements can be accomplished within the accuracy specified for the momentum measurements. Note that for the Midrapidity and the Front Section of the Forward Arm, the carried loads are dominated by the magnets supported, namely 8 tons and 20 tons, respectively. Since the vertex pivot point is well-defined, the above scheme resembles closely the mechanical arrangement utilized previously in AGS Experiment-802 which entailed similar rotations and loads, and was found to work quite well. The supported load for the Rear Section of the Forward Arm is substantially heavier than for the 60-ton Henry Higgins magnet described for E-802. However, the desired simple motion over a limited range ($<20^{\circ}$) again resembles the arrangement used previously for the extended Čerenkov Complex of E-802.

Brahms Spectrometer Magnets

	D1	D2	D3	D4	D5	Totals
Gap						
height (in)	3.15	6	10	12.6	4	
width (in)	7.874	10.75	15.75	20	14	
length (in)	78.75	63	78.75	72	28	
Nominal Field (KG)	12	15	12	12	12	
current (amps)	3200	3570	2813	2400	2210	
voltage (volts)	160	101	100	113	57	
DC power (kw)	512	361	281	271	126	**1551**
Coil Parameters						
weight (lbs)	110	862	3902	7000	271	
no. turns	24	54	96	96	48	
resistance (ohms)	0.049	0.028	0.035	0.0471	0.0255	
temp rise (deg F)	60	60	60	72	60	
flow (gpm)	58	41	32	26	28.4	**185**
no. paths	24	8	6	8	8	
pressure drop (psi)	78	94	81	150	54	
Magnet Parameters						
length (in)	88.5	79	103	96	39	
width (in)	19.3	38.6	56	94	40	
height (in)	22	44	58	56.6	40	
shield thickness (in)	1	2	4	6	1	
weight (lbs)	9064	30050	65200	112515	14500	
Power Supply						
AC power (kw)	602	424	331	319	148	**1825**
AC current (amps)	1234	869	678	653	304	

Table 4.1: Magnet parameters

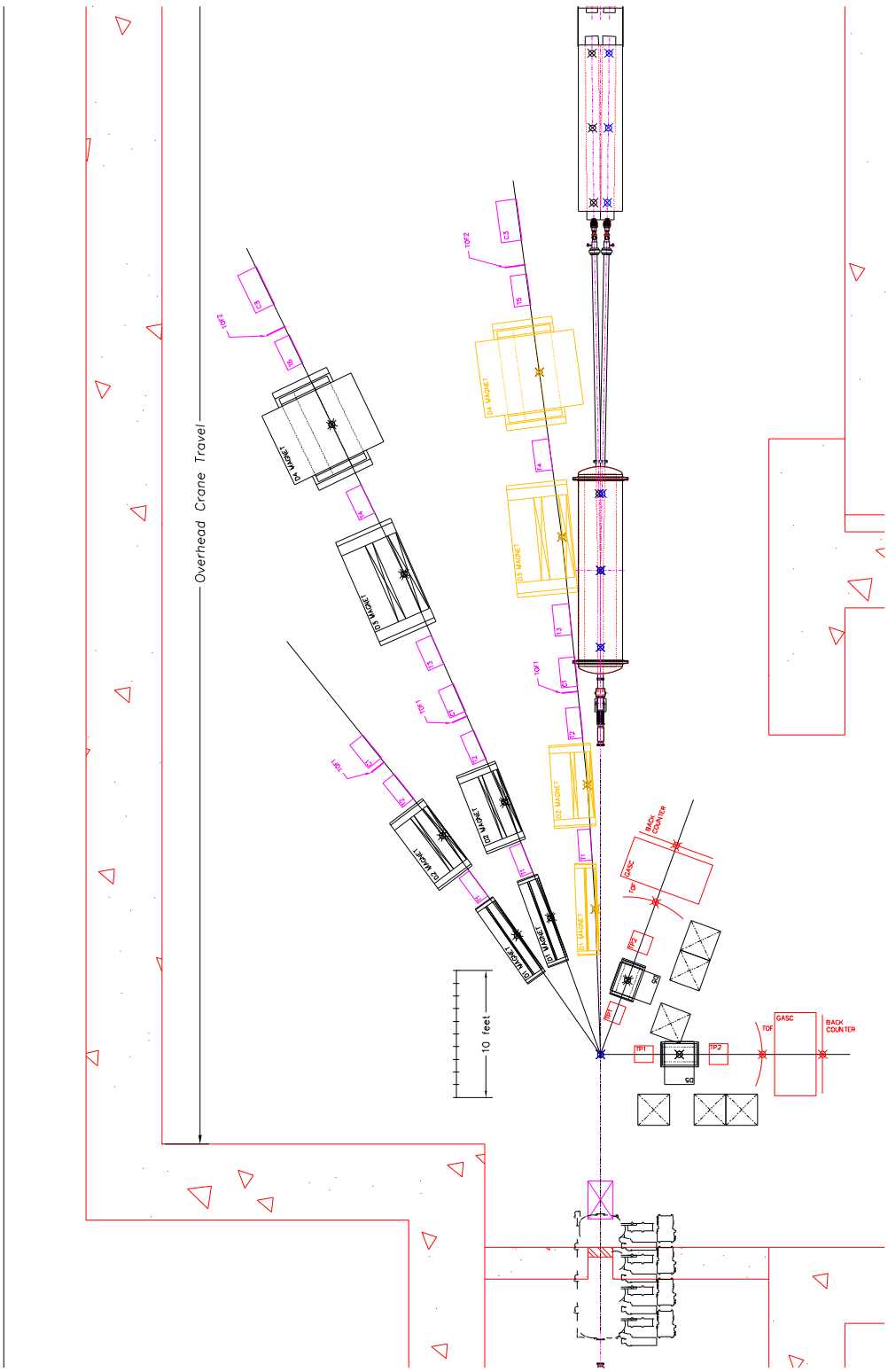

Figure 4.1: Layout of the 4 o'clock area.

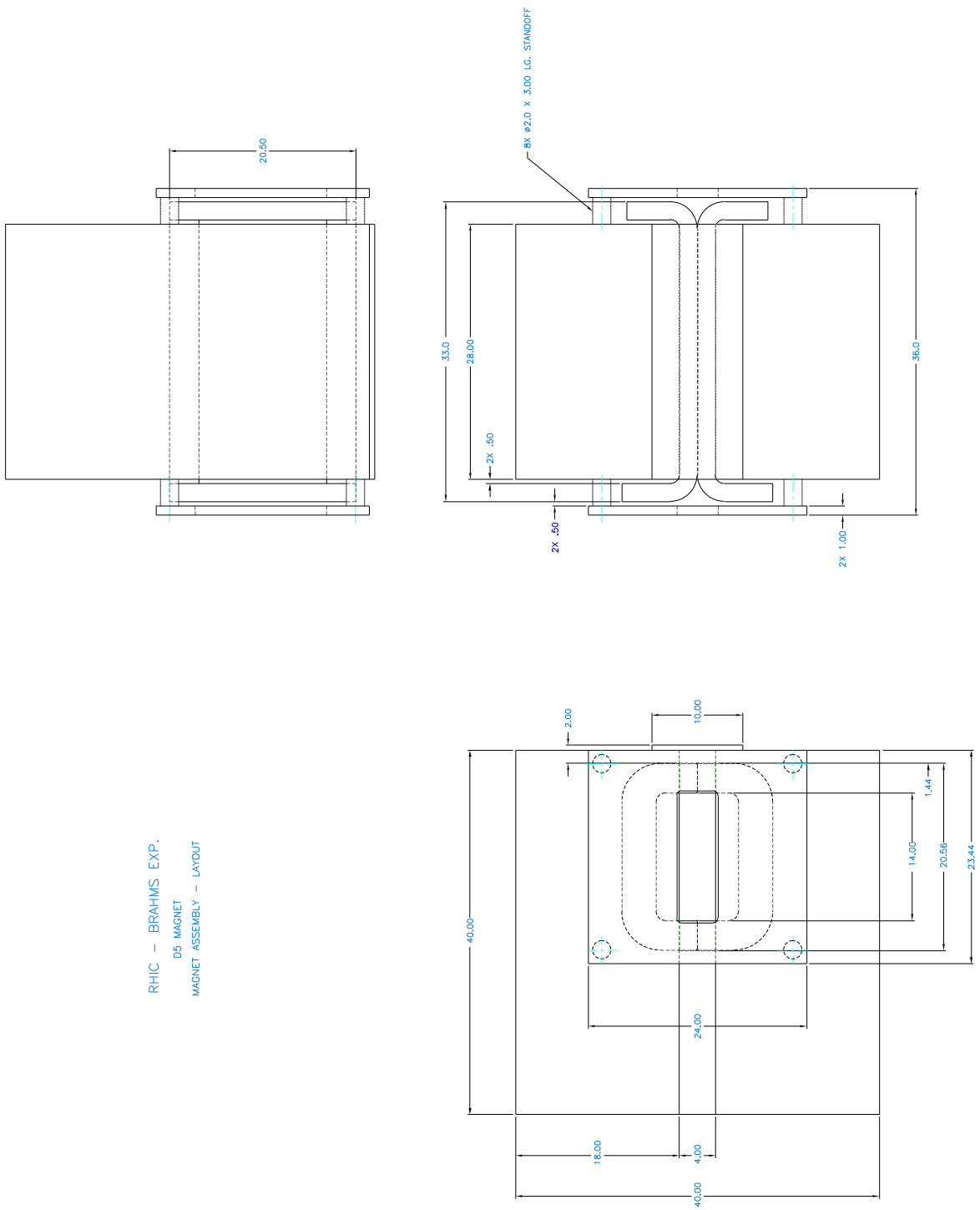

Figure 4.2: Steel design for D5.

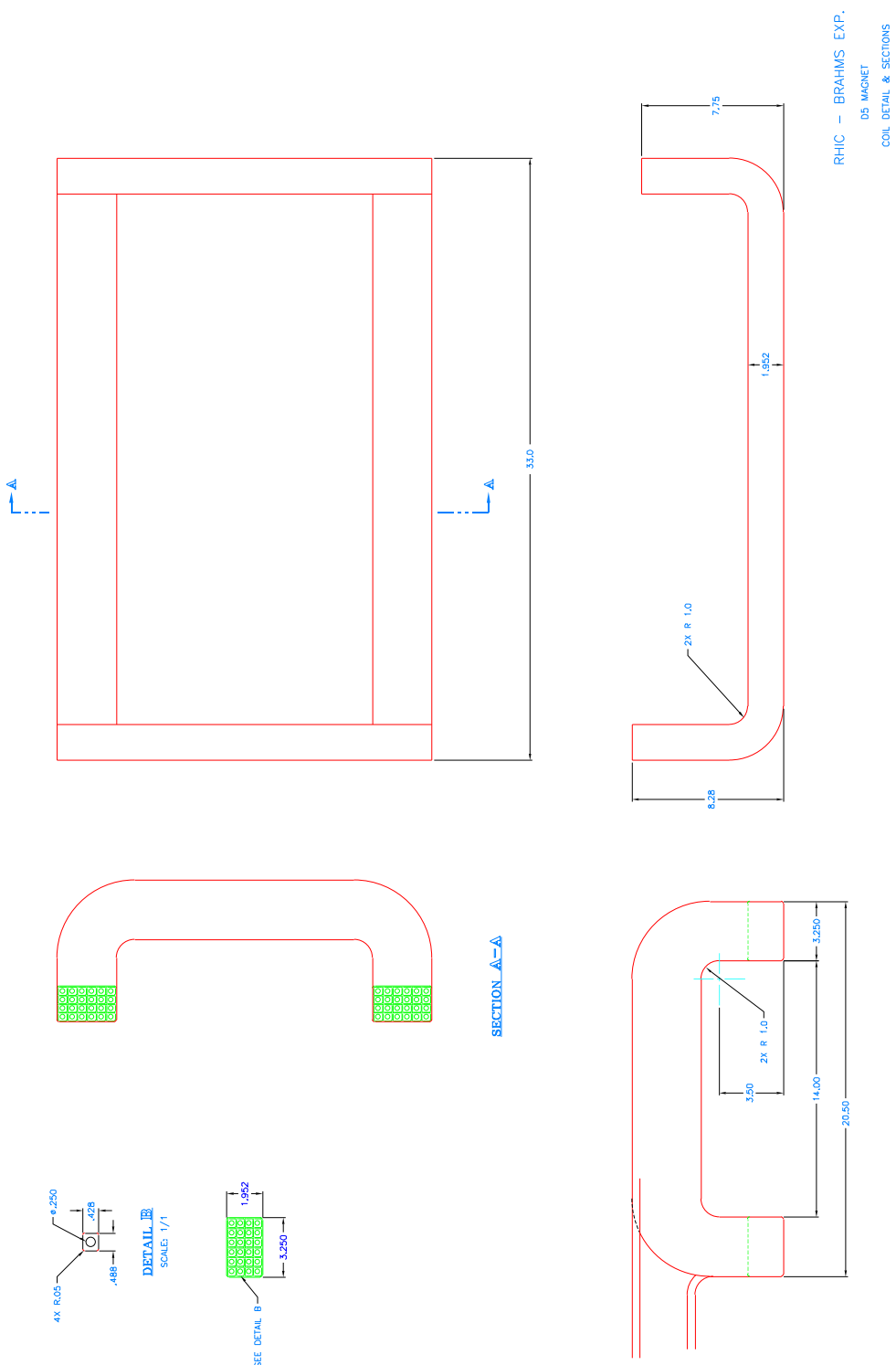

Figure 4.3: Coil design for D5.

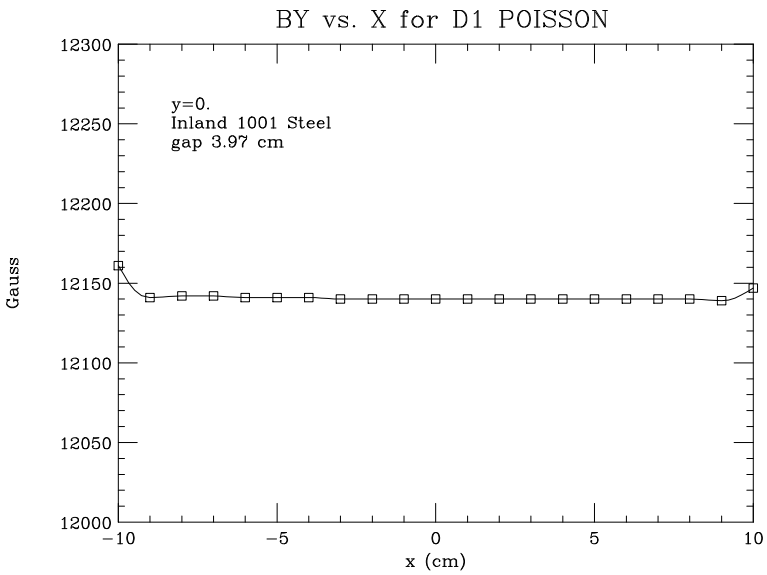

Figure 4.4: Field across the gap in D1.

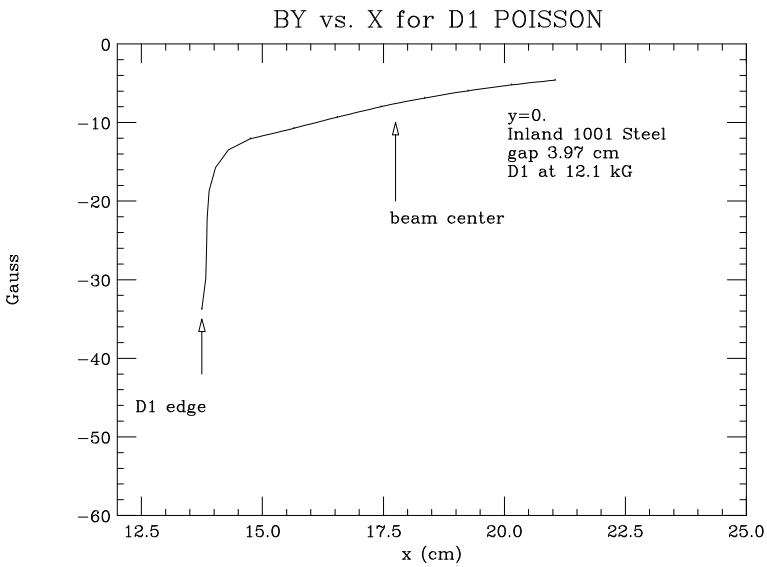

Figure 4.5: Fringe field in D1.

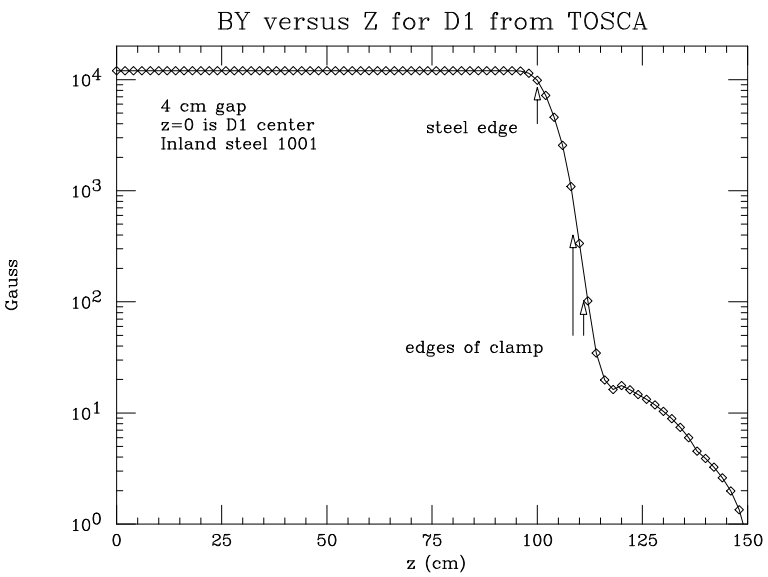

Figure 4.6: Vertical field in D1.

Chapter 5

Facilities and Experimental Layout

The BRAHMS Experiment requires a substantial area to meet the spatial requirements of its two spectrometer arms. Both the 4-O'clock and 2-O'clock intersection regions have been identified as possible experimental sites. In the following, we first consider the 4-O'clock location in some detail: historically, this was an early selection, but more importantly, it requires special considerations because of the RF cavities located at this intersection. Minor modifications necessary to locate BRAHMS at the 2-O'clock intersection, where the RF problem is absent, are given in a later subsection (5.7). In the following, we first discuss the physical layout of the experiment at the 4-O'clock area. The required resources for the experiment will be presented and interfacing issues with various collider components will be discussed. Finally, several potential upgrades to the facilities at the 4-O'clock area will be proposed.

A plan view of the experiment in the 4 O'clock hall is shown in Fig. 5.1. The mid-rapidity spectrometer is shown both at 90° and at its most forward angle of 20°. The complete forward angle spectrometer is shown at its most forward angle of 2° and largest angle of 20°. The back section is not needed for larger angles, but the forward section will operate to angles of 35° and is also shown in this setting. The shield walls have been sited to allow for the movement of the spectrometers, personnel access, and the addition of support electronics. The close proximity of the forward spectrometer to the beam pipe and DX is obvious. Issues of possible conflict will be discussed later. The required movement of the spectrometers to cover the desired p_t and rapidity ranges, coupled with the magnet and detector design, establishes the size of the experimental area.

There are several considerations which lead to the spectrometer layout as shown in Fig. 5.1. Many of the projectile fragmentation products will interact with the beam pipe between DX and D0. The forward spectrometer has been sited on the side of the accelerator opposite from where the fragmentation products will be bent by DX. This provides

additional distance and angle to shield the detectors from the interactions in the beam pipe. The experiment intends to occasionally operate both spectrometers with simultaneous coverage of the same region of phase space in order to study potential systematic effects. The experiment expects that it will be necessary to maintain the largest distance possible between the spectrometers and the RF cavities which also limits the spectrometers to that side of the IR opposite to the RF cavities. The above considerations lead to the layout shown. This arrangement also satisfies criteria established for unequal mass beams, in that both spectrometer arms operate in the region of positive rapidities for the light projectile. The proposed layout is compatible with this requirement and the orientation of PHENIX.

5.1 Shielding layout

The shielding for the experimental area has been shown in Fig. 5.1. Six-foot thick light-concrete walls have been used to reduce the dose from a full beam fault (at four times day one intensity) to less than 500 mrem for personnel outside the side wall. This is based on calculations (RHIC Note 5) which do not include massive objects located near the beam line. The close proximity of magnets when operating at forward angles may require a more careful calculation of the side wall shielding. The roof span over the experiment has been chosen to meet the requirements of the experiment and also to take advantage of available roof beams at the AGS. Fault levels through the roof will be approximately 10 times higher than the side wall, dictating that personnel should be excluded from this area. The higher radiation levels are a result of the thinner roof (four feet thick) and the smaller distances. Two access ports on each side of the area to accommodate the magnet transporter are shown. In addition, a labyrinth to allow for easy access of personnel and small equipment has been designed into the shield wall. The shielding height will need to be approximately 20 ft. to accommodate a gantry crane which would operate over the experiment but underneath the shielding roof. The shielding arrangement will continue to evolve to accommodate both the experimental and accelerator requirements.

5.2 Support Buildings

The BRAHMS Experiment will require two support buildings. The first is a counting house of approximately 1200 square feet. This area is expected to be sufficient if the electronics are distributed on the platforms with the detectors. The second is a building for the magnet power supplies and gas handling controls. These buildings are shown in Fig. 5.2. Consideration of safety, audible noise, and electrical isolation has led us to use separate structures at this stage of the design. The power supply area (900 ft^2) is large enough to accommodate air cooled power supplies on a single floor. It is intended that a small, separate section of this latter building be used to house the gas-control systems necessary for the various particle-detector elements of the spectrometers.

These two buildings have been sited on the inside of the accelerator ring near the center of the open area. This minimizes cable distances to the experiment and allows for convenient access. The outside of the experimental pad has been ruled out since there is no vehicle access, once the shielding walls are in place. Finally, it is anticipated that the utilities (power and water) will originate from inside the RHIC ring. These buildings and the two access areas for the RHIC magnet transporter use most of the available space along the 4 O'Clock area.

5.3 RF cavities and the experiment

Four storage RF cavities are planned for the four O'clock area as shown in in Fig. 5.2. There are important considerations on the compatability of the experiment and the RF cavities. A shield wall intended to protect personnel from the x-rays generated by the cavities is shown. It is anticipated that there will be occasions when it is desired to operate the RF cavities while the experiment desires access. This will be particularly true during the construction phase and during conditioning of the RF. A 30 inch concrete wall has been used to reduce the potential 100 rad/hr levels to 1 mrem/hr during conditioning of the cavities. A shield of 8 inches of iron is shown near the beam pipe. This arrangement is preliminary, representing a first-order attempt to address this problem.

The operations of the RF cavities may also create an undesirable environment for the experiment. The RF broadcast noise may induce undesired signals in the detectors and responses in the electronics. The generated x-rays may cause induced signals in the beam counters at unacceptable levels. Finally, the increased pressure bump in the cavities may increase beam-gas interactions to an intolerable level. The experiment will work in conjunction with RHIC personnel to examine these potential problems and solutions which can be implemented.

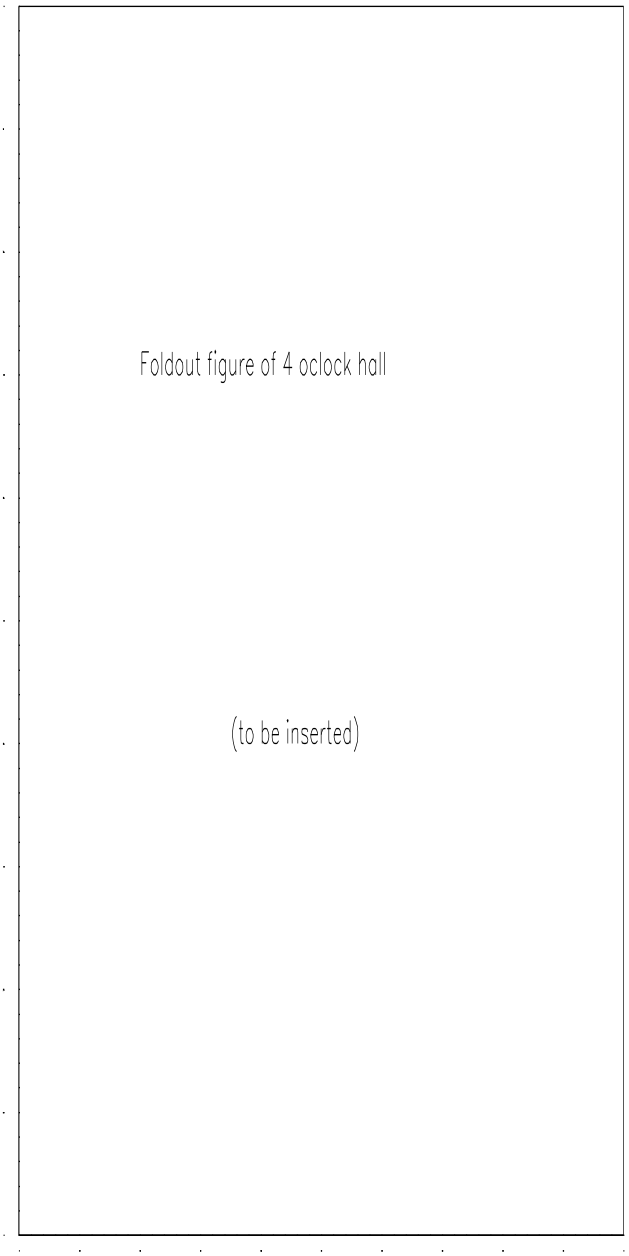

Figure 5.1: Detail of BRAHMS at the 4 O'clock area.

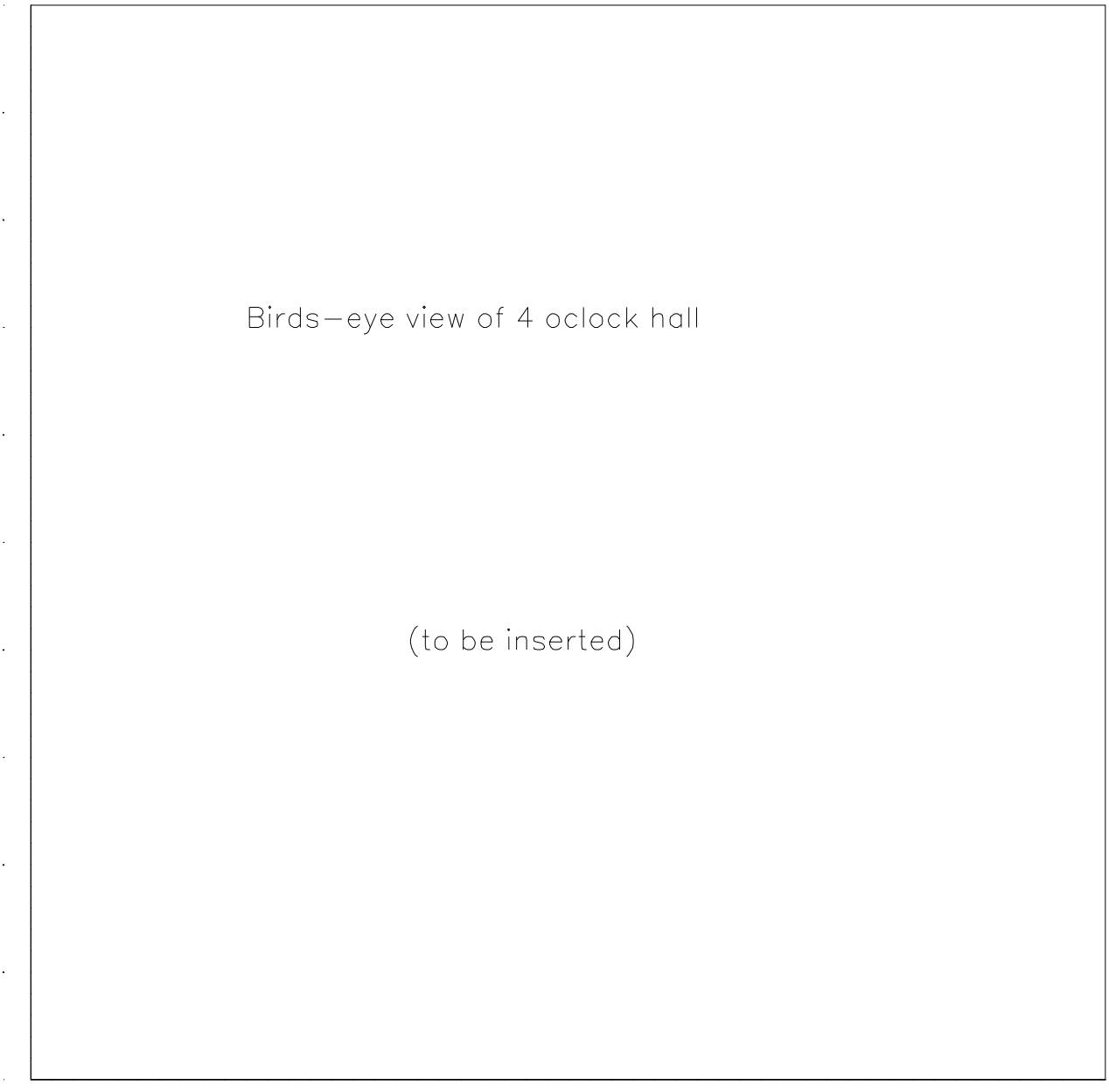

Figure 5.2: Bird's eye view of BRAHMS at the 4 O'clock area

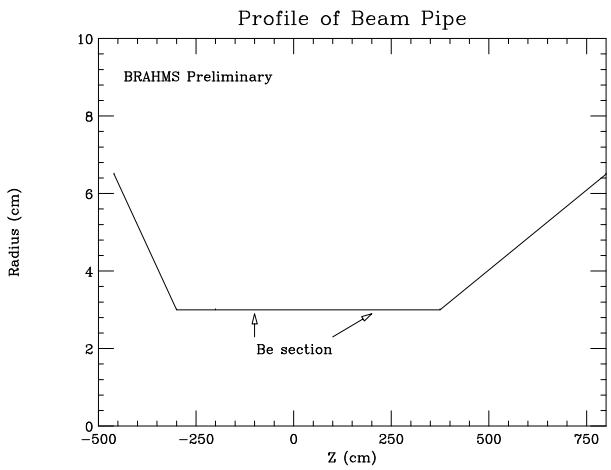

Figure 5.3: This plot illustrates the beam pipe profile for the BRAHMS intersection region. The beam pipe is stainless steel except for a 3-meter beryllium section near the beam crossing point ($z = 0$). The two conical sections expand the radius to the standard RHIC radius.

5.4 Beam Pipe

The beam pipe design in the intersection region has important consequences on the performance of the experiment. The forward spectrometer and D1 are being designed to have acceptance for particles produced at 2 degrees. A clearance of 1 cm between the coil and the 2 degree trajectories is required to eliminate the coils as a source of background trajectories due to secondary interactions. The coil and the retaining plate have a combined thickness of 3.75 cm leaving a total transverse distance of 4 cm to the center of the beam pipe. 1 cm of this space is intended for clearance, which establishes the maximum radius of 3 cm for the beam pipe. The simplest geometry for the beam pipe which would meet the need of the experiment would require the 6 cm diameter to extend from the intersection point to about the middle of D1, ie. about 3.5 meters. The diameter of the beam pipe along magnet D2 and the back portion of D1 is being examined in conjunction with the shielding design to reduce produced secondaries in the experiment's detectors. A preliminary diagram is shown in Fig. 5.3.

The diameter of the beam pipe can affect several aspects of the accelerator performance. The beta function shown in Fig. 11.6 of the RHIC Design Manual demonstrates that a 3 cm radius beam pipe near D1 is a larger aperture relative to the beam than the 5 cm radius pipe in D0. The vacuum achievable in the intersection region will be dependent on the beam pipe design. The ability of the pumping system to provide sufficient vacuum will need evaluation in conjunction with the design. We have addressed these issues with RHIC personnel and concluded that a beam pipe design which meets the machine and experimental parameters should be readily achievable.

5.5 Utilities

The experiment will require AC power and cooling water. The total AC power for the experiment is about 3MW. This is dominated by the 2 MW necessary for the DC power supplies. The experiment estimates requirements of 0.2 MW of clean power provided by an isolation transformer and 0.1 MW of power for lights, motors, fans, air conditioning, etc. Until the design is more complete we have added 30% contingency to this power request. The experiment will require 250 GPM of cooling water for the magnets and power supplies. The system should have at least 150 psi and handle a temperature rise of 75 degrees fahrenheit.

5.6 4 O'clock Facilities and Improvements

The items discussed in this chapter constitute a baseline facility for the BRAHMS Experiment. Discussions with the RHIC organization indicate that these baseline facilities are reasonable and will be provided by the RHIC organization at the IR in which the experiment is sited. We have discussed the transition of responsibilities for various systems to ensure that the appropriate costs are included in the BRAHMS budget. These considerations have been included in the budget and schedule given in Chapter 10 for BRAHMS.

We have suggested several possible improvements to the 4 O'clock area be considered which would enhance this area for BRAHMS, the accelerator systems, and other potential experiments. The experiment has discussed these options with the RHIC organization in preparing this CDR for BRAHMS. Although initial budgetary constraints may not allow these improvements to occur before initial machine operation, the option to implement these upgrades after the startup of the machine should be considered in the design and layout of the facility.

Removing the RF from this intersection region will greatly increase the versatility of this intersection region for BRAHMS and other potential experiments. It is expected that measurements in conjunction with the RF cavity test will determine whether BRAHMS and the storage RF can compatibly occupy the same intersection region. The present RF installation planned at 4 O'clock will certainly limit the upgrade options to BRAHMS and other experiments which might be able to use this area in the future.

A building and crane over the intersection region would be a valuable asset to the area. We suggest that an option to cover a portion of the IR with a building (approx. 100 ft wide) and a 40 ton crane be considered. The building and crane could be extended when future upgrade funds become available. Without this option, it will be nearly impossible to remove the roof shielding once the BRAHMS Experiment has been constructed. The decreased cost of installing shielding, weather-proofing the shielding, experimental installation, and accelerator component installation may make this an

intelligent cost effective option.

The addition of an access road to the outside of the 4 O'clock area would increase the versatility of the area. Options to site the experimental counting house and/or power supply house to the outside could then be considered to prevent congestion on the inner side. This may also aid in area construction and reduce interference during the construction phase of the machine and experimental components.

5.7 2 O'clock Facility

The 2 O'clock intersection region is a potential site for BRAHMS. A layout of BRAHMS in the 2 O'clock experimental area is shown in Fig. 5.4 for illustrative purposes. The experiment fits within the allotted space, although there are several locations where the rear of the spectrometers are in close proximity to walls. If sited at 2 O'clock, the experiment would need to carefully control the final design length of each spectrometer. A crane support and existing sheet metal wall would require modification to allow the forward spectrometer to reach 20°. We have discussed the issues of siting BRAHMS at either 2 or 4 O'clock with the RHIC organization. They are considering the benefits of either location in the context of both BRAHMS and the overall collider program.

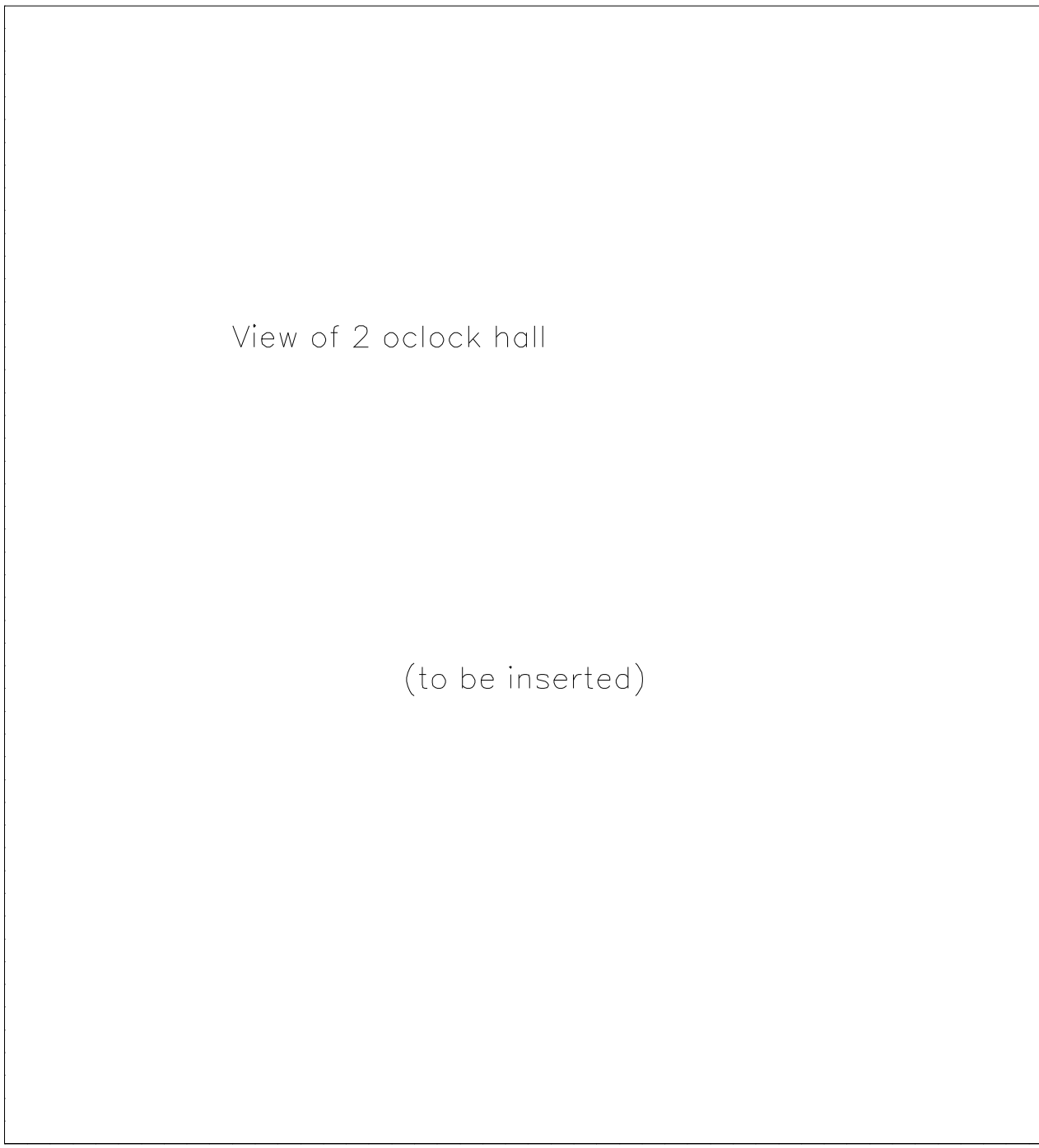

Figure 5.4: Layout of BRAHMS at the 2 O'clock area

Chapter 6

Tracking

This section describes the tracking detectors, their required performance and design. The forward spectrometer and the midrapidity spectrometer are dealt with in separate sections. The design criteria are somewhat different for the two spectrometer arms due to the different momentum ranges to be covered. Both arms will have TPC's as tracking detectors. At the present time a detailed design for the tracking detector has not been developed, but as described in Section 6.3, a prototype TPC has been built at Strasbourg and is undergoing tests. These tests as well as simulations will form the basis for a final design. The requirements in terms of size, number of pad rows for the TPC's and number of wire planes for the drift chambers in the Forward Arm are well understood.

6.1 Forward Spectrometer

The tracking of particles in the spectrometer involves several overlapping considerations. The first is the optics and layout of the spectrometers, which determines acceptance, multiplicities of particles, etc., in the different detectors. The second is how to determine the momenta of particles reconstructed through the tracking detectors, and the third the design of these detector components. This report deals mainly with the first two issues, and only discusses the conceptual design of the forward spectrometer tracking detectors.

6.1.1 General tracking considerations

The design of the spectrometer comes from some fairly simple tracking criteria. That the actual choice is workable is also confirmed through extensive simulations.

As has been described in the overview the forward spectrometer will be operating in two different modes.

- High-momentum mode. The forward-going particles are swept by the dipoles D1 and D2 towards the back end of the spectrometer where they are tracked in the chambers T2, T3, T4 and T5. Their momenta are determined by these measurements and the knowledge that they passed though the dipoles D3 and D4. The particle identification (PID) is done after D4 and T5. The particles are traced back to T2, and their trajectories projected back through D2 and D1 to confirm that they arose from the interaction point, and not from secondary scattering on polefaces, etc. The tracks must be found in T2, but not necessarily in T1.

- Low-momentum mode. The particles are tracked by T1 and T2 and their momenta determined by the dipole D2. The PID is done right after T2. The particles are projected back through D1 towards the

  interaction point to ensure their validity. This mode is used both at forward angles and at angles up to 30°.

These two modes of operation set the requirements on the tracking detectors.

Position and angular resolution

In the spectrometer system it is necessary to follow segments of a track from measurements in one tracking detector to the matching track segments in another element. This involves typical distances of 4 m. Several factors contribute to how well this can be done. First are the physical processes, such multiple scattering, which affect the tracks. For high momentum tracks this effect is usually small and can thus be dealt with. The variance due to multiple scattering for pions and protons passing through 4 meters of air has been evaluated using the following expression:

$$y_{plane}^{rms} = \frac{1}{\sqrt{3}}\,\theta_0 \ ,$$

where

$$\theta_0 = \frac{13.6}{\beta p}\sqrt{X/X_0}\ (1 + 0.038\ \ln(X/X_0)) \ ,$$

p is the momentum in GeV/c, βc is the velocity, X/X_0 is the thickness of the scattering medium in radiation lengths and y_{plane}^{rms} is the variance in a given plane at distance X. This relation is plotted in Fig. 6.1. It is observed that for particles with momenta above 2 GeV/c this contribution is less than 1 mm.

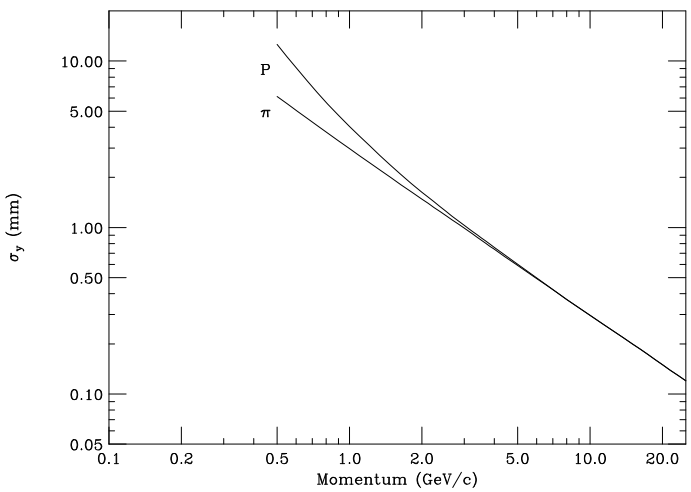

Figure 6.1: Variance due to multiple scattering over 4 meters of air.

A more important factor in the ability to project tracks is the accuracy of position measurements in the tracking detectors. Assume for simplicity that tracks are measured at the entrance and exit of each tracking detector with a resolution σ_D. Then the track can be traced back a distance X with an accuracy given by

$$\sigma_y \approx 2\sigma_D X/L_{det} \ ,$$

where L_{det} is the length of the detector volume. As an example, a detector with length $L_{det} = 80$ cm, a distance $X = 4$ m and the condition that $\sigma_y \leq 2$mm requires the resolution $\sigma_D \leq 285 \ \ \mu$m . The condition is reasonable for matching the tracks and the required position resolution is not difficult to achieve.

The momentum resolution of the spectrometer is given to first order by

$$\frac{\delta p}{p} = \frac{\delta \theta}{\theta} = \frac{2\sigma_D p}{0.30\, Bdl\, L_{det}} \ ,$$

where Bdl is in T-m integrated through D3 and D4. For the momentum setting which covers 7.5-15 GeV/c and $Bdl = 2.4$ Tm we calculate $\delta p/p = p \times 0.09\%$, where p is in GeV/c.

To confirm that the above-mentioned criteria are indeed fulfilled a GEANT simulation with tracking was performed. Specifically, 10 GeV/c pions were emitted from the interaction point, traced through the spectrometer system, and their hits recorded at the entrance and exit of all detector elements. The tracking algorithm used this information with an assumed position resolution of 200 μm to match track segments, reconstruct the momentum and follow the tracks using the procedure outlined above for the high-momentum setting. The extracted $\delta p/p$ distribution is shown in the left-most frame of Fig. 6.2.

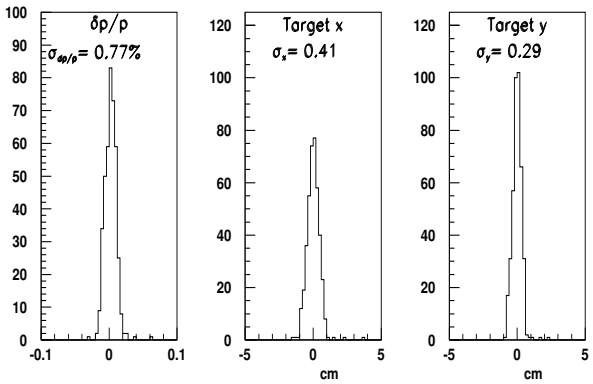

Figure 6.2: Reconstructed momentum resolution, target position distributions for 10 GeV/c pions with an assumed position resolution of 200 μm .
.

In the other two frames are shown the projected target positions. Note that even over the lever arm of 8 m from T2 to the interaction point the distribution is determined to better than 5 mm. In Table 6.1 below is shown the variance as a function of the assumed detector resolution.

σ_D μm	σ_p/p %	σ_x mm	σ_y mm
100	0.39	2.2	1.9
200	0.77	4.1	2.9
250	1.00	5.1	3.6
300	1.15	6.5	4.6

Table 6.1: Resolution of momentum and of determined target position as a function of the intrinsic detector resolution for 10 GeV/c π^-.

Particle Multiplicities

Of great importance to the detector design are the particle multiplicities and particle densities with which each detector element must contend. These quantities have been evaluated using GEANT simulations with 400 central Au+Au events from VENUS as input, and the results are summarized in Tables 6.2 , 6.3 and 6.4. The estimates do of

course depend critically on the angular and magnetic field settings. Here we consider three cases which are important and the most difficult to deal with.

- Spectrometer at 2.1° setup for intermediate momentum acceptance, i.e., $p = 7.5 - 15$ GeV/c.
- Spectrometer at 2.1° setup for high momentum acceptance, i.e., $p = 15 - 30$ GeV/c.
- Spectrometer at 2.1° for low momentum setting, i.e., $p = 2 - 5$ GeV/c. For this setting D2 is rotated 5° relative to D1 whereas in the normal mode of operation D2 is only rotated 1.8°.

Only particles which were emitted toward the first dipole D1 were tracked. A discussion of background from other sources is presented later. In addition to the primary particles

Detector	N_{prim}	N_{sec}	N_{total}	particles/cm^2
T2	4.1	3.5	7.6	0.02
T3	2.7	4.4	7.1	0.007
T4	1.5	0.8	2.4	0.002
T5	1.0	0.5	1.6	0.001

Table 6.2: Expected charged particle multiplicities for the 7.5-15 GeV/c setting at 2.1°.

emitted from the interaction, secondaries are generated primarily from the magnet yokes and field clamps, and to a lesser extent from the detectors.

Detector	N_{prim}	N_{sec}	N_{total}	particles/cm^2
T2	2.2	2.5	4.7	0.01
T3	1.2	4.6	5.9	0.006
T4	0.6	1.0	1.6	0.001
T5	0.3	0.5	0.8	0.0004

Table 6.3: Expected charged particle multiplicities for the 15-30 GeV/c setting at 2.1°.

The expected multiplicities are presented in the tables above. It can be observed that near the end of the spectrometer, i.e. in T4 and T5, the expected multiplicities are quite low, with the typical number of charged particles being 0.5–2. This sets only modest requirements for the tracking and PID detectors. On the other hand the charged particle multiplicities in T2 and T3 are higher and reach values of up to 8. The fairly high background rate in T3 is due to particles coming though the spectrometer which produce secondary emissions in the beamline magnet DX. Even for T1 the particle densities are acceptable for all settings.

Detector	N_{prim}	N_{sec}	N_{total}	particles/cm^2
T1	6.6	10.0	16.5	0.04
T2	2.4	1.4	3.8	0.01

Table 6.4: Expected charged particle multiplicities for the 2-5 GeV/c setting at 2.1°.

Detector	Primary	Background No Shield	Background With Shield
T2	4.3	11.8	5.3
H1	3.8	10.2	5.9

Table 6.5: Effect of shielding on rates per central Au+Au event in T1, T2 and H1 of the forward arm.

Shielding of Detectors

The very large expected multiplicity for central Au+Au collisions will make the background conditions difficult. For the forward angle measurements backgrounds generated from forward-going particles interacting in the magnet yoke, beam pipe, pump cluster and DX beam line magnet could contribute significantly to the observed multiplicity rates in the tracking and PID detectors. It would thus appear that some shielding of the detectors is needed. However, introduction of shielding for an experimental apparatus is often problematic, since it adds material from which additional secondary particles might be generated.

The T2 tracking detector plays an important role in the overall tracking of the forward spectrometer, and was thus taken as the focus for background considerations. The other tracking detectors (T3, T4, T5) being farther away from the interaction diamond have less background and can be more easily shielded. The proximity of T2 to the beam pipe makes it an obvious candidate for shielding. The layout of the shielding considered is depicted in Fig. 6.3. The expected background with this configuration has been estimated from several Monte Carlo runs. The shielding was envisioned to be made primarily of Pb, $\approx$ 50cm in height with a trapezoidal shape and attached to the D2 magnet and platform. (Heavymet was rejected due to cost.)

Since Monte Carlo calculations are very time consuming, the phase space considered for reaction products was confined to those emitted with polar angles less than 8°; i.e. all particles emerging towards the spectrometer and down the beamline. The results are summarized in Table 6.5 for rates of charged particles per central event.

Of the 5.3 background particles in T2, with shielding included, we know that approximately 3 come from interactions inside the magnets. Thus the increase of the charged

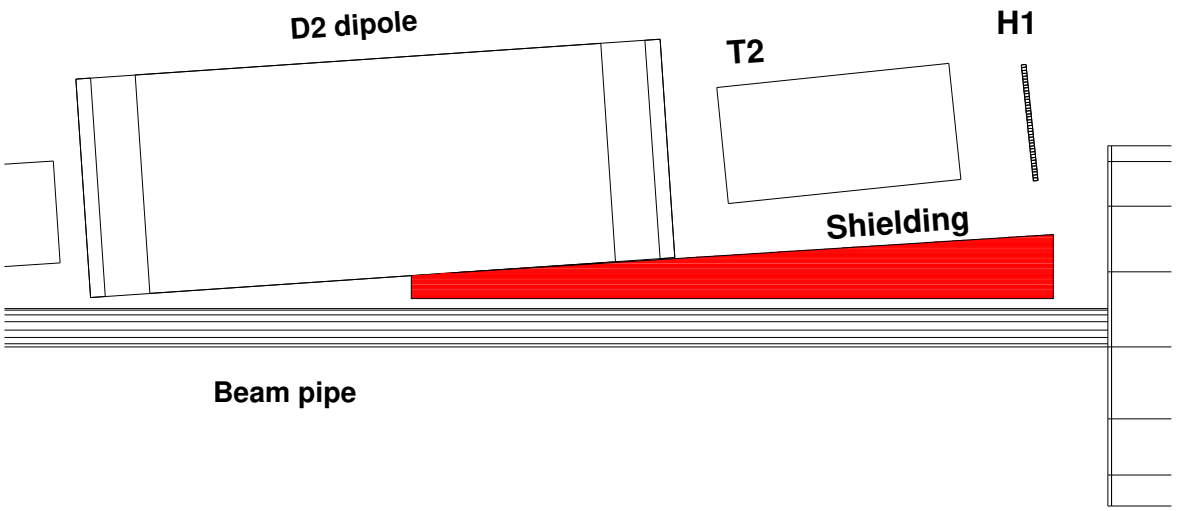

Figure 6.3: Top view of shielding for T2

particle background due to interactions in the beam pipe and shielding is approximately 2. This can easily be handled by the proposed tracking detectors. The simulations do not have a detailed description of the detector modules, and hence some additional background might be expected. However, the excellent pattern recognition capabilities of the T2 TPC will enable us to easily separate valid trucks from background tracks.

The H1 segmentation of 40 results in an average occupancy of approximately 20% for central Au+Au events at 2.1°. This can be tolerated since the measurements are inclusive. In addition it should be remembered that H1 is not the primary PID detector for the high momentum measurements but will be used to confirm the measurements in the H2 and RICH detectors.

6.1.2 Tracking Detectors

The tracking detectors T1-T5 have yet to be designed in detail, but the required capabilities are clear from the design criteria and the multiplicity considerations given above. The detectors T1, T2 and perhaps also T3 will be TPCs with good pattern recognition capabilities and intrinsic position resolution of $\approx$350 μm.

To avoid duplication of effort in detector design it was decided to use the same modular readout chambers for T1 and T2 TPC as will be used in the TPC's for the mid-rapidity spectrometer. This sets the active width for T1 and T2 to be 25 cm using a 4 mm pad spacing. The number of pad rows have been determined from simulations using the track reconstruction program SONATA (See Appendix B). The quality of local track reconstruction was judged from visual inspection of the Monte Carlo events and

Tracking Detector	width (cm)	height (cm)	length (cm)	# planes	# channels/wires	
T1	25	15	75	16	1024	chan.
T2	25	20	75	10	640	
T3	35	30	75	24	430	wires
T4	40	35	75	22	420	
T5	45	40	75	18	350	

Table 6.6: Detector characteristics for the forward arm components.

the reconstructed tracks.

The dimensions of the detectors and an approximate channel count are given in Table 6.6. The position and angular resolution resulting from sampling the track parameters on 10 rows satisfy the requirement δx <200 μm and $\delta\theta < 0.5$ mrad.

The tracking detectors T5, T4 and perhaps also T3, are envisioned to be drift chambers, each set up in 3 submodules placed at -35, 0 and +35 cm in each detector, allowing for both pattern recognition and subsequent track segment determination to a position resolution of $\approx$ 200-250 μm over the detector length of 80 cm. See Fig. 6.4 for an illustration of the layout with 3 submodules . Each submodule will consist of planes with approximately 1-cm wire spacing in a staggered geometry xx'yy'uv[xx']. (The last xx' planes may be omitted in the T5 detector.) The dimensions of the detectors and approximate channel counts are given in Table 6.6 for all five detectors T1 through T5.

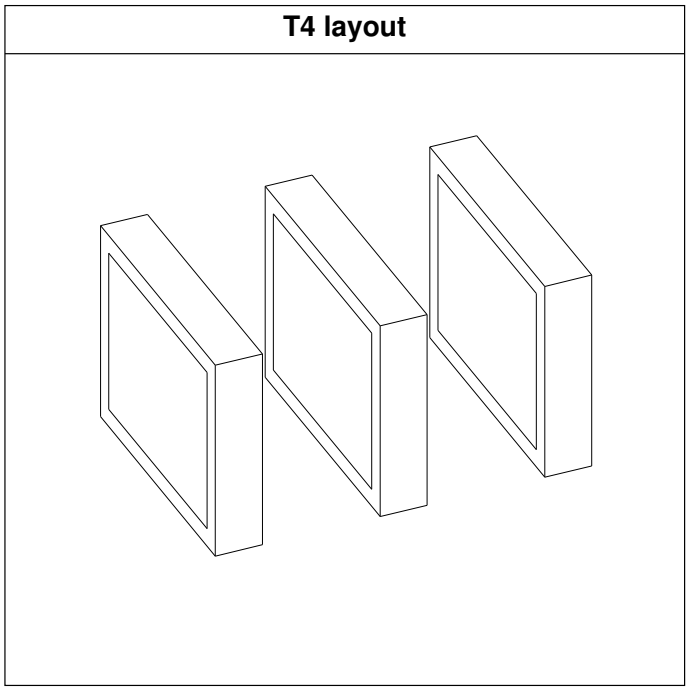

Figure 6.4: Schematic layout of T4 with 3 separate submodules of drift chambers separated by 35 cm. Each package will consist of 6 to 8 planes of drift chambers.

6.2 Midrapidity Spectrometer

The mid-rapidity spectrometer of BRAHMS (see Section 3.2) is designed to determine the momenta of individual particles by following their tracks through a magnetic field and identifying them by time-of-flight, Čerenkov and momentum measurements. The basic requirements for this spectrometer are:

- Locate all charged particle tracks (π,K,p) which originate from the interaction diamond.
- Measure momenta.
- Contribute to the particle identification (PID) completed in association with the scintillator time-of-flight wall (TOFW) and the gas Čerenkov counter (GASC).

This detector ensemble will be in an environment of high track density. The expected multiplicities and particle densities have been estimated by using the VENUS 4.02 model for central Au+Au collisions at $\sqrt{s} = 200$ GeV. The nominal setting of 34° (which in fact covers 30° to 38°) is the most difficult case to deal with, and has driven the design of the midrapidity spectrometer. Due to the low momentum of the particles, it is an advantage

to have the detectors and magnet situated as close as possible to the intersection point; on the other hand, an important design criterion is that the particle density in the front TPC be less than 0.3 particle/cm^2. To achieve this goal the midrapidity system has been placed with magnet D5 at 190 cm from the nominal intersection point and TPC1 at 90 cm. At the most forward angles the distributions are not uniform, as depicted in Figure 6.5, which shows the particle densities in the front TPC and the TOF wall at the nominal 34° setting for central Au+Au collisions. In the mid-rapidity spectrometer angular domain, the multiplicities including secondary charged particles range from 30 to 120 whereas the particle densities range from < 0.01 to 0.20 particle/cm^2 (see Table 6.7.) An overview of the particle multiplicities is given in Figure 6.6. The hit multiplicity in TPC2 is less than in TPC1 because of the smaller solid angle and because of the sweeping of particles due to the magnetic field; in Table 6.7 the field in D5 is taken as 4 kG.

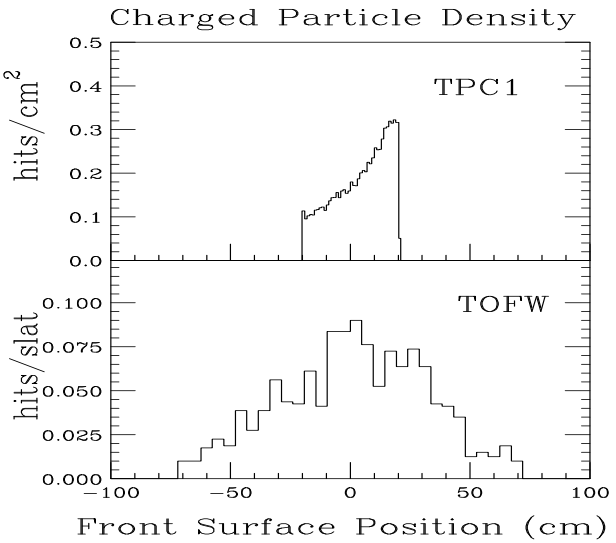

Figure 6.5: Charged particle densities in the midrapidity front TPC and TOF wall for the nominal 34° setting.

To improve the tracking capabilities by reducing both the multiple scattering and the energy loss for low momentum particles it is planned to install a helium bag inside the gap of D5.

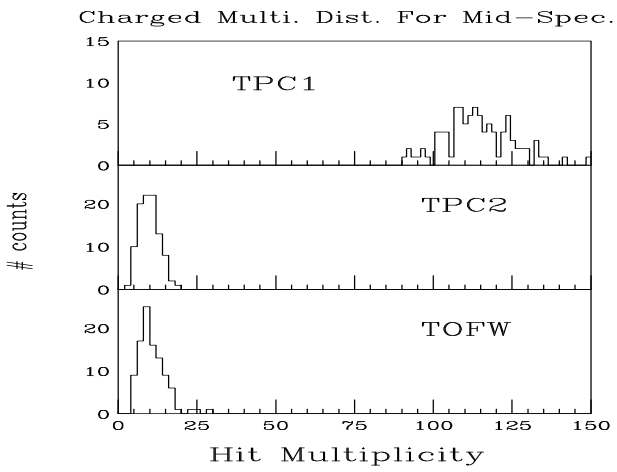

Figure 6.6: Hit multiplicities in the midrapidity TPC's and TOF wall for the nominal 34° setting.

	primary	secondary	total	particles/cm^2
34°				
TPC1	101	12	113	0.19
TPC2	7	2	9	0.01
TOFW	7	5	12	
90°				
TPC1	30	5	35	0.05
TPC2	2	1	3	0.003
TOFW	2	1.4	3.4	

Table 6.7: Average charged particle multiplicities in the midrapidity spectrometer.

6.3 Time Projection Chambers

6.3.1 Design of the Midrapidity TPC's

In order to obtain the best momentum resolution, even at low values of the momentum, one needs to minimize the amount of material in front of and in the volume of the tracking detectors. For this reason the tracking is achieved by two time projection chambers (TPC's) with the particle identification performed in separate detectors (TOFW and GASC). Precise momentum determinations are achieved by two TPC's providing three-dimensional position measurements of each particle track. These detectors, TPC1

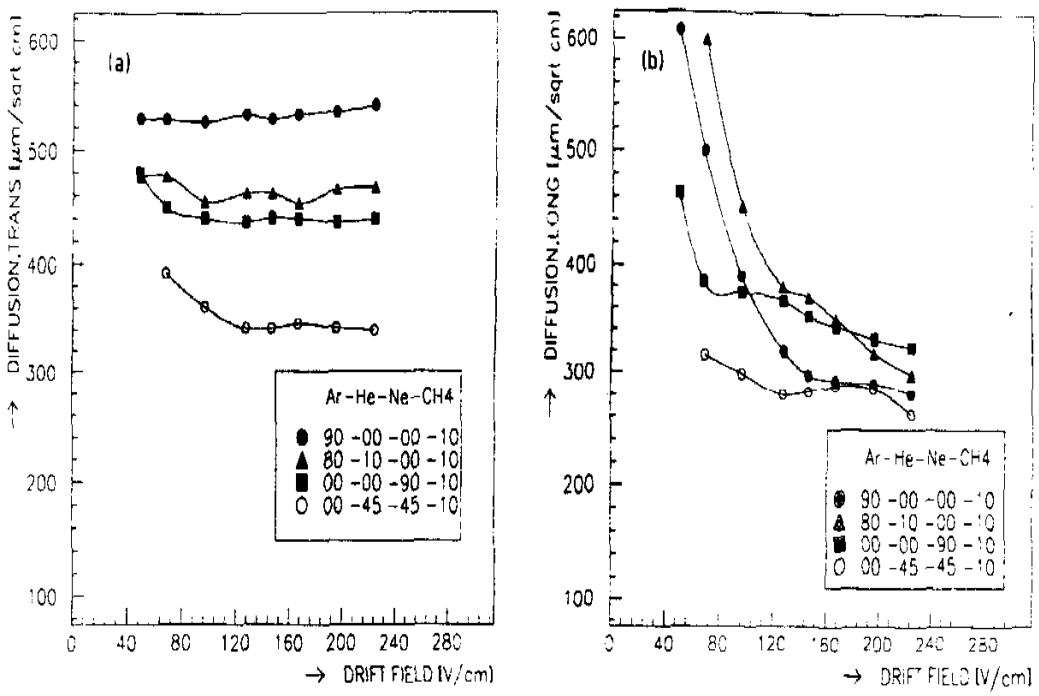

Figure 6.7: Longitudinal and transverse diffusion constants for various gas mixtures as a function of drift field.

($40\times15\times40$ cm^3) and TPC2 ($45\times20\times40$ cm^3), are located in front of and behind D5, respectively. TPC1 and TPC2, although different in size, are of the same modular design. The field cages have the shape of a rectangular box designed to operate at atmospheric pressure. Voltage grading strips are mounted on the sides in order to obtain a uniform electric drifting field. The entrance and exit windows are 25 μm mylar foils. A gating grid is opened only for selected events and avoids back diffusion of positive ions into the drift volume.

An argon-methane (88%-12%) gas mixture is used near the saturation velocity with a 130 V/cm drift field. Other gas mixtures, cool and slow gases, for example argon-isobutane (75%-25%) at 800 V/cm drift field or neon-methane (90%-10%) at 300 V/cm, will be considered also, since they would lead to a smaller electron diffusion (Figure 6.7) both in the transverse and longitudinal directions, and thus to a smaller cluster size. Since the overall drift length in our TPC's is only of the order of 15 cm and because of the timing properties of the read-out electronics, we must use gas mixtures with i) relatively low drift velocity ($\approx$2 cm/μs) and ii) small longitudinal and transverse diffusion. New low mass gas mixtures such as He-C_2H_6, Ne-C_2H_6 and Ne-CO_2 are being tested with our prototype TPC.[2]

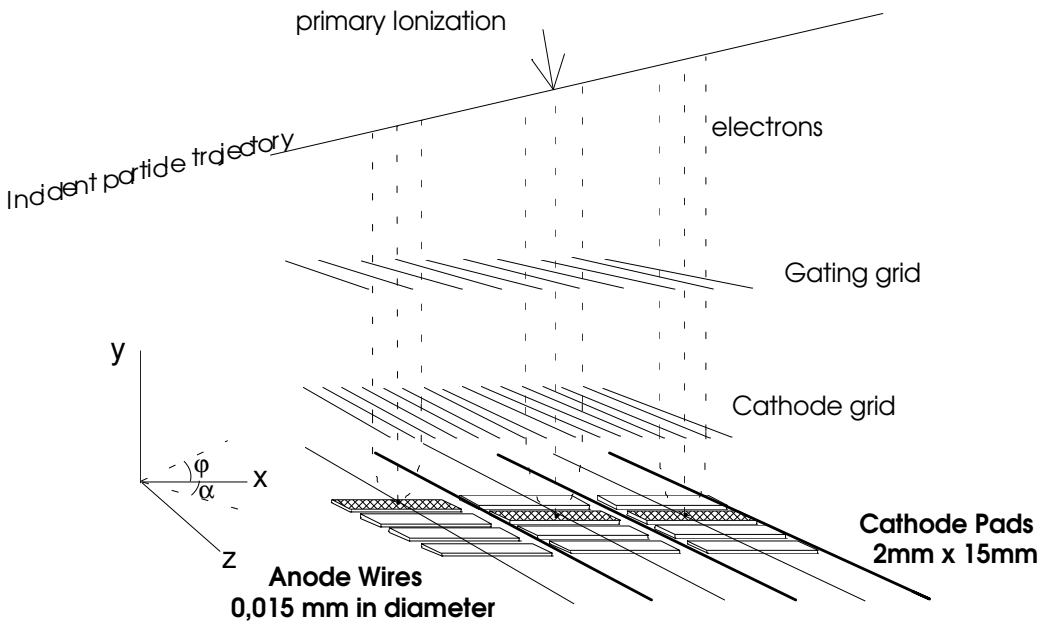

Figure 6.8: Schematic view of the pad-readout TPC.

Read out schemes

The primary ionization electrons drift toward the readout plane which contains thin gap (3 mm) proportional counters. Two usual readout schemes, either multiple anode wires or pad planes, are implemented in the prototype TPC we have built and are under test for spatial resolution capabilities. These read-out planes are of modular construction: each module consists of two read-out rows typically 38 cm long and 6 cm wide. Any number of these modules can then be assembled to build TPC's of desired depth to obtain the required momentum resolution and two-track separation. Such assemblies could be used not only for the two midrapidity TPC's but also for the Forward Arm Spectrometer tracking devices T1, T2 and possibly T3 .

Anode wire readout

The anode wire readout, previously used by another experiment (NA36)[1], consists of an anode plane divided into 10 identical rows located 2 mm above a solid copper cathode plane and 2 mm below a grid plane. Each row has 96 sense and field wires on a 2 mm pitch which are 20 μm and 50 μm in diameter, respectively. The gating grid, 8 mm higher, passes the drifting electrons for accepted events only and thus limits positive ion build-up in the drift volume.

Pad plane readout

In the high-field region close to the multiplying anode wire an avalanche takes place. The resulting electrons are quickly collected on the anode wire (~ 1 ns), whereas the more slowly moving positive ions induce image charges on the underlying pads (Figure 6.8). By recording the induced charge on the rows of rectangular pads at regular short time intervals by Flash Analog-to-Digital Converters (FADC) one achieves three-dimensional localization of the tracks. Typically, for each particle track, a cluster of about 3 to 5 pads in each pad row are involved in this process (Figure 6.9). For each track segment, the drift time from the primary ionization site to the anode wire yields the y coordinate (vertical), whereas the induced signals on the pad row yield the x (pad row number) and z (drift time) coordinates in the pad row plane (horizontal).

The pulse height distribution of the induced signal on each pad, z_i, of such a cluster depends on the distance of the pad from the centroid, z, of the cluster. The resulting pulse height distribution, the Pad Response Function (PRF), is approximated by the gaussian function P_i:

$$P_i = A \cdot e^{-\frac{(z-z_i)^2}{2\sigma_z^2}},$$

where z is the cluster centroid coordinate and z_i the location of the i-th pad of length l. The charge distribution width σ_z is a function of the drift length L_{drift} and the transverse diffusion constant D_{trans}, and depends on the angle α at which an incident particle crosses the pad row:

$$\sigma_z^2 = \sigma_{PRF}^2 + D_{trans}^2 \cdot L_{drift} + \frac{(\ell \cdot tan\alpha)^2}{12}.$$

σ_{PRF} is the intrinsic pad response width due to charges induced by a single anode wire on the underlying pads and depends mainly on the geometric configuration of the anode wire and pad planes. In our configuration with 2×15 mm^2 pads located 3 mm below the anode wire plane, this value is estimated to be $\sigma_{PRF} \approx 3.1$ mm.

A similar relation holds for the charge distribution in the y drift direction:

$$\sigma_y^2 = \sigma_o^2 + D_{long}^2 \cdot L_{drift} + \frac{(\ell \cdot tan\lambda)^2}{12},$$

where D_{long} is the diffusion constant in the longitudinal drift direction, λ is the angle of the particle trajectory to the $x-z$ plane (the dip angle) and σ_0 is the quadratic sum of a time slice of the FADC and the shaping time width (FWHM) of the preamplifiers:

$$\sigma_o^2 = \left(\frac{FWHM}{2.36}\right)^2 + \left(\frac{\Delta t}{\sqrt{12}}\right)^2.$$

The prototype is now undergoing a first series of tests with the following conditions:

- Argon-methane (90%-10%) gas mixture at 130 V/cm.
- 12.5 μm diameter anode wire.

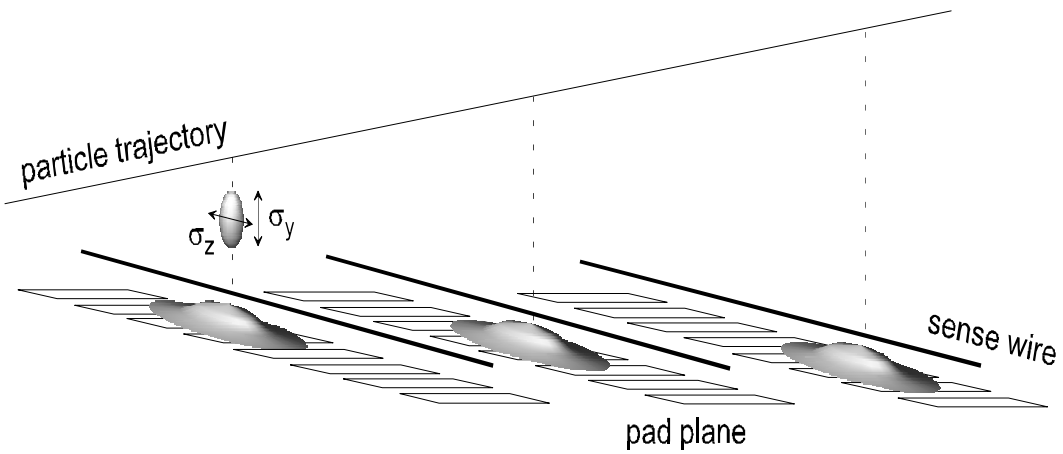

Figure 6.9: Typical geometry of the anode wires and pad rows with clusters.

- 3 mm cathode - anode wire gap, 3 mm anode wire - pad plane gap.
- 4 pad rows of 96 (2×15) mm^2 pads on a 4 mm pitch.

As an alternative to this rather conventional readout plane design, we are considering the use of a microstrip gas chamber (MSGC) analog design.[6] The multiplying anode wires are deposited atop a thin glass substrate, the pads being on the opposite surface of the substrate. Such an assembly could easily be reproduced as a large number of modules with minimum dispersion in geometric characteristics; furthermore, the smaller distance between anode and pad plane would improve the pad response function. A 50×50 mm^2 prototype has been build at GSI Darmstadt[4] following the original Oed[5] design with 8 μm wide anodes on a 1 mm pitch on a 300 μm glass substrate. A second prototype, different in the pad plane layout, is being designed at CRN Strasbourg where the MSGC technique has been used successfully[7]; nevertheless the achieved gas gain for stable operation has been limited as of this writing to a value of about 1000. Those prototypes will undergo extensive testing for pad response function and gain stability within the next two months. The size of the MSGC is as yet limited to 100×200 mm^2 by the available tools, and thus the readout plane would be constructed as an assembly of that size modules which does not carry further disadvantages.

6.3.2 Electronics

For the prototype tests we are using readout electronics which are similar to those used by the ALEPH and NA35 Collaborations (Figure 6.10), consisting of 16-channel preamplifier cards mounted directly to the TPC with their outputs led 4 by 4 via ∼40 m

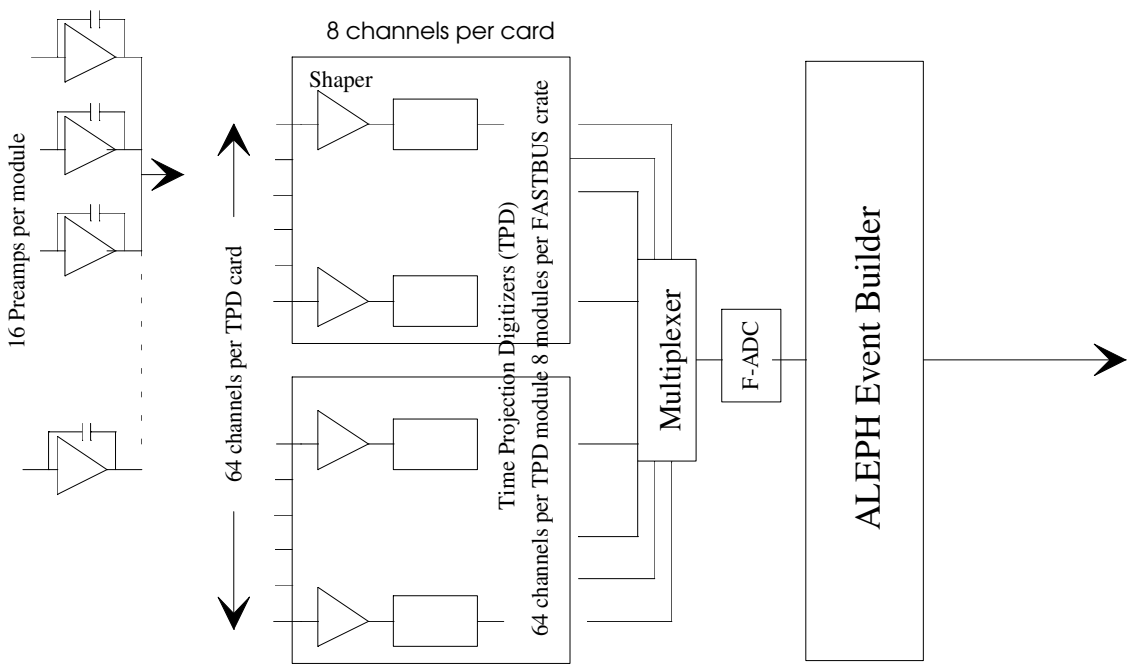

Figure 6.10: TPC readout electronics used by ALEPH and NA35.

long cables to Time Projection Digitizers (TPD) Fastbus modules. Each TPD module contains 64 shaping amplifiers and an FADC. A Fastbus crate contains 8 TPD's for a total of 512 channels and is read out by an ALEPH Event Builder (AEB). The FWHM of those shaping amplifiers is 180 ns and the clock frequency for sampling is 12.5 MHz, giving time slices of 80 ns width.

We are considering other highly integrated solutions for the final readout electronics to be used in the future: i) electronic systems designed at LBL for the NA49 and STAR Collaborations[3]; ii) new developments at the Laboratoire d'électronique et de Physique des systèmes Instrumentaux (LEPSI) at the University of Strasbourg.

The front end electronics (FEE) will be directly mounted on the TPC's read-out plane. Each $\approx 10 \times 10$ cm^2 FEE card holds 32 channels providing: charge sensitive preamplifier, shaping amplifier, 265-samples analog storage (Switched Capacitor Array) analog-to-digital converter, zero suppression and multiplexed transmitter to the VME data processing.

6.3.3 TPC Characteristics

Position resolution

The ionization along a particle track yields an average number, n_o, of electron-ion pairs per centimeter of track length. Landau fluctuations affect the charge distribution centroid position in the particle track direction x. Since one assumes the x coordinate of the projected track to be at the center of a pad one has to account for that centroid shift in the position resolution in both the y and z coordinates. This is taken care of in the angle-dependent terms of the charge distribution relations by an empirical term, n_{eff}, related to the number of electron-ion pairs which effectively reach a pad along its length. To estimate the position resolution of our prototype TPC, we will use the value $n_{eff} = 15$ previously determined for minimum ionizing particles in similar designs. The expected position resolutions are then:

$$\partial_z^2 = \frac{\sigma_{PRF}^2 + D_{trans}^2 \cdot L_{drift}}{n_o \cdot \ell} + \frac{(\ell \cdot tan\alpha)^2}{12 \cdot n_{eff}}$$

$$\partial_y^2 = \frac{\sigma_o^2 + D_{long}^2 \cdot L_{drift}}{n_o \cdot \ell} + \frac{(\ell \cdot tan\lambda)^2}{12 \cdot n_{eff}}.$$

Assuming for minimum ionizing particles $n_o = 90$, $n_{eff} = 15$, and using the estimated values for our prototype from Table 6.8, one obtains:

$$\partial_z^2 = (0.266mm)^2 + (0.047mm)^2 \cdot L_{drift} + (1.12 \cdot tan\alpha)^2 = (335\mu m)^2$$

$$\partial_y^2 = (0.358mm)^2 + (0.0095mm)^2 \cdot L_{drift} + (1.12 \cdot tan\lambda)^2 = (360\mu m)^2.$$

The prominent terms in the position resolution are the diffusion constants which could be reduced by using other gas mixtures but which would in turn require a shorter integration time in the shaping amplifiers. This would affect the formation of the output signals and result in a decrease of their amplitude if the drift velocity is not significantly decreased. Since the pad-crossing and dip-angles are rather small in our design, increasing the pad length could improve the position resolution (increasing the pad length by factor of 2 could improve the position resolution by a factor of $\sqrt{2}$.)

Coordinate determination

For each accepted event, before performing the track-finding procedure one has to extract the coordinates x, y and z from the recorded signals. The coordinate x is the pad row number and y is determined by a weighted average of the pulse height P_{ij} :

$$y = \frac{\sum_{i,j} y_j P_{ij}}{\sum_{i,j} P_{ij}}$$

where P_{ij} is the pulse height of time slice j on pad number i. The coordinate along a pad row z is generally obtained from a weighted mean of the Pad Response Function P_i:

$$z = \frac{\sum z_i P_i}{\sum P_i}.$$

The procedure may be slightly different if only two or three pads are in a cluster.

If the cluster contains only two valid pad signals P_1 and P_2, their distribution is fitted using the function:

$$P_i = A \cdot e^{-\frac{(z-z_i)^2}{2\sigma_z^2}}$$

and then:

$$z = z_i + \frac{\Delta}{2} + \frac{\sigma_z^2}{\Delta} \cdot \ln \frac{(P_{i+1})}{(P_i)}.$$

For example, in a simplified way:

$$z = z_1 + \frac{\Delta}{2} + \frac{\sigma_z^2}{\Delta} \cdot \ln \frac{P_2}{P_1}$$

where z_1 is the position of the first pad in the cluster, Δ is the pad spacing (pad pitch) and σ_{PRF} is set to the expected value for the present design (Table 6.8.)

For a three pad cluster one can fit σ_{PRF} or σ_z as well by using a similar function or by using the following relations:

$$z = z_1 + \frac{\Delta}{2} + \frac{\sigma_{PRF}^2}{\Delta} \cdot \ln \frac{P_2}{P_1} = z = z_2 + \frac{\Delta}{2} + \frac{\sigma_z^2}{\Delta} \cdot \ln \frac{P_3}{P_2} = z = z_1 + \Delta + \frac{\Delta}{2} + \frac{\sigma_z^2}{\Delta} \cdot \ln \frac{P_3}{P_2}$$

$$\sigma_{PRF}^2 = \Delta^2 / \ln \frac{P_2^2}{P_1 P_3}.$$

With these conditions and the present prototype the relevant parameters are given in Table 6.8.

6.3.4 TPC Simulations

The rapidity and transverse momentum acceptance of the mid-rapidity spectrometer has been evaluated for Au + Au ($\sqrt{s}$ = 200 GeV/nucleon pair) events generated by VENUS through GEANT simulations. In order to simulate the processes in a TPC, each particle track was followed into the TPC and hits were generated for each track segment crossing the active volume above a pad row. A set of x, y, z coordinates was attributed to every

Parameter	Value
D_{trans}	550 μm/$\sqrt{\text{cm}}$
D_{long}	350 μm/$\sqrt{\text{cm}}$
σ_{PRF}	3.1 mm
σ_0	80 ns ; 5.2mm
v_{drift}	52 μm/ns
$\left(L_{drift}\right)_{max}$	20 cm
l	15 mm
α_{max}	5°
λ_{max}	15°

Table 6.8: TPC parameters for the present prototype.

hit. From hit coordinates y and z, a cluster was generated, taking into account the charge distribution deduced from energy loss calculations including Landau fluctuations and the parameterization outlined in the previous section, depending on drift length and trajectory angles. From those cluster parameters a two-dimensional gaussian shape charge distribution was calculated. The corresponding digitized values were attributed to each pad and time slice (bucket).

Such simulations are used to check the track recognition and reconstruction algorithms versus momentum resolution and will be used to test the two-track resolution capabilities of the spectrometer. This is of special interest if one wants to perform HBT analysis in order to obtain information on the space-time dimension of an emitting source. The momentum resolution and the two-track separation will set a lower limit for measurements of the Lorentz-invariant four-momentum difference $Q_{inv} = \sqrt{\sum_{x,y,z}(p_{xi} - p_{xj})^2 - (E_i - E_j)^2}$ of two identical particles.

Track finding and reconstruction

The tracking in the TPC's is performed, for present purposes, by utilizing a program adapted from an existing program designed for a silicon telescope (by A. and M.E. Michalon) used in the WA97 Experiment. This Track Pattern Recognition (TPR) program is comprised of three successive executive procedures :

- TPH, which builds the hits from the measured digits.
- TPA, which performs the optimized track recognition.
- TPO, which extracts the TPA-analysis results and stores them in ZEBRA data banks.

The TPH Procedure

This program selects the raw data monitored by the pad monitor program and extracted from the various cathode-pad planes of the TPC. For each plane the raw data are stored and converted into hits characterized by their DRS (Detector Reference System) coordinates.

The TPA Procedure
The Final Cluster-Distribution Elaboration

The program proceeds first to a "cleaning" to simplify the adjacent hit distribution (cluster) in the following manner :

- For a low number of adjacent hits (≤ 3) they are merged into a single hit located at the centroid of the initial distribution.
- For a medium number (≤ 6) they are merged into several clusters reflecting the sub-structure of the initial distribution.
- For a large number (> 6) they are rejected (often resulting from tracks perpendicular to the longitudinal axis of the TPC's, δ-rays, etc.).

This defines the set of hits as illustrated in top frames of Figure 6.11.

Iterations are then performed on three subprocesses:

1. tolerance definition
2. track following
3. track road.

Pre-Processing of Hits in Following Tracks

This procedure is applied simultaneously to the $x-y$ and $x-z$ planes. Scanning starts from the back of the TPC (the last plane of hits) where the hit density is lowest. For each hit one defines a window F_0 by a cone with the apex located at the hit and whose opening angle (an adjustable parameter) is such that it covers the whole (or a large fraction) of the front face of the TPC. All the hits contained in this plane are analyzed separately and simultaneously in this way. Then, one scrutinizes the hits in the precedent (next to last) plane which are contained in the defined window. By analyzing the statistical distribution of these hit locations, one defines the most probable location

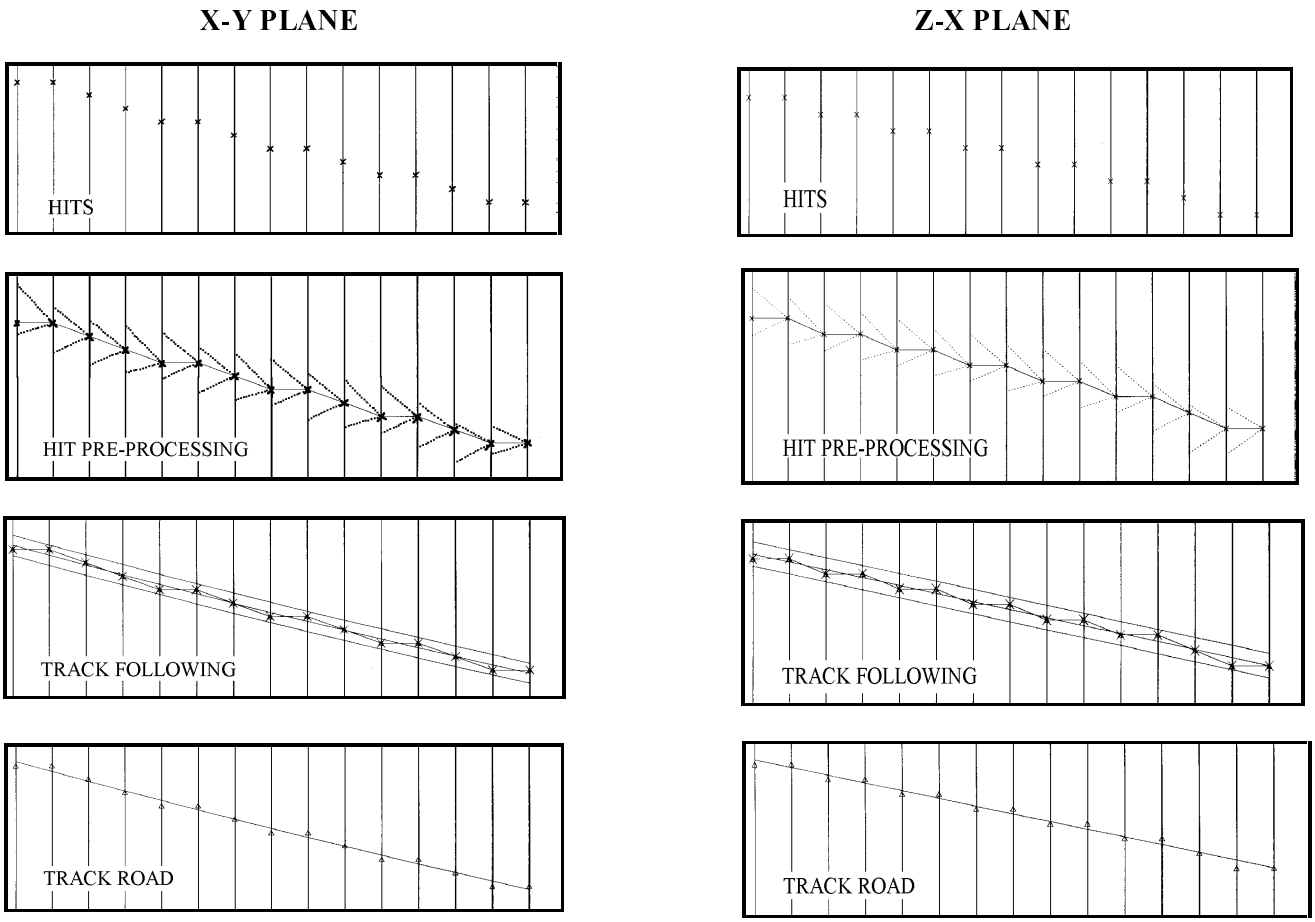

Figure 6.11: Illustration of the steps used in track finding and reconstruction.

(the centroid of the distribution) of the hit associated with that considered, as well as the opening of the next window F_1 (the width of the distribution). This defines a segment, a possible track-element, extending from the initial hit location to the new one found. The procedure is then iterated by considering next the plane immediately before, and so on. For each new plane the opening of the window is adjusted (i.e., reduced) accordingly. This procedure is illustrated in the second from top frames of Figure 6.11.

When one single initial hit is followed by a gap (no hit in the next plane) the process is aborted for this specific investigation. This, of course, is not relevant when a gap (or more) occurs after several hits, i.e., shorter tracks.

Following Tracks and Determining the Track Road

The aim is to determine the *most probable complete track* from the collection of segments obtained. Thus, the segments are associated to generate possible tracks and then they are sorted out. When several tracks share common hits these latter are associated with the longest track. Tracks with only few spare hits are eliminated. When hits are missing (no hits are close to the impact of the possible track) in a particular plane then ghost hits are created. In this way possible tracks are constituted with different level of confidence.

By linear fitting to the possible tracks and by adding a given variance (a parameter) to this fit, one determines a possible road as shown in the second from bottom frames of Figure 6.11. The number of hits included in the calculated road determines the quality of the result and whether a new iteration should be considered. Used hits in the track road determination are flagged and their number should be equal to the number of analyzed planes. Concretely the width of the road is increased until the number of hits remains constant and close to the number of planes. The final track, together with the initial hits, are shown in the bottom frame of Figure 6.11. Unused hits not belonging to the road under construction are restituted to be included in further analyses of other tracks.

6.3.5 Present Status

At this point the prototype TPC, including the two mentioned readout schemes, has been built at the Centre de Recherches Nucléaires, Strasbourg, France. Preliminary tests of the field cage and the readout systems have been satisfactorily achieved using radioactive sources (electrons and X rays).

For further testing, the prototype has now been moved to the Gesellschaft fur Schwerionen Forschung (G.S.I.) at Darmstadt, Germany. At present we have 512 channels of electronics (preamplifiers, TPD's) connected to a computer via an ALEPH Event Builder. Extensive tests using radioactive sources and laser beams have been undertaken in order to measure the basic performance in space resolution and two-track separation of the prototypes.

References

1. C. Garabalos, Nucl. Instrum. and Meth. **A283**, 553 (1989).

2. J. Va'vra, P. Coyle, J. Kadyk and J. Wise, Nucl. Instrum. and Meth. **A324**, 113 (1993).

3. A. Mock, Diplomarbeit, Technische Universitat Munchen.

4. H. Sahn, GSI, Darmstadt, private communication.

5. A. Oed, Nucl. Instrum. and Meth. **A263**, 351 (1988).

6. R&D-32 Status Report, CERN/DRDC 94-10.

7. A. Pallares *et al.*, Internal Report, CRN Strasbourg (1994).

Chapter 7

Particle Identification

The particle identification (PID) in BRAHMS is accomplished by a combination of time-of-flight and Čerenkov detectors. The momentum ranges to be covered in the forward arm and the mid-rapidity arm are different, but the techniques used for particle identification are similar. In both cases the lower K-p range is covered by time-of-flight, and the higher range by Čerenkov detectors. This chapter first gives an overview of the PID scheme in the forward and mid-rapidity arms followed by a more detailed discussion of the TOF design and tests, as well as the RICH detector.

7.1 Forward spectrometer

Particle identification in the forward arm spectrometer is done in two places:

- Between D2 and D3. This is needed for the low momentum part of the spectra where 1 GeV/c < $p \leq$ 5 GeV/c in the angular range 2°< θ < 18°, and is the only PID for 18°< θ < 35° where the measurements are done by the D1-D2 complex alone.

- After D4. This will cover the high momentum part of the spectra, i.e., $p \geq$ 5 GeV/c for the angular range 2°< θ < 18°

In both cases part of the particle identification can be done using time-of-flight measurements, but these will be augmented by Čerenkov measurements. The requirements for the two methods are coupled.

TOF Element	Distance From Vertex	Species Separated	Maximum p (GeV/c) 5σ cut	4σ cut	3σ cut
H1	9 m	π/K	2.9	3.3	3.8
		K/p	5.0	5.7	6.5
H2	20 m	π/K	4.4	5.0	5.8
		K/p	7.4	8.5	9.7
TOFW (midrap.)	4 m	π/K	1.9	2.2	2.5
		K/p	3.3	3.7	4.3

Table 7.1: Dependence of the performance of the various TOF detectors on the cut in number of σ. The value $\sigma = 75$ ps is assumed.

H1

The low momentum PID is done after the dipole D2. At 9 meters from the interaction point the time-of-flight hodoscope H1 can discriminate pions from kaons and protons depending on the time resolution that can be achieved. The expected performance of this detector is listed in Table 7.1. It will consist of 40 staves of size $1 \times 1 \times 25$ cm^3. They will be instrumented by fast photomultipliers mounted at each end, and both time and pulse height information will be read out.

C1

A segmented Čerenkov counter, C1, with C_4F_{10} as radiator gas at 1 atm. can extend the pion identification all the way up to 9 GeV/c, but a gap in the K/p separation will be present between 5.7 (for the 4σ cut) and 9 GeV/c. A segmentation of 8 (two cells along y and four along x) suffices for this counter.

The light collection scheme is shown schematically in Figure 7.1. Each cell is defined optically by a flat mirror angled at 45 degrees to the horizontal and by truncated pyramids which channel the Čerenkov light onto a 3-inch diameter photomultiplier. A prototype of this detector was tested recently[1] and it was found that with a 60 cm radiator length of C_4F_{10} and an RCA8854 photomultiplier, a saturated light yield of some 20 photoelectrons was observed. It was also found during these tests that the background from scintillation was minimal.

The BRAHMS Monte Carlo program was used to evaluate the number of "confusing" events with two particles in one cell. One of those particles has its momentum above threshold and the other below and does not produce any light. The information from this particular cell will then be of no use to extract the identity of the particles because H1 and C1 would not be able to indicate which one of the particles was the one that produced light in the Čerenkov counter. Events with these type of pairs were counted for a setup where the Forward Spectrometer was the closest to the beam, i.e. 2 degrees. The fraction of events with confusing pairs at 2 degrees was found to be equal to 8%, but if the second time-of-flight wall H2 is also taken into account, some of the confused

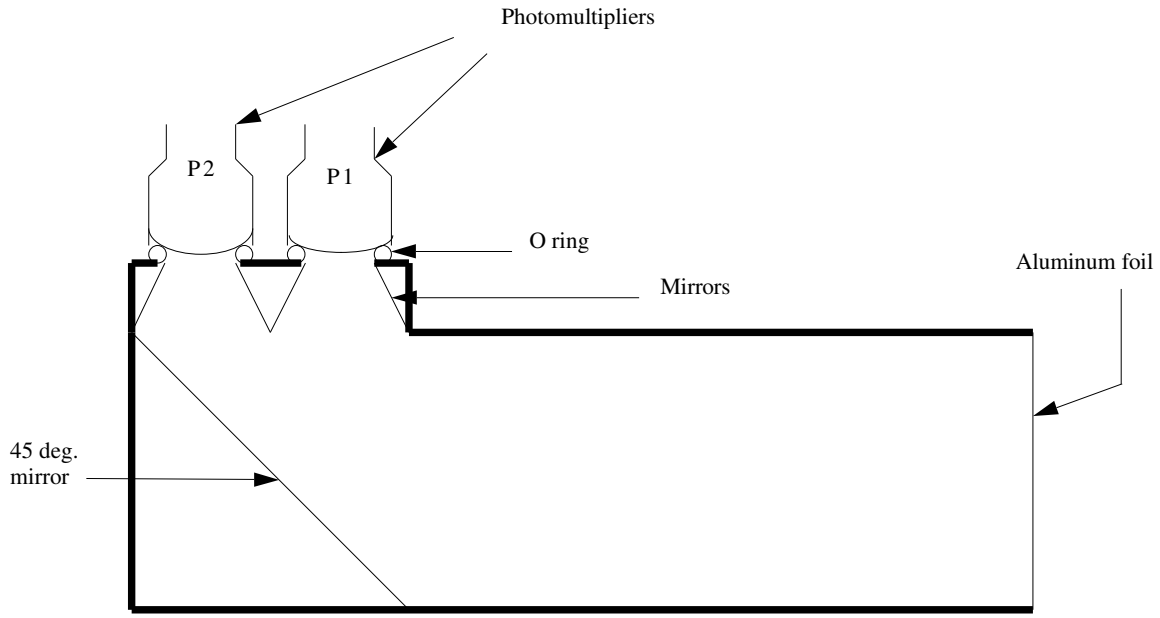

Figure 7.1: Schematic view of the C1 Čerenkov counter. This is a side view, showing how the 45° mirror and photomultipliers P1 and P2 define two cells displaced in the vertical direction.

particles can be identified by time-of-flight, and the fraction of events with unresolved pairs becomes equal to 5%.

H2 and RICH

The high momentum PID will be done with the hodoscope H2, placed 20 meters away from the interaction point and immediately after the tracking detector T5, and with a RICH counter placed after H2. Hodoscope H2, whose performance is listed in Table 7.1, will consist of 20 staves of size $1 \times 2 \times 40$ cm^3, each instrumented by fast photomultipliers mounted at both ends, with time as well as pulse height information read out. The design criteria, expected performance and details of the RICH detector are described below.

Acceptance

The particle identification as done by the different detectors is displayed in Figure 7.2 for the π–K separation and in Figure 7.3 for the K-p separation.

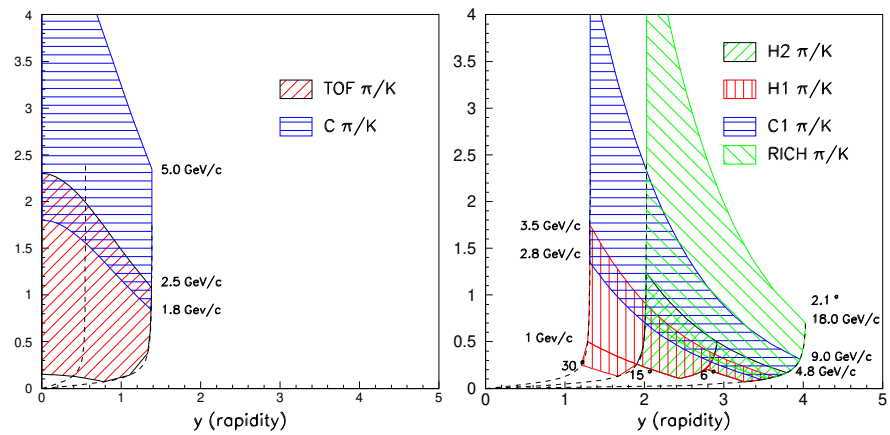

Figure 7.2: Acceptance for pions in the midrapidity (left frame) and forward (right frame) arms. The different shaded areas indicate which detector performs the PID.

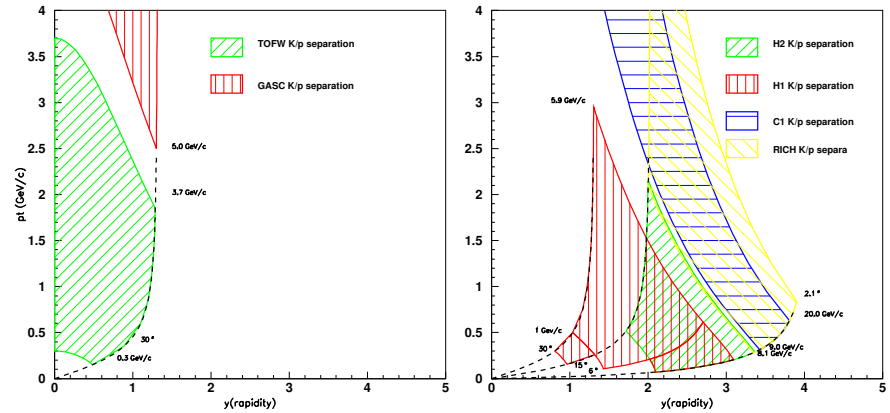

Figure 7.3: Separation of kaons and protons in the midrapidity (left frame) and forward (right frame) arms. The different shaded areas indicate which detector performs the PID.

7.2 Midrapidity spectrometer

The particle identification in the midrapidity spectrometer is designed to be relatively simple. It consists of a time-of-flight wall (TOFW) followed by a segmented threshold Čerenkov detector (GASC), as indicated in Fig. 3.1. The TOFW is 4 meters away from the interaction vetex. With an assumption of 75 ps in overall timing resolution, which is reasonable from recent beam tests, the range of charged hadronic particle separation is given in Table 7.1 under various cut criteria, indicating 4σ separation of K-π up to 2.2

GeV/c and K-p up to 3.7 GeV/c. These momentum ranges contain most of the yield for the particles concerned. However, particles with higher momentum, although few in number, could have different spectrum shapes, revealing unique information on the reaction dynamics.

The GASC detector is proposed to extend the momentum range for particle identification beyond that of TOFW. With Freon-12 gas at 4 atm pressure, pions up to 5 GeV/c, kaons up to 3.7 GeV/c and protons up to 11 GeV/c will be identified. Between 3.7 and 5.0 GeV/c, protons could be contaminated to various degrees by unidentified kaons in the momentum range.

With the center of the midrapidity spectrometer at 34 degrees, the hit probability on TOFW by charged particles, both primary and secondary, is shown in Fig. 6.5, with each TOFW slat 0.6 cm wide and 22 cm high. The calculation is performed for central Au+Au collisions generated by VENUS. The probability is the highest in the middle of the wall and gradually falls down towards both ends. With the same calculation, it is seen that the average multiplicity for charged particles of momentum above the pion threshold (1.6 GeV/c) in the GASC detector is 0.7, posing no special problems for conventional designs of segmented gas Čerenkov counters. A similar, but smaller, design of the successful GASC detector in E-802 at the AGS could be implemented. A segmentation of 20 cells would be more than enough and is very feasible. The segmentation can be achieved optically with flat mirrors and cones for channeling light onto the nearby photomultipliers. In order to make the optical segmentation work correctly, the length of the radiator should be less than 50 cm and the figure of merit N_0 should be close to 90 cm^{-1} in order to get a saturated light yield of some 30 photoelectrons.

7.3 Time-of-flight

Time-of-flight detection is an important part of the BRAHMS particle identification scheme. The forward arm spectrometer uses two time-of-flight walls, H1 and H2, and the midrapidity arm spectrometer uses one, TOFW.

7.3.1 TOFW design

Due to the large multiplicity even in the midrapidity spectrometer at 30 degrees, the TOF wall proposed for the midrapidity spectrometer has to be adequately segmented. Given the present layout of the midrapidity spectrometer, it is desirable to make the individual slats as thin as possible while keeping a reasonable timing resolution ($\leq$ 75 ps). Thinner slats will have less energy deposited by charged particles, and hence larger fluctuations in timing.

We have chosen 22 cm for the height of the TOF wall, and 160 cm for the width. Based on a simulation performed with the midrapidity spectrometer at 34°, the width of the scintillators should be 0.6 cm or smaller.

The proposed arrangement for the phototubes and scintillators on the staves is shown in Fig. 7.4. Light guides direct the photons through a 30° angle to the phototubes at each end. The positions of the light guides are staggered in the assembled wall so as to allow maximum space between neighboring phototubes, as shown in the figure.

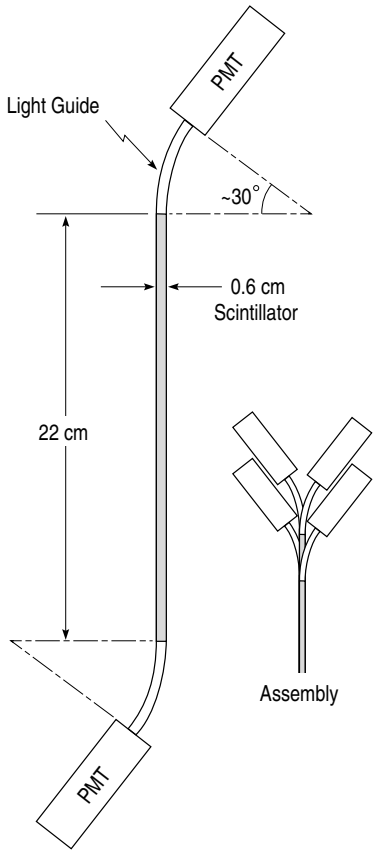

Figure 7.4: Arrangement for mid-rapidity TOF wall staves.

7.3.2 TOF tests

Prototype TOF modules have been studied with the AGS test beam. Two types of scintillators were tested: BC404 0.6×0.6×22 cm^3 (Type I), and BC404 0.4×0.4×22 cm^3

Tube	Peak Wavelength (nm)	Rise Time (ns)	Transit Time (ns)	Current (amp)	Price ($)
R1635	420	0.8	7.8	1.0×10^6	427.
R3478S	420	1.3	14.	2.1×10^6	516.

Table 7.2: Characteristics of different phototubes for the TOF.

(Type II). Lucite light guides 6 cm long, matched in cross-section to the scintillator and bent approximately 30 degrees were glued to the end of the scintillators and attached to the phototubes with optical grease. On-Tube-Discriminators from the University of Tsukuba developed for E–866 were connected to the ends of the 3/4-inch phototubes (R3478S) on the Type I scintillator, and a Phillips 8-channel NIM discriminator module was used 50 ft away from the 1 cm tubes (R1635) for the Type II scintillator. Properties of the phototubes tested are given in Table 7.2. The beam particles were mainly 2 GeV/c negative pions. A tiny scintillator (0.5×0.5 cm^2) was placed behind the TOF modules under test and used in conjunction with another 2×2 cm^2 scintillator upstream to define the trigger in order to select beam particles in a small position and angle dispersion. Both ADC's and TDC's were read out by a Macintosh-based data acquisition system.

The timing resolution was analyzed by setting gates of small ranges on the ADC's in order to correct the slewing effect due to the finite rise time of the phototubes. Timing differences between the two tubes on each end of the scintillator, $dt = 0.5 \times (TDC_{up} - TDC_{down})$, were fitted with gaussian distributions, with σ being 61 ps for Type I and 62 ps for Type II. This indicates the timing resolutions for the two types of setup are very similar, in spite of the different scintillator cross-sections, phototubes, and discriminators. The timing resolution between the two scintillators,

$$d(tof) = 0.5 \times (TDC_{up} + TDC_{down})_1 - 0.5 \times (TDC_{up} + TDC_{down})_2 \ ,$$

fits a gaussian distribution with $\sigma = 87$ ps. By assuming both scintillators have the same intrinsic timing resolution, the intrinsic timing resolution for each scintillator is calculated to be $\Delta t = 87/\sqrt{2} = 62$ ps.

In conclusion, intrinsic timing resolution around 60 ps can be achieved by the small scintillators we propose for the BRAHMS Experiment. Depending on the intrinsic timing resolution of the start counters, an overall timing resolution of 70 ps is achievable.

7.4 RICH detector

As described in the PID overview an important part of the high momentum particle identification is performed by a RICH (Ring Imaging CHerenkov) detector. RICH counters are powerful tools for achieving particle identification over a wide range of momentum

within a single detector. The experience of the SLD[2] and DELPHI[3] Collaborations in developing broad-range detectors has shown that π/K/p separation can be achieved up to approximately 30 GeV/c and e/π separation can be performed up to 5 GeV/c. There is also the capability of handling modest multiplicities within the detector. For reviews on the subject, see Refs. 4 and 5.

For a given particle the frequency distribution of Čerenkov radiation, $dN/d\nu$, is constant for all frequencies, ν, leading to several possible photon detection schemes. Existing RICH counters generally detect the Čerenkov photons in the UV region (6.5 – 7.5 eV) by means of photoionization of a complex organic molecule, such as TMAE or TEA, in a proportional gas chamber. Alternatively, a segmented optical readout based on an array of photomultipliers offers three main advantages over the gas-based drift chamber:

1. No special handling for hazardous materials such as TMAE.

2. The possibility of readout fast enough for first-level triggering.

3. Greater overall efficiency due to larger bandwidth (2.5–4.3 eV).

As shown in Fig 3.1 the time-of-flight wall H2 is at a distance of 20 m from the vertex. At the 3σ level (where σ = 75 ps) it separates π/K up to p = 5.8 GeV/c and K/p up to p = 9.7 GeV/c (see Table 7.1). Using the criterion that two decades of coverage in the inclusive invariant cross-section are required, the RICH detector must separate π/K up to 20 GeV/c and K/p up to ≈30 GeV/c at the 2° polar angle setting (see Chapter 3).

For the RICH counter, located just behind H2, it is proposed to have 1.5 m of C_4F_{10} radiator at 1.25 atmosphere pressure (n = 1.00185). This choice of radiator allows overlap of coverage with the TOF system and determines the resolution in ring radius, $\Delta r/r$, required to obtain the desired momentum coverage. The Čerenkov photons are focused by a spherical primary mirror with radius of curvature R = 3.0 m (i.e. focal length f = 1.5 m) onto the focal-plane. The photons are detected by four segmented 10×10 cm^2 multi-anode photomultipliers arranged in a tightly packed manner. Each photomultiplier comprises a subarray of 10×10=100 pixels (each 1 cm^2 in area), representing a total segmentation of 400 pixels. The trajectories of the incoming charged particles will be known from the tracking in the Forward Spectrometer, and thus the position of the center of each Čerenkov ring may be deduced. In addition, the momentum of each tracked particle is also measured; thus it is sufficient to discriminate between known ring radii in order to perform the π/K/p particle identification.

It is important to note that the expected multiplicity of charged particles through the RICH counter is low. This has been confirmed by GEANT simulations of several hundred events generated by Venus and tracked through the BRAHMS Forward Spectrometer. Only particles which entered through the front-face of the spectrometer were tracked; thus the analysis was not concerned with background particles generated, for example, in the beampipe or the air. The RICH detector is far enough away from the beampipe that this is likely not a concern. The estimated multiplicities are given in Table 7.3.

	Hits per event p=7.5-15 GeV/c	Hits per event p=15-30 GeV/c
Primary	0.9	0.29
Secondary	0.5	0.39
Above threshold	0.8	0.30

Table 7.3: Average charged particle hits in the RICH detector

As can be seen from the table the proposed RICH counter will have to deal with at most a few particles per event. Typically, the tracks will be separated in angle by $\sim$2.0° in the bend plane and $\sim$0.5° in the non-bend plane which leads to a displacement of the ring center of $\sim$1 cm, enough to distinguish the individual particles.

Arrays of single-anode PMT's have been used successfully in previous RICH counters[7], but state-of-the-art multi-anode PMT's offer the advantage of many channels with a single common power supply and a compact readout. A working prototype counter has performed well in the AGS test beam and proven the multi-anode PMT technique (see Appendix A.)

7.4.1 Design Requirements and Detector Performance

The principal features of a RICH detector satisfying the design considerations outlined above are shown in Fig. 7.5. The radiator volume is filled with C_4F_{10} which, at a temperature of 20°C and 1.25 atm pressure has an index of refraction of n=1.00185. Reaction products π, K and p emerging from the exit aperture of D4 (h×w=40 cm×50 cm) pass through the volume, entering and exiting via the aluminum-alloy windows ($<$ 250 mg/cm^2). Čerenkov radiation produced along the 1.5 m path length (i.e. before the mirror) is focused by the spherical concave mirror (focal length f = 1.5 m) on the focal-plane detector as shown. The mirror itself has been rotated by an angle $\alpha = 8°$ about a horizontal axis through its center, thus shifting the ring image by an angle $2\alpha = 16°$. This places the ring image outside the radiator volume so that the primary particle flux cannot produce Čerenkov light in the glass walls of the photomultipliers.

Before proceeding to further discussion of the reason for various design features, it should be emphasized that the design illustrated can be constructed with components presently available. Key elements of the design, specifically the photon imaging detector, mirror and radiator gas, have been successfully tested in beam using the prototype RICH detector of BNL RD-44 with runs in 1992, 1993 and 1994. (For details see Appendix A.)

The focal plane detector consists of four Hamamatsu H-4945 multianode photomultipliers situated as indicated in Fig. 7.5. Each PMT consists of a 10×10 array of 1

cm^2 pixels mounted in a glass envelope of 12.8×12.8 cm^2 outside dimensions. Thus the outside dimensions of the focal-plane detector system are 25.6×25.6 cm^2 and the active area measures 22.8×22.8 cm^2 with a central dead region resembling a cross, as shown, of about 2.8 pixels in width. A vacuum seal on the four phototubes is used to constrain the radiator gas to the interior of the RICH vessel.

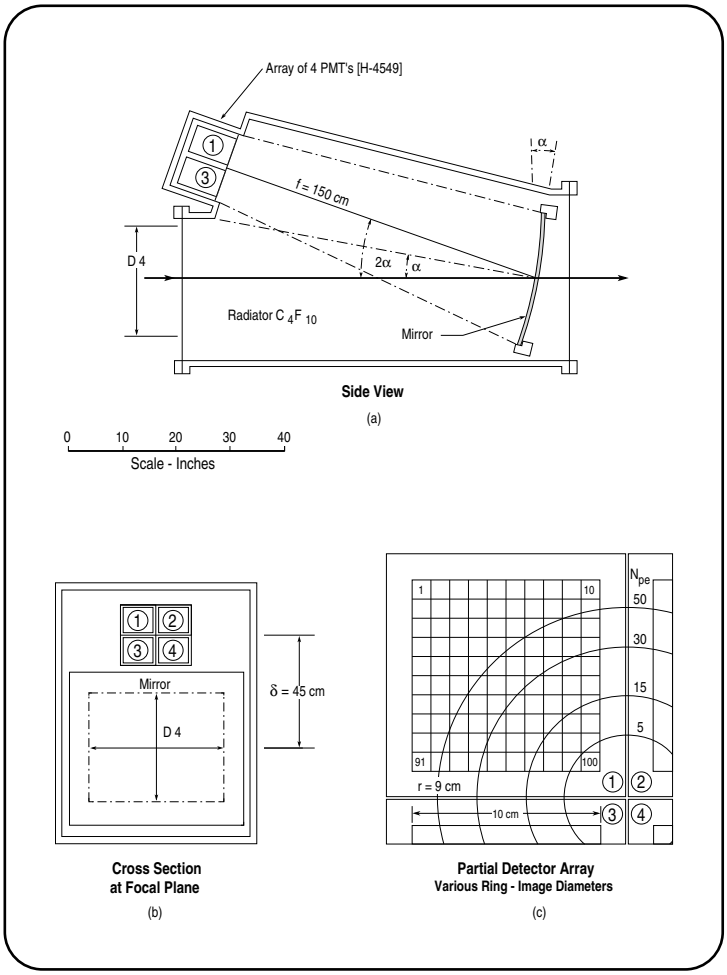

Figure 7.5: Schematic outline of RICH detector

Performance Characteristics

General

For a charged particle of velocity $\beta = v/c$ travelling through a medium with index

of refraction n, the Čerenkov angle for photon emission is given by

$$\theta = \cos^{-1}(1/\beta n) \ .$$

The radius of the ring-image at the detector focal plane is $r = f \tan\theta$. The number of detected photons may be written as[9]

$$N_{detected} = N_0 \, L \, \sin^2\theta \ ,$$

where L is the pathlength, in cm, and N_0 is the quality parameter of the counter, which is related to the integral over the photon energy, E, of the detector quantum efficiency $\epsilon(E)$ by:

$$N_0 = 370 \ (\text{cm eV})^{-1} \, \epsilon_m \int \epsilon(E) \, dE,$$

where ϵ_m is the reflection efficiency of the spherical mirror = 90%. For the Hamamatsu detector H-4549, the integral of $\epsilon(E)$ over E has the value 0.33 eV, and thus N_0=110 cm^{-1}.

Figure 7.6 shows plots of the ring radius, r, versus particle momentum, p, for pions, kaons and protons. Panel (a) uses the value N_0=110 cm^{-1} given above, while panel (b) assumes, as a worst case, the value N_0=55 cm^{-1}. Confidence contours at the 3σ level are included, where $\sigma = 0.0505/\sqrt{N_{pe}}$ and N_{pe} is the mean number of detected photoelectrons (see discussion below.) Also illustrated are the 3σ limits for π-K and K-p separation by the time-of-flight hodoscope H2. Even for the pessimistic N_0=55 cm^{-1} case, the RICH counter is expected to extend the particle identification from H2 to >20 GeV/c for π-K and to >35 GeV/c for K-p.

The right-hand scales of Fig. 7.6 show the expected mean number of detected photons for rings of different radii. The first column of numbers assumes the full detector coverage over the focal plane. The numbers in parentheses are acceptance-corrected for the inactive region as shown in Fig 7.5.

Detector Resolution: Aberrations and Pixel Size

It is evident from Fig 7.6 that the most stringent test of the detector resolution occurs in the momentum range p=20–30 GeV/c where it is essential to distinguish, on the basis of the measured ring radius r, the character of the particle as a pion or a kaon. In the following, it should be remembered that since $\theta = \cos^{-1}(1/\beta n) \leq 0.006$ rad $\ll 1$, we have $\tan\theta \approx \theta$ and thus the relationship between θ and r is $\theta = r/f$. This implies that the fractional uncertainties $\Delta\theta/\theta$ and $\Delta r/r$ are equal within negligible errors. The center of the ring distribution, in conjunction with the tracking information, is accurately determined. The uncertainty in an *individual* photoelectron hit position can be written as

$$\left(\frac{\Delta\theta}{\theta}\right)^2 = \left(\frac{\Delta\theta}{\theta}\right)^2_{\text{chromatic}} + \left(\frac{\Delta\theta}{\theta}\right)^2_{\text{geom}} + \left(\frac{s}{r\sqrt{12}}\right)^2 \ .$$

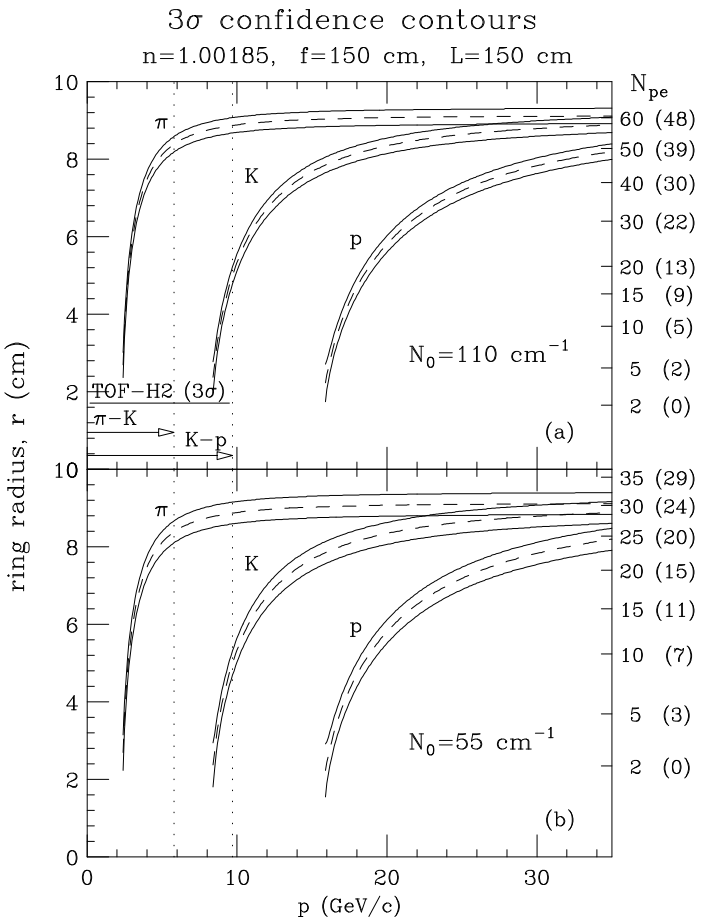

Figure 7.6: Ring radius and number of photoelectrons versus momentum. The number of photoelectrons given in parentheses are for the active area only.

The first two terms on the right express, in order, the effect of chromatic and geometric (optical) aberrations; the last term accounts for the finite pixel size, s, with the factor $\sqrt{12}$ arising from the r.m.s. error on the radius from assuming the position of the center of the pixel. We now evaluate these terms in the high momentum limit of β=1 for the parameters specified above and in Fig 7.6a.

Aberrations

The chromatic aberration is irreducible, in the sense that it follows directly from the choice of radiator gas. In a C_4F_{10} radiator at 1.25 atmosphere, the chromatic aberration is calculated[9] to be

$$\left(\frac{\Delta\theta}{\theta}\right)_{\text{chromatic}} \approx \frac{1}{2}\frac{\Delta n}{n-1} = 0.0315 \ .$$

In the above $\Delta n/(n-1)$ is simply the fractional change in the index of refraction over the 1.8 eV bandwidth of the photon detector.

The geometric aberration depends on the details of the RICH detector geometry, particularly on the ratio $x = \delta/R$, where R is the radius of curvature of the spherical mirror and δ is the perpendicular displacement of the focal plane detector from the particle trajectory axis. The geometric aberration is given by:

$$\left(\frac{\Delta\theta}{\theta}\right)_{\text{geom.}} = \left\{(n-1)\sqrt{3} \oplus \frac{\sqrt{42(n-1)}}{7} \cdot x \oplus x^2\right\} = 0.0235 \ ,$$

where $\oplus$ indicates addition in quadrature. Here we have used the case of a particle trajectory passing through the center of the spherical mirror shown in Fig. 7.5; thus $\delta = f \sin 2\alpha \approx 45$ cm, with the resulting value x=45/300=0.15. The x^2 term clearly dominates the expression for $\Delta\theta/\theta$.

Pixel Size

The last term specifies the fractional contribution to the net uncertainty (for a single hit) due to the fact that the pixel size, s, may represent a significant fraction of the ring radius, r. For fully relativistic particles the ring radius is 9.1 cm, compared to the pixel dimension of 1 cm, and thus

$$\left(\frac{s}{r\sqrt{12}}\right) = 0.0317$$

.

Net resolution

Combining the results for β=1 particles, such as 25 GeV/c pions, we compute the fractional uncertainty

$$\frac{\Delta\theta_\pi}{\theta_\pi} = \sqrt{.00255} = 0.0505$$

or $\Delta\theta_\pi = \theta_\pi \times 0.0505 = 0.00306$.

A figure of merit for distinguishing π from K may now be written as

$$n_\sigma = \frac{\theta_\pi - \theta_K}{\sqrt{\Delta\theta^2/N'_{pe}}} \ ,$$

where n_σ is the number of standard deviations separating π from K. Here N'_{pe} is the minimum number of detected detected photons, which is taken as $N'_{pe} = N_{pe} - 2\sqrt{N_{pe}}$.

From Fig 7.6a with p=25 GeV/c, N_{pe} =48 implying N'_{pe}=34, and finally

$$n_\sigma = 6.5 \ ,$$

i.e., the determined radius is more than six standard deviations away from what might be expected from a kaon.

7.4.2 Expected performance

Simulated images of Čerenkov rings on the focal-plane of the RICH detector are shown in Fig. 7.7. Panel (a) shows that a high momentum (18 GeV/c) pion may be discriminated from a kaon or proton by the observed ring radius. The ring from a 10 GeV/c kaon is also easily seen (in Fig. 7.7b) despite the dead space between the photomultiplier tubes. Finally, Fig. 7.7c shows two overlapping pion rings which may be readily separated and identified.

In order to understand better the real pattern of rings expected behind the forward spectrometer, Monte Carlo simulations were performed. Central Au+Au events produced by Venus were run through the forward spectrometer with the code GEANT, and the RICH rings, if any, from primary and secondary (background) particles were then generated. Fig. 7.8 summarizes a key feature of the results, namely the distribution of the ring centers in the focal plane. Fig. 7.8a shows that the positions of the ring centers from "good" primary particles are concentrated in a narrow horizontal band (along the bend-plane of the spectrometer magnets) at the center of the acceptance. Ring centers from background secondary particles, however, are scattered more or less randomly throughout the acceptance, as seen in Fig. 7.8b. This fact greatly aids in reconstructing the good rings since the background rings generally do not appear fully in the active area of the focal-plane.

The event ring patterns output by the Monte Carlo calculation were visually scanned in order to determine the reconstruction efficiency. In a study of 100 events with the forward spectrometer at the 2 degree, 7.5-15 GeV/c setting and with the RICH parameters set at (the not quite final values of) n = 1.00175, N_0 = 100 cm^{-1}, L = 100 cm and f = 150 cm, all the rings of 96 events were successfully found and identified. Since random "noise hits" were not included in the simulation, it is important to prove that we have conservatively designed the RICH counter in terms of the photon yield. To this end, a separate Monte Carlo run was performed with the quantum efficiency at half the expected value, i.e., with N_0 = 50 cm^{-1}. In this case the ring reconstruction efficiency found by visual scanning was almost unchanged: 93/100 of the events were complete successes.

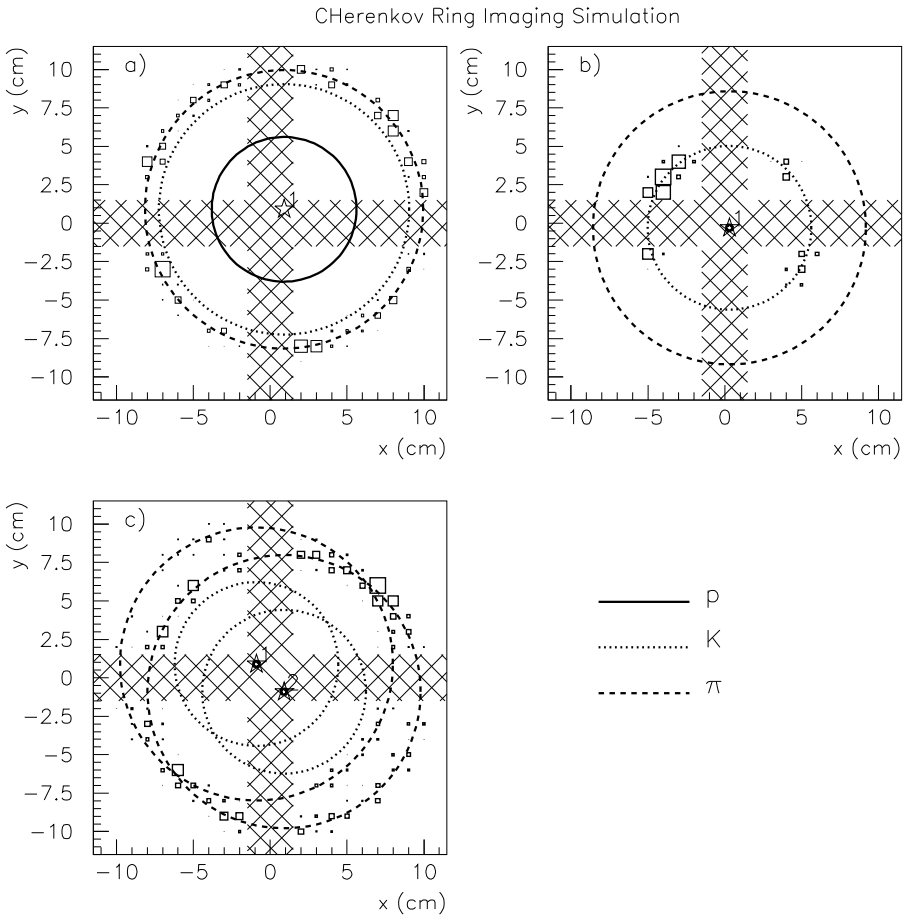

Figure 7.7: Simulated ring patterns for the RICH detector focal-plane with $n = 1.00185$, $N_0 = 110$ cm^{-1}, $L = 150$ cm and $f = 150$ cm. The sizes of the boxes indicate the pulse height on active pixels (1×1 cm^2 each) with the cross-hatched area being dead. Independent tracking yields the ring centers (stars) and momenta, which imply the drawn circles for different particle species. Panel a shows an 18 GeV/c pion, panel b shows a 10 GeV/c kaon, and panel c shows two 10 GeV/c pions.

7.5 References

1. R. Debbe, et al., Report on tests of detector prototypes for the extended PID of E866, internal E866 memo E-866-MEM-10, 1994.
2. V. Ashford, et al., presented at the XXIII Int. Conf. on High Energy Physics (Berkeley, CA, July 16–23, 1986) SLAC-PUB-4046; V. Ashford, et al., IEEE Trans. Nucl. Sci. **NS-34**, 499 (1987).
3. DELPHI Collaboration, Nucl. Instrum. and Meth. **A303**, 233 (1991).
4. T. Ypsilantis, Proc. of the Symposium on Particle Identification at High Luminosity Hadron Colliders, T. J. Gourlay and J. G. Mofin, ed., Fermilab, p. 133

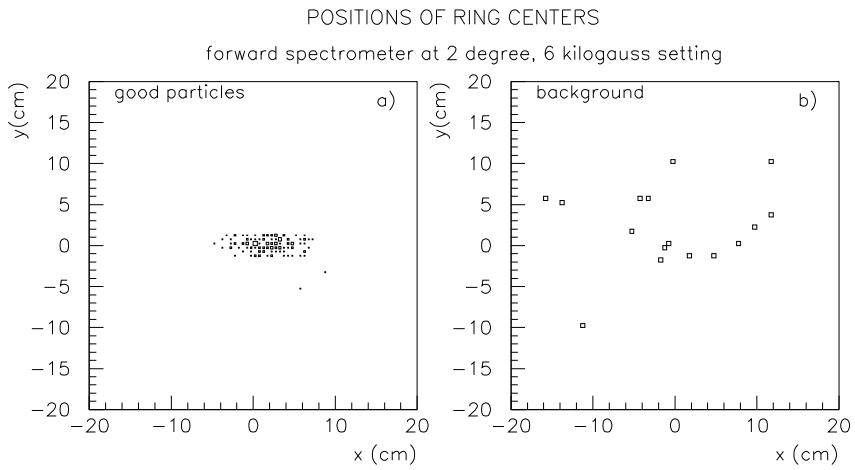

Figure 7.8: Position of the ring centers for good primary particles (panel a) and for secondary background tracks (panel b) from a GEANT simulation of 145 Venus central Au+Au events through the BRAHMS forward spectrometer at the 2 degree, 7.5-15 GeV/c setting.

(1989).

5. D. Leith, Nucl. Instrum. and Meth. **A265**, 120 (1988).
6. T. Sugitate, et al., Nucl. Instrum. and Meth., **A307**, 265 (1991); S. Endo, et al., "A Test of an Improved RICH Prototype", Institute for Nuclear Study (Tokyo) Annual Report, 1990.
7. See, e.g., Proc. of the Seminar held on the Occasion of the 50th Anniversary of the Discovery of Vavilov-Čerenkov Radiation, P. Carlson, ed., Nucl. Instrum. and Meth. **A248** (1986).
8. D. Beavis, et al., RHIC Letter of Intent #8, Brookhaven National Laboratory, 1990; Addendum to RHIC Letter of Intent #8, Brookhaven National Laboratory, 1991.
9. T. Ekelof, "The Experimental Method of Ring-Imaging Cherenkov (RICH) Counters", lecture given at the 1984 SLAC Institute on Particle Physics, 23 July–3 August 1984, CERN-EP/84-168.

Chapter 8

Global Detectors

In addition to the two small solid-angle spectrometers, BRAHMS will employ beam-beam counters and a centrality detector to characterize collisions from a global perspective and to form zero and first level triggers. The beam-beam counters will provide the start time for the time-of-flight measurements as well as determining the vertex position to an accuracy of order 1 cm. The centrality detector will measure the centrality ("impact parameter") of collisions by recording a related quantity, the charged particle multiplicity at midrapidity; additional information from the beam-beam counters complements this coverage.

8.1 Beam-Beam Counters

The BRAHMS beam-beam counters will consist of two arrays of Čerenkov detectors with one array located on each side of the intersection region as is shown in the detail of Fig. 5.1. These counters will provide the start timing for time-of-flight measurements, sample $dn/d\eta$ at high η, and provide initial vertex determination. Similar systems have been discussed for the other RHIC experiments. In this section we will discuss the design parameters for the BRAHMS Experiment.

The design constraints of the beam-beam counter system for BRAHMS are dominated by the need for a good timing start for the spectrometers. The detector modules are designed to detect the Čerenkov light from $\beta = 1$ charged particles. Placement of the counters in a region of high η ensures that most of the particles have β near 1, enabling an array with a reasonable number of modules to efficiently provide a timing start. Each module will consist of a lucite radiator attached to a good timing photomultiplier. The

radiator must be sufficiently thick (2-4 cm), such that a $\beta = 1$ charged particle will have a timing resolution of 50 ps. Multiple particles striking a single module may compromise the ability to provide good timing. Estimates of 10 hits per module for central Au+Au collisions have been considered for various system designs, where the region of pseudo-rapidity is spanned by only a small number of counters. To avoid this potential problem, we will sparsely sample a region of η ensuring that several counters have only one or two hits for the most central events. For a fixed number of counters, sparse sampling has the disadvantage of introducing an inefficiency at lower multiplicities. We will illustrate this with a preliminary detector layout.

Fig. 8.1 shows the front view of the two beam counter arrays. The left array has 40 modules sampling η from 3.0 to 4.5. The right array has 35 modules and samples the opposite η region but with reduced azimuthal coverage since magnet D1 is on the opposite side of the beam pipe. A higher spatial density of modules has been used in the right array to partially compensate for the reduced azimuthal coverage. The dots shown in Fig. 8.1 represent the expected charged particle hit density. Four different module sizes are used in the arrays. The larger modules use a two-inch Hamamatsu fast timing tube (R2083) with either 2- or 2.5-inch diameter lucite radiators. The smaller modules use a 0.75-inch diameter Hamamatsu tube with lucite radiators of diameter 0.75 or 1.0 inches. Prototypes of these modules will be tested to ensure that they provide the desired 50 ps timing resolution. The array-geometry will later be refined based on the results of the prototype tests.

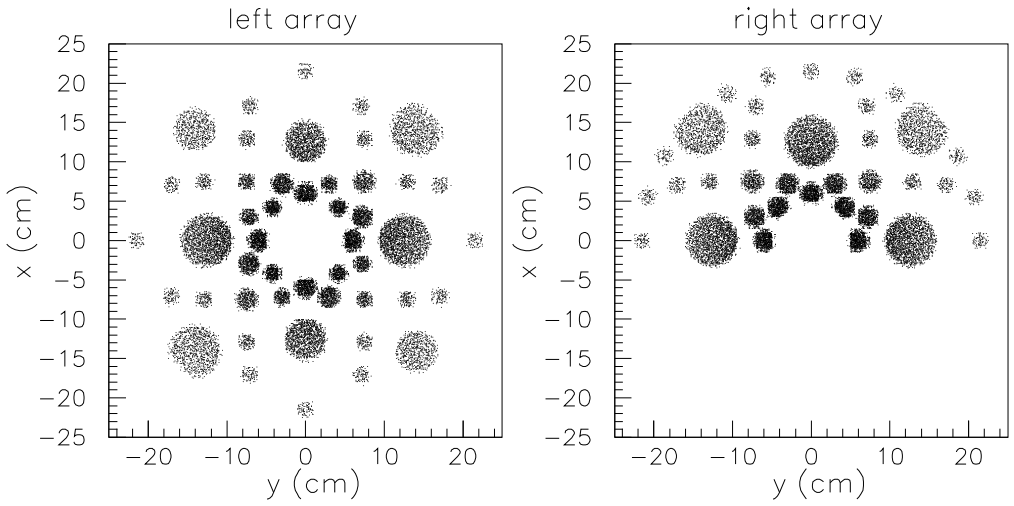

Figure 8.1: Schematic view of the two beam-beam counter arrays. The points represent charged particles striking the active area of the modules. Central Au+Au collisions from FRITIOF have been parameterized to simulate the hit density.

An estimate of the efficiency with which the combined array can provide a good

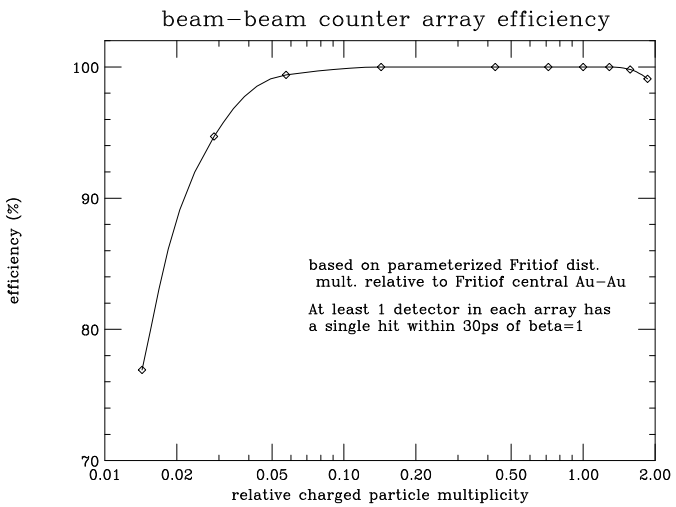

Figure 8.2: Efficiency of the beam-beam array to provide a good timing start as a function of relative multiplicity. Central Au+Au collisions from FRITIOF correspond to a relative multiplicity of 1.

timing start has been made. The charged particle distributions for Au+Au central collisions from FRITIOF have been parameterized. A module is considered to produce good timing if only one charged particle strikes the active area of the module and it arrives within 30 ps of the arrival time expected for $\beta = 1$. In addition, it is required that both arrays have at least one good timing hit. The efficiency as a function of the charged particle multiplicity relative to Au+Au central events of FRITIOF is presented in Fig. 8.2. The array is nearly 100% efficient for relative multiplicities of 0.05 to 1.6. The inefficiency at lower multiplicities is a consequence of the small number of counters and sparse sampling. The inefficiencies at large relative multiplicities is the result of all modules having multiple hits for some events. Backgrounds will produce spurious hits in the arrays which will increase the occupancy. Preliminary simulations using GEANT suggest that this will only modestly affect the efficiency. These simple simulations demonstrate that a sampling array can provide an efficient start-timing over a large range of multiplicities.

8.2 Centrality detector

As mentioned above, selecting on charged particle multiplicity as a measure of the centrality ("impact parameter") of collisions will be performed by the centrality detector. The goals for this detector may be briefly stated as:

1. To use the identical detector for all systems from peripheral Si+Si to central Au+Au.

2. To provide a first-level hardware trigger for the experiment.

3. To allow an offline analysis with as many as five centrality windows for Au+Au, and at least two such windows for Si+Si.

4. To provide azimuthal angle coverage as symmetric and as complete as possible without interfering with the spectrometers.

5. To cover as large a range of pseudorapidity as possible and yet remain within a reasonable budget.

These goals guide the design of the detector in ways that are outlined below.

Silicon strip detectors have been successfully operated as vertex detectors at collider experiments[1] and are being constructed as centrality detectors for both the PHOBOS and PHENIX Experiments at RHIC[2,3]. Following the development work of these collaborations, the incremental cost per channel of such detectors is expected to be quite low, allowing a suitable device to be built for a cost of less than $250,000. In addition, it is desirable for two or more RHIC experiments to have a common centrality trigger for the purpose of comparing results. Indeed, many of the goals for the low-resolution part of the PHOBOS vertex detector coincide with those outlined above. For these reasons, BRAHMS is planning to build a silicon strip barrel detector resembling the multiplicity vertex barrel of PHOBOS.

An alternate detector technology which is also lightweight and low-cost is that of a gas proportional counter with cathode pad readout. A backup plan for a multiplicity array based on this option is outlined in a separate section below.

8.2.1 Phase-space Coverage

The total charged particle multiplicity density, $dN/d\eta$, versus pseudorapidity, η, is shown in Fig. 8.3 for central Au+Au for the two models Fritiof and Venus. Note that the two-peaked distribution for Fritiof arises not from less nucleon "stopping" in the model – protons comprise only 6% of the total multiplicity – but rather from the difference between rapidity, y, and pseudorapidity, η. Due to the inequality, $|y| \leq |\eta|$, the $dN/d\eta$ distributions are broader than the corresponding ones for dN/dy. For both Fritiof and Venus, the *shape* of the $dN/d\eta$ distribution does not depend on the mass of the projectile nor on the centrality of the collision (except for the very peripheral case), so the following argument concerning the desired coverage is appropriate within the context of these models.

A reasonable criterion for the minimum pseudorapidity coverage is to insure that both peaks in the Fritiof distribution are included. This implies covering $|\eta| \leq 2.0$, as shown

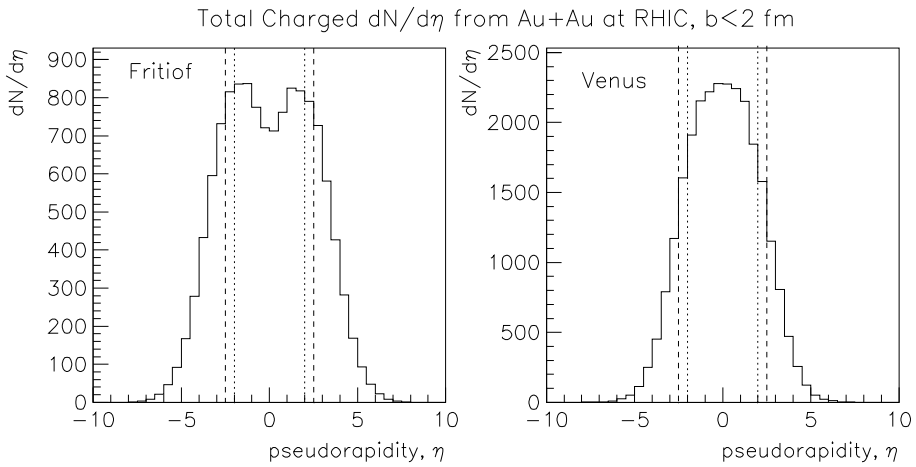

Figure 8.3: The total charged particle $dN/d\eta$ for central Au+Au. The dashed lines show coverage to ± 2.5 units of pseudorapidity, corresponding to the nominal coverage of the proposed detector; the dotted lines show the minimum coverage of ± 2.0 units.

by the dotted lines in Fig. 8.3. Note that the central peak in the Venus distribution is also well covered by this choice. For a barrel detector of radius 6 cm a pseudorapidity coverage of $|\eta| \leq 2.0$ implies a barrel length of 44 cm; however, a ± 15 cm vertex cut along the beam direction will be used in this experiment. This extra 30 cm brings the necessary total barrel length to 74 cm.

The coverage of the proposed silicon strip detector is shown in Fig. 8.4. Due to practical considerations regarding silicon wafer dimensions, the actual barrel length is 70.7 cm, implying a nominal coverage of $|\eta| \leq 2.47$ for an interaction at the diamond center. Interactions at the edge of the vertex cut give the extreme values η_{min}=1.94 and η_{max}=2.82 on opposite sides of the barrel. The barrel detector will be complemented by information from the beam-beam counters which nominally cover the pseudorapidity $3.0 \leq |\eta| \leq 4.5$.

To minimize the amount of material obscuring the apertures of the two BRAHMS spectrometers, gaps are allowed in the azimuthal coverage. As shown in the end view of Fig. 8.4, the octagonal cross-section for the barrel has six of the eight sides covered. Geant calculations with Venus central Au+Au events were used to estimate the background in the BRAHMS midrapidity spectrometer caused by the presence of the multiplicity detector silicon and associated electronics. With the spectrometer at 90°, less than one additional charged particle out of a total of 47 primary and secondary tracks was found to come from the multiplicity detector.

Figure 8.5 shows the predicted charged multiplicity distribution for a barrel detector of radius 6 cm, total length 70.7 cm and 3/4 of the azimuthal angle coverage. Effects of the vertex longitudinal position along the diamond are included, along with a ± 15

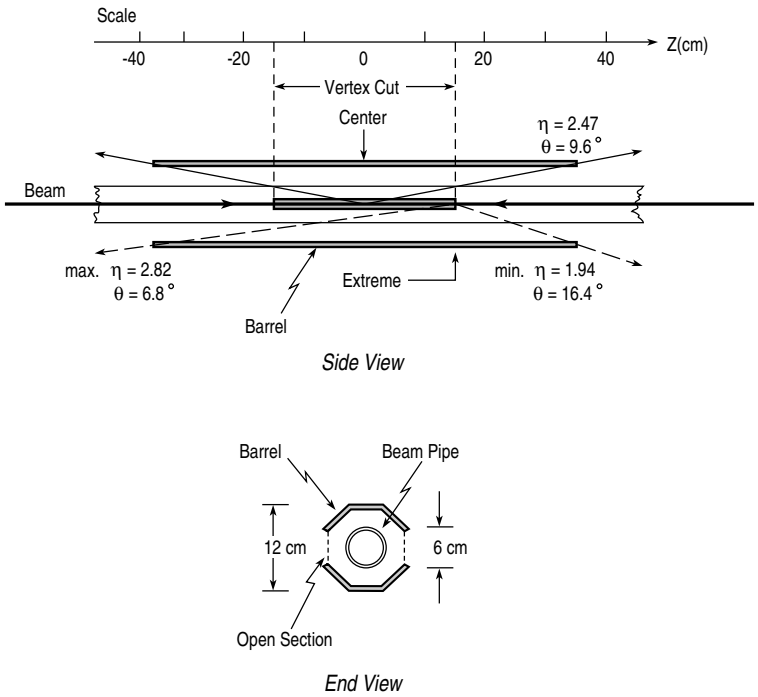

Figure 8.4: Coverage of the silicon strip multiplicity detector. The barrel has an octagonal cross-section of radius 6 cm, is 70.7 cm long, and is covered on six of the eight sides. An interaction vertex cut of ± 15 cm along the beam axis will be used.

cm vertex position cut. Since it is our goal to be able to use the identical detector for measuring centrality for all systems from peripheral Si+Si to central Au+Au, a dynamic range covering multiplicities with order of magnitude from 100 to 10000 is required, as seen in Fig. 8.5. In the Au+Au case, five multiplicity windows are required for the offline analysis: this requires a resolution in the determination of multiplicity of 10% or better. For the case of Si+Si, two cuts (central and peripheral) are quite satisfactory as this projectile system will be studied mainly as a contrast to Au+Au. A different centrality detector will be needed for both p+p and p+A running.

8.2.2 Concept for a Silicon Strip Detector

The layout of the silicon strip wafers on the multiplicity detector barrel is shown in Fig. 8.6. The octagon is composed of top and bottom halves with mechanical support provided by stands on the floor; for servicing the detector and/or the beampipe, the top half may be moved up and the bottom half down, and then both may be easily removed.

The wafers are identical with Wafer Type 8 of the PHOBOS Vertex Detector[2]. Each

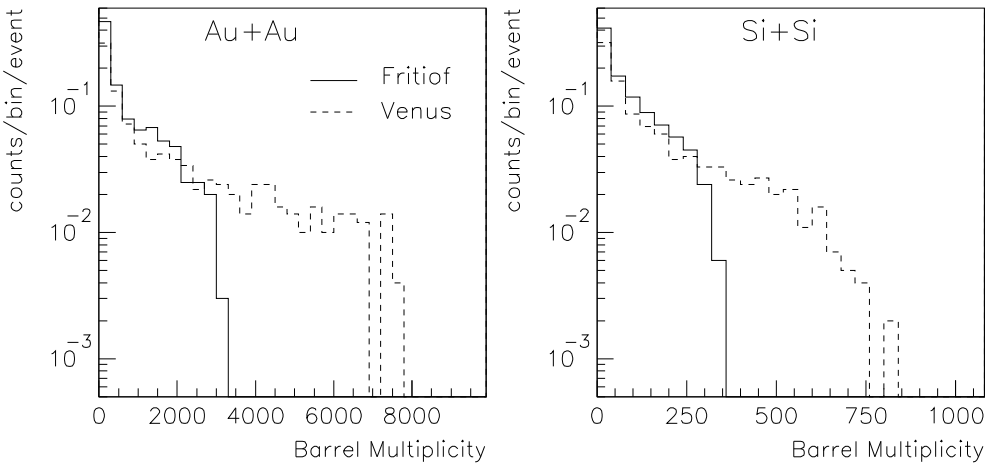

Figure 8.5: The true charged particle multiplicity distribution into a barrel with the coverage shown in Fig. 8.4, from Fritiof (solid histograms) and from Venus (dashed histograms.)

wafer is 78.6×48.8 mm^2 with an active area of 76.8×47.0 mm^2, and has 2 rows of 32 strips each (i.e., 64 strips/wafer.) Nine wafers cover the length of each side of the octagon; thus there are a total of (9 wafers/side)×(6 sides)× (64 channels/wafer) = 3456 channels. The wafer thickness is 300 μm and the strip pitch is 2.4 mm ($\Delta\eta \approx 0.05$.)

Since each silicon wafer has two sets of strips in the azimuthal direction, this implies an azimuthal segmentation of $\Delta\phi = 22.5^\circ$ per strip. Thus the detector system will only give limited information on charged particle distributions in the azimuthal angle ϕ.

Some multi-hit capability exists with these counters and the pulse height will be recorded. The total charge from each pad is read out with ADC's and the charged-particle multiplicity is deduced from the signal and the angle of the particle trajectory from the vertex through the Si plane. Although this procedure introduces some dispersion due to variations in energy loss of the charged-particles traversing the Si wafers, it yields a multiplicity measurement which does not saturate at high multiplicities.

Monte Carlo simulations were run to gauge the expected performance of this procedure for obtaining the multiplicity. Particles from model-generated events were "thrown" one by one at the actual detector geometry, and the energy deposited in the silicon was taken from the Landau distribution appropriate for the particle's mass, velocity and thickness of silicon traversed[4]. The high-energy end of the long Landau "tail" of the distribution is comprised almost entirely of delta electrons carrying energy of order 1 MeV, or greater, and these electrons generally escape the silicon without much energy loss. This fact is accounted for in the simulations by introducing a high-energy cutoff to the Landau distribution[5]. The total energy deposited in each silicon strip was then summed for each event, including the effects of individual particles crossing more than

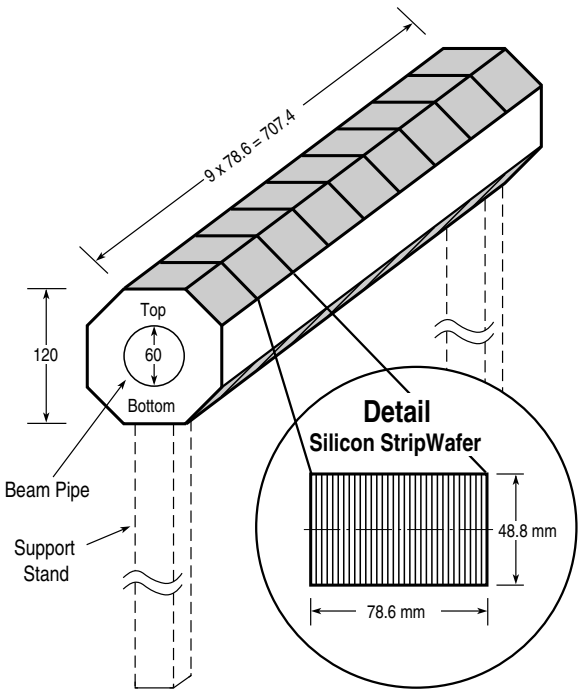

Figure 8.6: Layout of silicon wafers on the multiplicity detector barrel. Dimensions are in mm. Each wafer is 78.6×48.8 mm^2 with an active area of 76.8×47.0 mm^2.

one strip, and also including a random gaussian noise of 15 keV. (For comparison, a minimum-ionizing particle loses 116 keV in 300μm Si, on average.) In addition, a 50 keV threshold was applied for each channel. Finally, the number of particles hitting each strip was inferred, on average basis only, from the total energy deposited (in the strip) divided by the mean energy deposited per particle at that pseudorapidity. It should be noted that the mean energy deposited per particle is a model-dependent quantity which depends on the mixture of particle species produced as well as their momentum distribution.

The results of the Monte Carlo simulation described in the paragraph above are summarized in Fig. 8.7. Panel (a) plots the measured barrel multiplicity versus impact parameter for Fritiof Au+Au minimum bias events, showing the expected anti-correlation between the two quantities. In panel (b) is a histogram of the measured multiplicity for 100 trials of the same Fritiof central Au+Au event: the true charged particle multiplicity into the active barrel acceptance is 2725, whereas the mean measured value is only slightly higher at 2778. The r.m.s. width of the histogram is 22; i.e., less than 1% of the mean. Finally, panel (c) displays the measured $dN/d\eta$ for Au+Au central events from both Fritiof and Venus. The simulation with both models has been "tuned" for Fritiof in the sense that the mean energy deposited per particle (as a function of η) is derived

from that model; therefore it is not too surprising that the measured $dN/d\eta$ for Fritiof is nearly identical with the input distribution. However, the fact that the measured distribution for Venus agrees with its corresponding input to $\approx$5% provides confidence that the multiplicity measurement is valid in a less model-dependent manner.

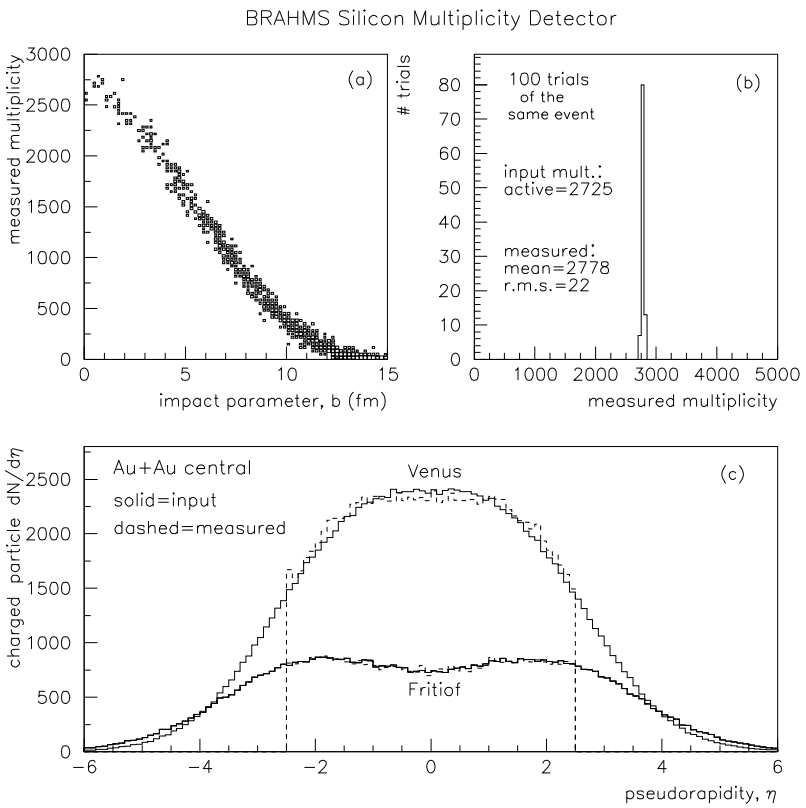

Figure 8.7: Simulated performance of the silicon strip multiplicity detector. Panel (a) shows the measured multiplicity versus impact parameter for Fritiof Au+Au events. Panel (b) shows the results of running the same Fritiof event through 100 trials. Panel (c) compares the measured $dN/d\eta$ for Au+Au central events to the inputs from both Venus and Fritiof.

The PHOBOS front-end electronics and readout, including the capability of forming an analog multiplicity trigger, would be used for BRAHMS with no changes.

The incremental cost of building this "copy" of the PHOBOS vertex detector is about \$240K.

8.2.3 The Backup Option: A Gas Proportional Counter

The option envisioned would be quite similar to the "Barrel-Section" of the Target Multiplicity Array (TMA) used successfully in E-802 at the AGS, with which members of BRAHMS have extensive experience. The basic counter element is a resistive plastic tube, 1×1 cm^2 in cross section, with a central anode wire stretched longitudinally. The gas-filled detector element is operated in the proportional mode. The particle-induced signals are read out from copper pads which form the segmented cathode plane. The read out electronics could be quite similar to that described for the original TMA, in which the barrel section had 1512 pads.

A suitable arrangement for BRAHMS would involve construction of a barrel of roughly twice the dimensions of Fig.8.4; i.e., 140 cm long and $\approx$12 cm in radius, which would cover the same range of η as illustrated. Each of the 6 flat detector planes would be comprised of 10 tubes cemented together: the length of the etched cathode pads would vary from $\approx$1 cm in the vertex region to $\approx$2-3 cm at the ends. As before, the two side sections would be open so as to not obscure the spectrometer views of the interaction diamond. The net ensemble could thus be configured to define, as desired, a segmentation range of 3000-6000 cells, and yet provide no greater scattering background than that for the silicon-strip detector described above.

With such a detector, the logic behind the determination of the experimental multiplicity is distinctly different from that of the original TMA. For TMA, the occupancy was kept low enough ($\leq$15%) such that the occurrence of multiple hits on a single element could be safely ignored. In the present case, although the occupancy is much higher, the true multiplicity may yet be determined under the assumption that the multi-hit probabilities follow pure Poisson statistics.

As an example of this approach, Fig. 8.8 summarizes the results of simple Monte Carlo calculations. For each trial, M particles were randomly thrown at $N = 5000$ channels, and from F_{hit} = fraction of channels with at least one hit, an estimate for M was deduced (M_{est}.) The mean value of F_{hit} from many trials is plotted in the figure versus the true multiplicity, M. For the multiplicity range relevant to this detector, $100 \leq M \leq 10000$, the relative r.m.s. error on the estimate, $\sigma(M_{est})/M$, is less than 1.5%. We conclude that the loss of resolution introduced by this estimating procedure, in distinction to any intrinsic detector resolution, is too small to be of concern.

8.2.4 Potential Upgrades

Possible future upgrades to the centrality detector include instrumenting more channels on the central barrel and adding endcaps to extend the pseudorapidity coverage. A separate centrality detector is necessary both for p+p and p+A running.

The more finely segmented wafers used by PHOBOS to make a precise determination of the interaction vertex ($<$ 1 mm) could also be employed for BRAHMS, albeit in a

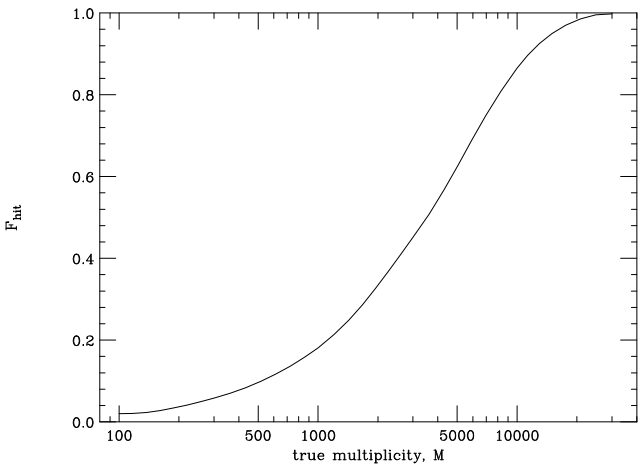

Figure 8.8: The mean fraction of channels with at least one hit as a function of the true multiplicity, M, in the acceptance of a "yes-no" detector with 5000 channels.

slightly different configuration. Two wafers, 78.6 mm $\times$ 39.8 mm^2 segmented into two rows of 0.3-mm strips, would be centered at a distance of 6 cm both above and below the beampipe. An array of 4 $\times$ 2 wafers of the same size, but segmented into single rows of 0.3-mm strips would be centered at a distance of 12 cm. The inner layer has a total of 1024 strips and the outer layer has a total of 2048. A precise determination of the interaction vertex will assist in a precise determination of the start-time, t_0, and in distinguishing primary tracks from secondaries in the mid-rapidity spectrometer.

8.3 References

1. For a recent review, see A.S. Schwarz, Phys. Rep. **238**, 1 (1994).
2. PHOBOS Conceptual Design Report, BNL, 1994.
3. PHENIX Conceptual Design Report, BNL, 1993.
4. A useful reference is W.R. Leo, *Techniques for Nuclear and Particle Physics Experiments*, Springer-Verlag, New York, second edition (1994).
5. The values for the cutoff derive from separate calculations which use the GEANT code. Empirically it is found that the maximum deposited energy, in keV, in 300 μm thick Si is given by $1200 + 160\eta^2$, where η is the pseudorapidity, with $|\eta| \leq 3$. This result holds whether the incident particle is a pion, kaon or proton.
6. T. Abbott, *et al.*, (E-802 Collaboration), Nucl. Instrum. Meth. **A290**, 41 (1990).

Chapter 9

Data Acquisition and Triggers

The data acquisition and trigger needs for BRAHMS are not expected to pose major technical challenges. Both can be fulfilled by a fairly conservative design.

9.1 Data Acquisition

The BRAHMS data acquisition is a UNIX/VME based system which will facilitate the readout and processing of data from various detector subsystems. It is planned to record $\approx$50 central events/sec and 200 spectrometer events/sec from all impact parameters. The data acquisition also provides for run control and control and monitoring of the operation of various detectors and related components.

The heart of the system consists of a VME processor element farm residing in several VME crates. Most of these processors are used for reading event fragments from front-end crates and have various interfaces to CAMAC, the front-end electronics (FEE) for the BRAHMS TPC's and centrality detector, and Fastbus. A VME crate is dedicated to monitoring and controlling various detectors and devices. To facilitate collection of various event fragments in parallel and to reduce VME traffic one processor is dedicated and directly interfaced to each CAMAC and Fastbus crate. Several processors will be interfaced to the centrality detector and TPC front-end electronics through high-speed optical fiber links for readout and zero-suppression. Several VME processors with SCSI-2 and ethernet interfaces perform event building, reformatting and data logging tasks.

Front End Electronics Interface

The front-end electronics for BRAHMS consist of CAMAC and Fastbus and are likely to use integrated electronics being developed for STAR or PHOBOS as well. FEE for the centrality detector for BRAHMS are likely to be an adaptation of similar FEE being developed for PHOBOS. The TPC read-out electronics cards which are being developed for STAR and similar cards being used in the NA49 Experiment are being considered for the TPC's in BRAHMS. These modules provide both timing and dE/dx information and have a relatively low incremental cost of production. It should be possible to modify and adapt these modules for the BRAHMS TPC's.

All front-end electronics are interfaced to VME and have dedicated VME-based intelligent controllers. We have developed intelligent VME interfaces to CAMAC as well as Fastbus which permit parallel readout of event fragments from various detectors for E866. These interfaces can be used in the current state or modified to accommodate higher event rates. The CAMAC interfaces consist of commercial VME processor boards equipped with memory-mapped interfaces to CAMAC crate controllers. The interface to Fastbus is through a VME slave interface to multiple Fastbus segment managers via fiber-optic links. The Fastbus interface could be modified to provide for multiplexed block transfer (MBLT) capability to enhance the VME data transfer rates.

The detectors proposed for BRAHMS consist of $\approx$15K channels, most of which have no hits in a typical event. The data from the TPC FEE constitute the majority of the raw data in BRAHMS. At a rate of 250 events/sec over 200 MB of raw data have to be processed per second. These data must be substantially reduced before logging. A VME interface to the TPC FEE will be designed. One VME processor module is dedicated for readout and zero-suppression of data from 16 FEE boards (512 channels). A daughter board interfaces directly to the processor module. This board interfaces with a control module via a fast optical link. The control module interfaces to 16 FEE boards and performs the readout of all boards once an event has been digitized. Zero-suppression and further reduction of data will be performed on the VME processor. Zero-suppression of the TPC data could in principle be performed, in earlier stages of readout, on the control module. This would however require a larger development effort and debugging time; also later enhancements would require major modifications, while a commercial processor board can easily be replaced with a more powerful processor. There may also be a need to develop VME interfaces to the FEE for the centrality detector if an appropriate interface is not available. The decision to develop such an interface will be made in the next year pending the final design of such interfaces by other collaborations.

DAQ Control and Software

The BRAHMS data acquisition is a UNIX/VME64 based system. All code for the host and the majority of the VME data acquisition code will be written in C/C++. Minimal amounts of code will be written in assembly language. The VxWorks real-time development environment will be used for the development of code running on VME

processors. SQL will be used for database access through RHIC computing facilities.

Motif graphical user interfaces (GUI) will be developed on UNIX workstations (e.g. SPARCstation 10) for DAQ run control and for monitoring and controlling various detectors. The majority of the code for the GUI will be generated using a commercial package such as Builder Xcessory. The host workstation is interfaced to VME modules over ethernet. Data acquisition on the VME crate could be centered around PowerPC (or ALPHA) based VME-resident CPUs with SCSI-2 and ethernet interfaces. Event building, reformatting, and tape logging will be performed on these processors. The present design can accommodate logging data to multiple tape drives via independent VME processors. However, data could also be sent to dedicated workstations via fast VME/(SBUS/PCI) buses for further processing and/or data logging. A small sample of data could be monitored by accessing the sample over the network: alternately fast dedicated links could be used to access a much larger sample which is especially useful in the initial debugging/setup stages of the experiment. VME processors with MBLT capability running the VxWorks real-time operating system will be employed in the DAQ system. VxWorks seems to be the best choice as a real-time VME development environment; it is the VME operating system most widely used in nuclear physics and HEP experiments and is used by EPICS. Another commercial real-time VME development environment, VRTX from Ready Systems, was considered but previous versions of VRTX have serious problems and support of this product is very limited.

Slow Controls

Unlike the present situation with AGS experiments, access to the experimental area and various detectors will be very limited during RHIC operation. There are a relatively large number of components that require monitoring and remote operation in BRAHMS. These include moving the spectrometers, setting and monitoring the magnets, setting and monitoring silicon voltage/current for the centrality detector, setting and monitoring various high voltages, monitoring and controlling the tracking detector gas flow, and generating alarms. BRAHMS, therefore, requires a reliable and flexible control system capable of handling a diverse set of interfaces. The EPICS control system satisfies our requirements and fits well with the overall DAQ design. Data acquisition, detector control, and monitoring of events and hardware form a distributed and integrated environment. One or more workstations can be used for run control, control of hardware and monitoring of various detector systems and data; this will be accomplished by implementing a client/server model with RPCs using TCP/IP.

Schedule

Due to the rapid progress in computer hardware the final selection of UNIX-based workstations, VME-resident CPU's, and tape drive technology will be delayed until 1997. The DAQ software development effort will begin when funding becomes available and should be complete and partially tested by 1998. All hardware prototypes will be built

by 1997 and tested by 1998. The development and testing of the control system will begin once funding is available and should be complete prior to the availability of major detector components. The completion of the DAQ system in a timely manner is only possible if enough funds (approximately one third of the cost for the DAQ) are incrementally available before 1997.

9.2 Triggers

The BRAHMS detector electronics and readout consists of both conventional TDC's and ADC's in CAMAC and Fastbus as well as integrated front end electronics for the TPC's and the centrality detector. Multiple trigger levels are required for BRAHMS.

The lowest level trigger (LVL0) will be formed by requiring a coincidence between signals from the RHIC clock and from the beam-beam counters located on opposite sides of the interaction point. This will be used to start the triggering system and the integrated electronics. The LVL0 trigger also constitutes a minimum-bias trigger for which a sample of events will be recorded.

The main first level trigger (LVL1) will also use the multiplicity detector, where several windows will select a range of reactions from peripheral to central collisions. This will also be used for measurements in the midrapidity spectrometer which, for Au+Au running, does not require a specialized trigger to obtain sufficient rates and statistics.

For the forward spectrometer, on the other hand, a track-selection trigger is needed for larger angles ($\theta > 5^\circ$) and/or non-central events. This can be formed by requiring hits in T3, T4, T5 and H2 as necessary conditions for identifying a track through the D3-D4 magnet system. More detailed studies are needed to determine if this will be sufficient to obtain the desired rates. The trigger could, e.g., be improved by correlating valid combinations of wire-hit positions in the different chambers, thereby suppressing background tracks which do not originate from the interaction region.

Future Plans

For running with lighter ions and protons it is desirable to have more refined spectrometer triggers. Two MWPC's are planned for inclusion in the midrapidity spectrometer trigger. The chambers will be mounted between the magnet and the TPCs. Their sizes will be 40 cm$\times$15 cm and 45 cm$\times$20 cm, respectively. Anode to anode wire spacing will be 0.5 cm. Each chamber will have two planes with different orientations in the x and y directions. Planes in y-direction can be used to form a trigger selecting particles from the collision diamond. When charged particles from the collision diamond go through the spectrometer, the positions of hit wires in the two chambers and the beam axis form a straight line. This condition can be programmed in a lookup-table as a LVL1

trigger. More elaborate triggers can be formed in LVL2 by utilizing information on time-of-flight, hit positions on the trigger chamber in the x-direction, and the vertex point from the beam-beam counters. From the above hit positions, a rough estimate of the momenta for the charged particles can be obtained. In combination with time-of-flight information, on-line particle identification is achievable for rare particle production, resonance production, and two-particle correlations at small relative momentum.

Chapter 10

Cost and Schedule

10.1 Cost

Presented here is a cost estimate for the construction of the BRAHMS Experiment. This includes the mechanical construction of magnets and platforms, the building of detectors and electronics, as well as other utilities needed for the experiment. The budget is first presented as an overview, followed by more details on the subcomponents, given on the following pages.

The budget summarized in Table 10.1 is given in thousands of FY94 dollars (i.e. present day value). In broad terms 30% of the budget is for the large magnets, power supplies, and installation of all components, 50% for the detectors and the remaining 20% for data acquisition, triggers, and control systems. The budget assumes an overall contingency of 25%; a reasonable number in line with that of the other RHIC experiments, particularly considering that most components have little development involved. A more detailed budget is presented in tabular form at the end of this chapter. Several comments concerning this is given in the following paragraphs, while others have been addressed in previous chapters.

The costs of the magnets are based on the engineering and design work which has taken place. The coils are based on an estimate from a vendor. The facilities and integration includes the platforms which are presently preliminary but is based on recent experience from the AGS. As discussed in Chapter 4, it is proposed to rebuild (modify) the power supplies obtained from LBL surplus. The cost of trays, cables and installation of all mechanical structures, utilities and detectors is based on fairly extensive work, which also gave the basis for an installation schedule discussed later. These estimates

BRAHMS SPECTROMETER BUDGET

Magnets & Platforms		**471**	
Tracking		**774**	
PID		**1139**	
Daq and triggerring		**720**	
Global Detectors		**393**	
Facility & Infrastructure		**1118**	
			4616
Contingency	25%		**1154**
Total			**5769**

Table 10.1: Requested budget for BRAHMS, in thousands of FY94 dollars.

are considered quite conservative.

The cost of the drift chambers is based on very recent construction for AGS Experiment 866, both for the mechanical and for the electronics part. The cost of TPC electronics, which includes preamps, shapers and readout systems, was estimated at \$50/channel. This assumes that the detectors utilize with only minor modifications the integral electronics developed for NA49 and presently under development for STAR. As discussed earlier the front end electronics are well suited for our detector; only the readout module following digitizing will have to be modified to handle an event rate of 200 per second.

The cost for the TOF system is based on current prices for the components used in E-802/E-866 based on a conventional design.

The global centrality detector is priced for the silicon detector option based on current incremental costs for silicon wafers and electronics using the PHOBOS design.

10.2 Schedule

At the present time a schedule for procurement, building of components, installation and testing has been outlined. This schedule will, for the larger components such as magnets, platforms etc., depend critically on the RHIC installation in the intersection

region. All the major components must be installed before the area is enclosed and RHIC commissioning begins. After that time only smaller detectors, controls, and electronics can be installed. Assuming that the commissioning will start 1/2 year before RHIC turns on in FY99, magnets must be installed on platforms and tested during FY98. It is estimated that procurement, production and delivery of coils and steel for the larger magnets D1-D4 will take two years implying that this must begin in FY96. The final engineering and design should thus start in FY95 and be completed in early FY96.

The schedule for detector components, DAQ and control systems requires that they will also have to be installed by end of FY98 such that only the final testing is left before turn on. The construction of these items need not begin before FY96/97, although development of prototypes and design will have to take place during FY95/96 for detector components, electronics and DAQ.

The effects of time scheduling have been incorporated in a requested budget profile for BRAHMS. In this request we have incorporated the desire of RHIC that the smaller experiments be funded late, but it has to be stressed again that funding in FY96 is crucial to have the experiment ready at RHIC turn on.

The requested funding profile, divided into the various subsystems, is given in Table 10.2.

Sub-system	FY95	FY96	FY97	FY98	FY99
Magnets	31	180	260	0	0
Power Supplies	0	150	213	0	0
Installation..	0	0	298	427	30
Tracking	0	80	311	383	0
PID	0	200	400	539	0
Global Det.	0	0	180	213	0
DAQ and trigger	60	40	100	360	180
BRAHMS total	91	650	1762	1922	210
Tot incl cont.	113	813	2203	2402	263

Table 10.2: BRAHMS funding profile for subsystems in thousands of FY94 dollars, excluding contingency. The last row gives the total requested per year including contingency

Magnets total			**471**
D1			**50**
	Steel	25	
	Coils	24.9	
D2			**98**
	Steel	58.4	
	Coils	39.6	
D3			**210**
	Steel	122.6	
	Coils	87	
D4			**28.1**
	Steel	28.1	
	Coils-use existing	0	
D5			**55**
	Steel	28.5	
	Coils	26.3	
Engineering & Design			**31**
Facilities & Integration			**1118**
Platforms			**198**
	Pivot	9.4	
	Front Platf.	44	
	Back Platf.	49.4	
	Midrap Platf.	30	
	Design	65	
Power Supplies			**363**
	Modification of LBL supplies	150	
	Trays,Cables	213	
Installation			**287**
Detector stands,Air Cond,Racks.			**150**
Control Systems			**80**
Detector Shielding (Pb/Heavy Met)			**40**

TRACKING					**774**
M-TPC1					**120**
	field cage			15	
	Readout Chamber			25	
	HighVoltage,Gas..			20	
	electronics	1200	$50	60	
M-TPC2					**100**
	mechanical			15	
	Readout Chamber			20	
	HighVoltage,Gas..			20	
	electronics	900	$50	45	
T1					**116**
	field cage			15	
	Readout Chamber			30	
	High Voltage,Gas..			20	
	electronics	1024	$50	51	
T2					**87**
	field cage			15	
	Readout Chamber			20	
	High Voltage,Gas..			20	
	electronics	640	$50	32	
T3,T4,T5					**311**
	mechanical	62	4	248	
	electronics	1050	$60	63	
T6					40

PID Forward & Midrapidity				**1139**
	channels	$/ch.		
TOF-midrapidity				**583**
	Tubes/electronics	450	1250	563
	Engineering Design			20
TOF-Forward				**170**
	H1	80	1250	100
	H2	40	1250	50

	Design,Eng.			20	
GasC-mid					**150**
	Electronics..	20	500	10	
	mechanical			120	
	Design,Eng.			20	
RICH					**183**
	4 tubes			88	
	Gas handling			25	
	Detector Box			20	
	Mirror			10	
	Design,Engineering			15	
	Readout Electronics			25	
Cherenkov (C1)					**53**
	mechanical,design			40	
	Gas handling			10	
	electronics	8	400	3.2	
Global Detectors					**393**
Centrality					243
	Silicon wafers	54	3000	162	
	Electronics	3456	12	41	
	Control			20	
	Design+mechanical			20	
Beam Beam counter					150
	Tubes, Electronics...			110	
	Design,mechanical			35	
DAQ & Triggering					**720**
	VME system			300	
	Level I+ II trigger			300	
	Workstations			120	

Appendix A

Prototype RICH Test Results

Key elements of the proposed RICH detector have been subjected to in-beam testing in RHIC RD44 using secondary beams at the AGS, and some pertinent results are reported here. Note that the multi-anode PMT used in these tests was the first version of its kind to meet the specifications of the Hamamatsu Corporation, upon which the expected performance criteria outlined in Sect. 7.4 are based.

A.1 The Multi-anode PMT

The R-4549-01 is a 20-stage 100-anode PMT based on a fine-mesh dynode structure, providing a current gain of 3×10^6 at a high voltage of HV = 2000 volts. The 10×10 cm^2 photocathode is bialkali: the segmented anode is a matrix array (10×10 = 100) of 9.5×9.5 mm^2 units with lemo outputs. With current gains of 10^6 - 2×10^7 (HV = 1800-2500 volts) the outputs will easily drive cable connections to appropriate ADC's. The high voltage is supplied by a single high-voltage cable: a built-in R/C dropping chain fixes the relative dynode voltages. A single output from the last dynode, representing essentially the "sum" of all anode currents, is available as a convenient gate.

The entrance window is of boro-silicate glass with the typical cutoff for wavelengths $\lambda < 300$ nm ($E > 4.1$ eV). The quantum efficiency response function is approximately Gaussian, with a peak sensitivity of 18%, centered at $E = 3.4$ eV and with FWHM = 1.8 eV. (The tails, however, fall off twice as fast as a true Gaussian.) As given in the above section on the RICH counter, the energy integral for the PMT efficiency is $\int \epsilon(E) dE = 0.33$ eV.

A.2 PMT Single-photon Response

Since the Čerenkov ring-image is composed of multiple hits of single photons, we were prompted to study the single-hit response. For this purpose, the R-4549 PMT was first mounted in a light-tight box. A collimated photon source, using a blue LED, was positioned a few cm away from the photocathode; the collimator opening was such as to illuminate only a single pixel at a time. The LED was pulsed by a driver whose intensity could be tuned low enough so that the collimator output was either 0 or 1 photon. (This tuning requirement was checked independently using a special RCA PMT with excellent single-photon resolution.) The data acquisition was triggered by the same signal which triggered the LED. The position dependence of the response is shown in Fig. A.1. The relative signal in each of three adjacent pixels is plotted for a run in which the position of the LED relative to the phototube was stepped in the y-direction. The FWHM of the response for an individual pixel is 10 mm with little cross-talk between neighboring pixels, as expected. In general, the pulse heights in neighboring pixels average only about 10% of that in the hit pixel.

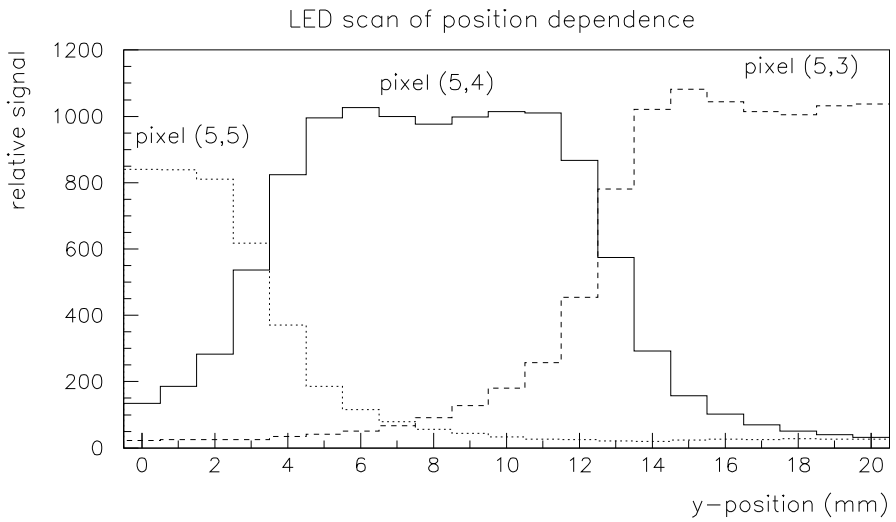

Figure A.1: Position dependence of the PMT pulse height in three adjacent pixels, measured as the position of an LED is stepped with respect to the phototube.

A.3 The Test Box

The test box is shown schematically in Fig. A.2. It was constructed from 1.9 cm thick aluminum plate, vacuum-welded at the box edges, with a removable top attached by 50

1/4-20 screws and sealed by a rubber gasket. The inner dimensions are $127\times64\times46$ cm^3. The particle beam enters via a 15 cm diameter mylar window of thickness 0.025 mm (shown on the left in the figure) and exits through an identical window at the output port.

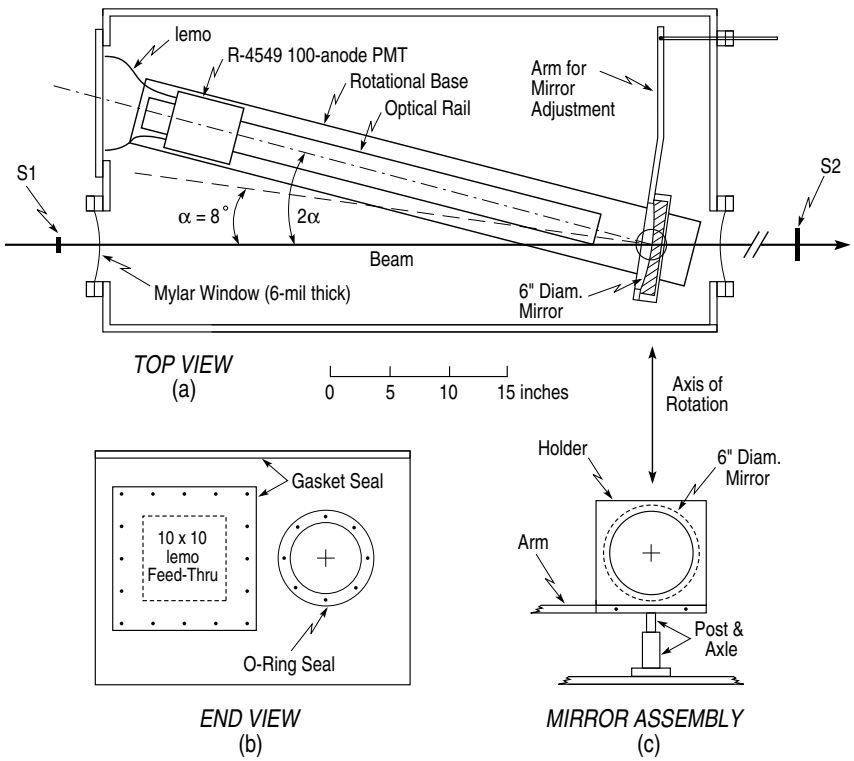

Figure A.2: Schematic view of the RICH test box. See text for details.

A 15 cm diameter mirror of multi-layer dielectric-coated aluminum with a focal length $f = 91$ cm is situated at a distance of $L = 114$ cm from the beam entrance, and is rotated by an angle $\alpha = 8^\circ$ relative to the beam direction, producing a ring image focussed at $2\alpha = 16^\circ$. The mirror was mounted in a frame attached to an axle which could be rotated about a vertical axis perpendicular to the beam direction. The mirror angle was controlled by a 0.6 cm steel rod which moved a 47 cm arm rigidly fixed to the mirror frame, so as to allow a mirror rotation over the range $-12^\circ < \alpha < +12^\circ$.

One hundred six Lemo signal cables are fed into the box using ordinary Lemo feed-throughs epoxyed into place to maintain a vacuum seal.

The device was aligned in the secondary test beam at the AGS, with the trigger defined by a 2×2 cm^2 scintillator, S1, just before the entrance window of the test vessel, and a larger scintillator paddle, S2, downstream of the exit window. Two drift chambers,

one in front of and one behind the test box, provided tracking for determining the particle trajectory, and hence measured the expected position of the center of the RICH ring to better than 1 mm in both the x and y directions.

A.4 Gas Handling System

The gas-handling system used in filling the RICH chamber with fluorocarbons is shown in Fig. A.3. The procedure adopted utilizes the fact that the radiator gases Freon-12 (122) and C_4F_{10} (238) have molecular weights (given in parentheses) much heavier than air (29) or argon (39). For example, consider the case where the RICH chamber has been initially filled with argon. The C_4F_{10} is set to flow slowly into the bottom of the vessel, while the output mixture (Ar + C_4F_{10}) is sent through a cooled recovery tank where the C_4F_{10} is liqified while the argon passes out the exhaust. The differing molecular weights (factor of 6) result in a density gradient in the RICH vessel, such that if the flow is slow enough (non-turbulent) the volume slowly becomes enriched in C_4F_{10}. The procedure can be continued until the supply in tank A is exhausted. In our case we manually switched the two tanks A and B and repeated the cycle using the C_4F_{10} previously recovered in B. Three such cycles yielded a gas mix of approximately 90% purity in C_4F_{10}.

In order to recover the C_4F_{10} at the conclusion of the experiment, a pump was used to reverse the flow direction – as indicated by the dashed lines in Fig. A.3. As the C_4F_{10} is recovered into B, the observed pressure drop in the chamber is compensated by adding argon to maintain a pressure differential of < 0.15 atm.

In principle, one can install a remote-controlled switching system to actuate the controlling valves, so as to alternate the designated funtion of the supply and recovery tanks. This would allow an extended period of automatic cycling, leading to a nearly 100% purity of C_4F_{10}, or by reversing the cycle, a complete recovery of the fluorocarbon.

A.5 In-Beam Testing

Figure A.4 presents results measured with the beam tuned for negative 12 GeV/c particles — predominantly pions — and a gas mixture in the test box of Freon-12 and N_2. Panel (a) shows the pulse height for each phototube pixel, summed over approximately 1100 events. The drawn ring is the best fit of the data to a circle. Figure A.4b is a histogram of the ADC pulse height in pixel (3,8), which lies directly on the ring. The corresponding histogram from neighboring pixel (3,9), which is not on the ring, is shown in Fig. A.4c; clearly the cross-talk between adjacent pixels is small, although not completely negligible.

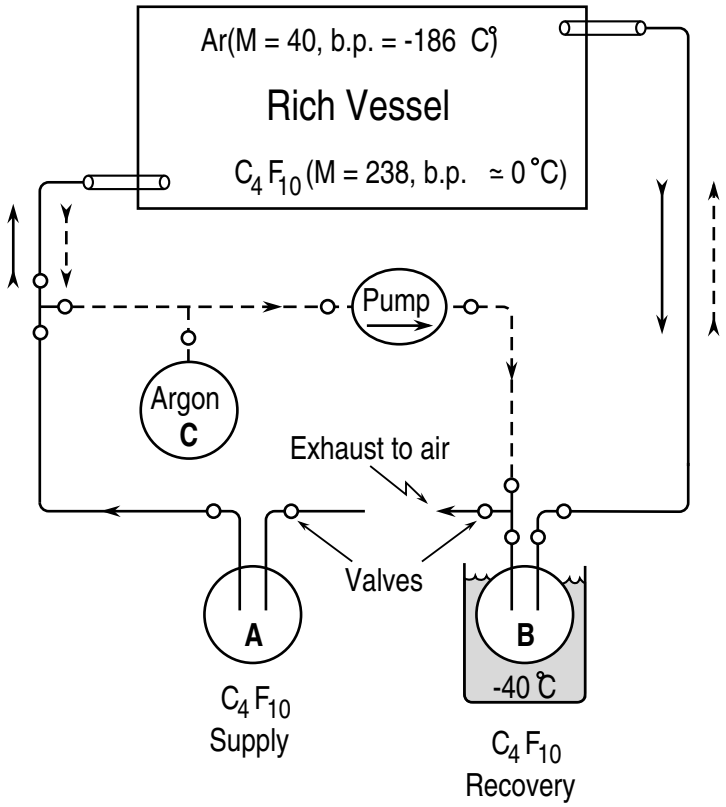

Figure A.3: Schematic flow-diagram for gas-handling system. Solid lines are for initial filling with the fluorocarbon; dashed lines (note reversed direction) are for final recovery of the fluorocarbon gas. With this system, the pressure in the RICH vessel can be kept within $< 10\%$ of atmospheric over both the filling and recovery operations.

The ability of the counter to identify individual particles is demonstrated in Fig. A.5. Panels a, b and c show individual events from a run where the beam momentum was tuned to 3 GeV/c and the box contained a C_4F_{10}-Ar mixture. The drawn rings show the best fits to circles constrained by the positions of the ring center (shown as the small star symbols) given independently by the drift chamber tracking. The ring radius from all events in the run is histogrammed in Fig. A.5d where three distinct peaks, identified with π^-, μ^- and e^-, are clearly observed. The peaks are well described as gaussian in shape; for the rings which are fully saturated in radius (electrons) the resolution of the radius determination is $\sigma_r/r = 2.3\%$.

A momentum scan was performed with a C_4F_{10}-Ar mixture in the vessel during a period in which the ratio of the gases did not change. The ring radius is plotted versus momentum in Fig. A.6, which shows saturated light production from electrons, as well as the excitation curves for muons, pions and kaons. The saturated radius for

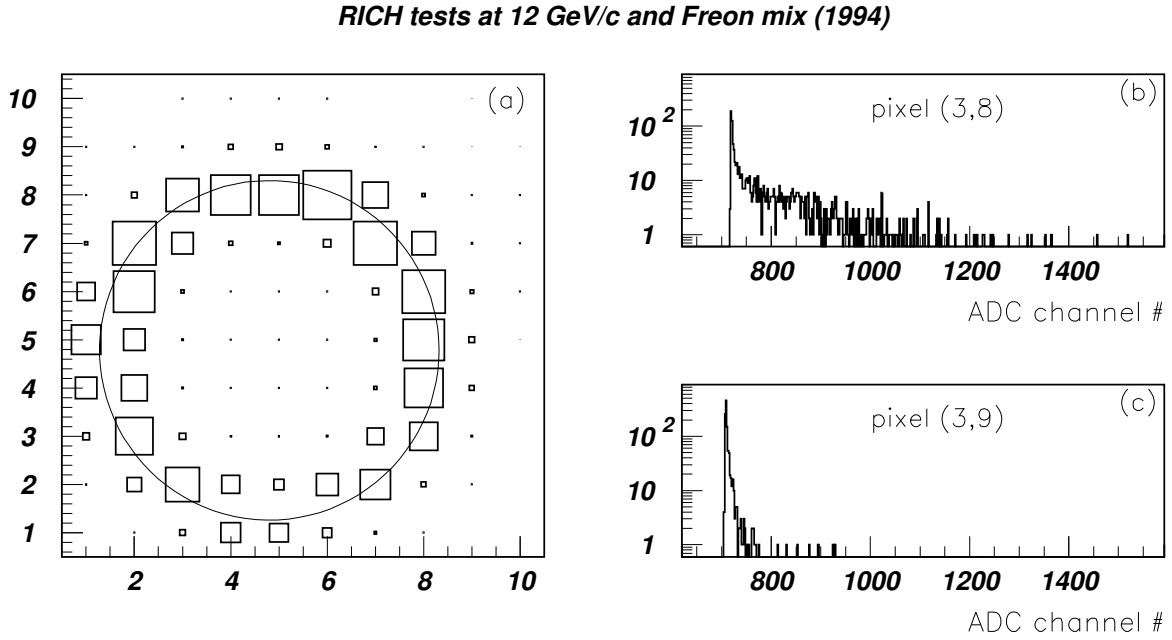

Figure A.4: Results from the prototype RICH counter with test beam at 12 GeV/c and a Freon gas mixture. Panel a shows a ring image from approximately 1100 events and panels b and c show the ADC pulse height spectra from two individual pixels. See text for details.

electrons implies an index of refraction n=1.00113, shown as the horizontal line through the electron points. (This includes a 3% correction to the radius to account for the fact that the position of phototube was for practical reasons slightly out of the focal plane.) The excitation curves predicted by this index of refraction are shown as the solid curves; the shaded regions represent a ±5% systematic uncertainty in the absolute momentum scale. The measured values of the radius all lie within the shaded regions. From n=1.00113 it is inferred that the fraction of C_4F_{10} in the vessel was approximately 75%. Later runs following further filling of the vessel achieved approximately 90% C_4F_{10}.

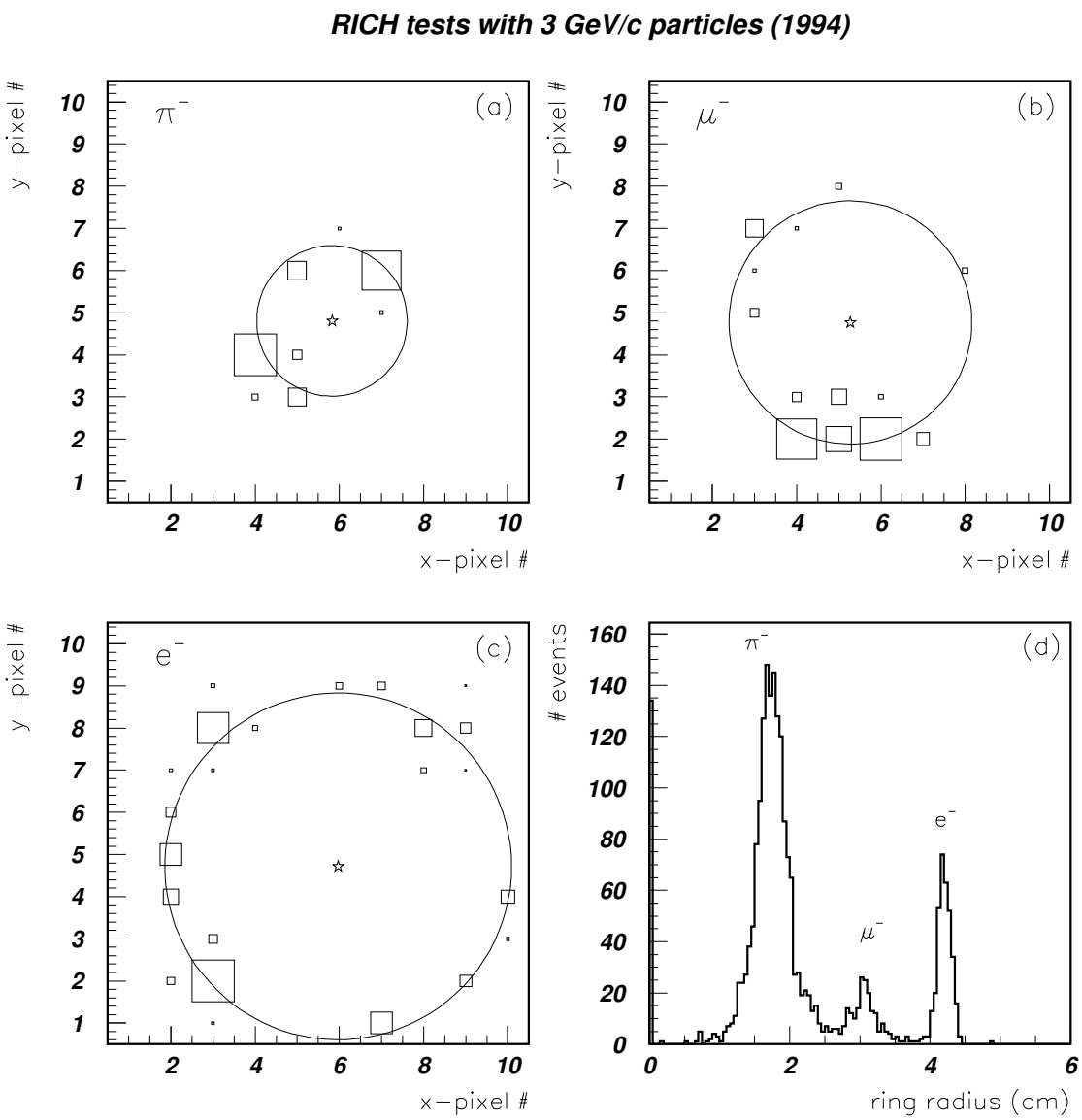

Figure A.5: Results from the prototype RICH counter with test beam at 3 GeV/c and a C_4F_{10}-Ar gas mixture. Panels a, b and c show individual events with fitted rings; the ring centers are shown as stars and come from independent drift chamber tracking. Panel d is a histogram of the fitted ring radius from the entire run, showing peaks identified as π^-, μ^- and e^-.

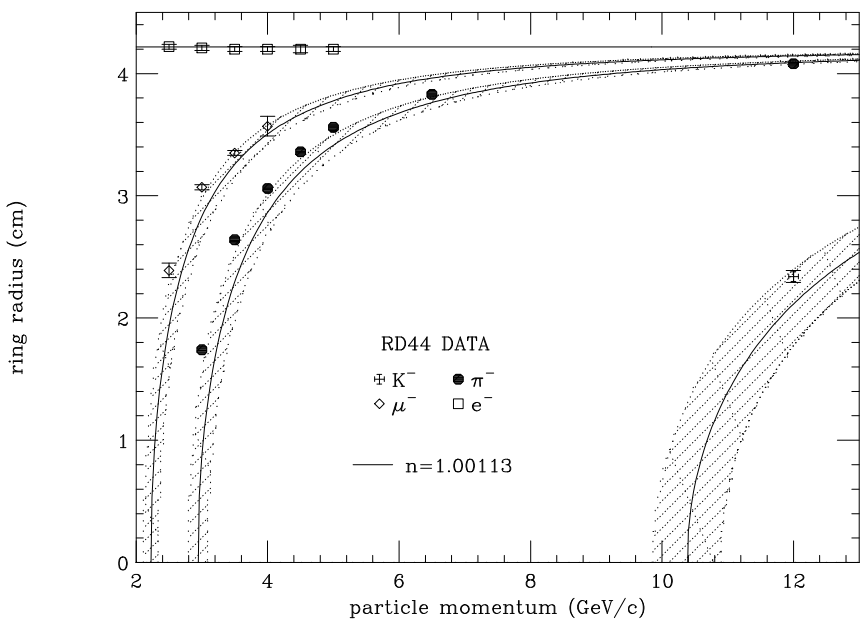

Figure A.6: The mean radius from event-by-event fits to rings in the prototype RICH counter filled with a C_4F_{10}-Ar gas mixture, for different particle species. The solid curves show the expected radii for an index of refraction of $n = 1.00113$; the shaded regions represent a 5% systematic uncertainty in the absolute momentum scale.

Appendix B

Simulation programs

The simulations for BRAHMS are carried out using a package built on the GEANT program library from CERN. It has been the goal to deal with the different detector components in a common and modular manner. By design, detector and magnet configuration and parameters can be changed with ease. The present version uses the 3.21 version of the library. The description of most detectors is quite simple. The tracking detectors are given as simple gaseous volumes and the TOF detectors as scintillator slats. Thus none of the supporting structures are included. These will in most cases not have a direct view to the collision point and are not expected to have any significant influence on the simulation results obtained so far.

The input to the simulations have mainly been "data" from the event generators FRITIOF and VENUS. The predicted multiplicities from the two models are quite different (see, e.g., Reference 1) underlining the uncertainty in the particle densities with which the RHIC detectors must deal. The collaboration has chosen to use mainly the VENUS input since it represents the more difficult situation for the detectors.

The output from the simulations are used to investigate background sources, rates, etc. by a fairly simple analysis. This is the method used for most tables of background properties in the report.

Alternately the output was used as input to the track reconstruction program SONATA developed for the forward spectrometer. The Entity-Relation model is used to describe the data structures for detectors, hits, tracks, etc. It is implemented using the ADAMO[2] package. The use of this methodology makes modifications to detector descriptions and data structures easy and safe to deal with. Briefly, this program digitizes the tracks going through the detectors T1-T5, reconstructs track segments from the drift chamber wire-information or the TPC-pad ADC and time information. It then connects track segments from T3, T4, and T5 to determine the momenta of the tracks, projects these

back to T2, and to the interaction point. The configuration of a given detector, e.g. number of wire planes, wire distances in T5 can be easily modified, a feature which is used to optimize the performance of the detector.

References

1. F. Videbaek, M. Ye, T. Throwe, T. Ludlam, RHIC/Detector Note-2, BNL, 1992.

2. S.M. Fisher, The ADAMO Data System, CERN/RAL, 1992.

Appendix C

Rate Estimates

In order to estimate the time needed to obtain a complete data set for one combination of colliding beams at one energy the following requirements were defined to obtain high quality spectra of pions, kaons, protons, and antiprotons. The goal, as established earlier, is to measure to p_t of at least 1.5 GeV/c where possible. We require to have in each 40 MeV/c bin of p_t 400 kaons per angle setting. This is roughly equivalent to observing 5000 pions in each bin following the model predictions. Also, since emphasis is put on the most central collisions, a 5% trigger is employed. For the Forward Angle Spectrometer the momentum bites are such that the entire range can be covered in about 7 settings for each angle . For the high momentum bite, which is most crucial for the rate estimates, the spectrometer accepts about 1° in polar angle.

In Table C.1 the estimated times for central Au+Au at $\sqrt{s}$ = 200 GeV per nucleon pair based on the FRITIOF predictions for pions are shown. The VENUS prediction would give similar times at the most forward angles and somewhat shorter times at the larger angles. Summed over angle and both magnetic field polarities it is estimated that a complete distribution can be obtained in ≈3200 hours. This is very much dependent on the highest p_t to be measured. If the p_t range at the angles from 5° and backward was limited to p_t(max) = 1.5 GeV/c the time is reduced by 50%. It is envisioned that less central and peripheral collision spectra can be measured concurrently with the centrally triggered events; the time required for minimum bias running is estimated to be approximately 5 times that for central triggers. An average luminosity of 4 $fm^{-2}s^{-1}$ was used for the rate estimate.

With regard to the midrapidity spectrometer the polar range of 30°-90° can be covered in 8 angle settings each with two different field settings and two polarities. A measurement of spectra up to p_t ≈1.4 GeV/c requires 270,000 events (including a correction for K^+ decay), which will take ≈2 hours per angle and polarity setting. The

Angle (deg.)	$(p_t)_{max}$ GeV/c	p_{max} GeV/c	Events/sec/40 MeV per collision at p_{max}	Time (hrs) at p_{max}	Total time (hrs) This angle
3 (1)	1.30	25	0.0135	10	16
5 (1)	2.00	23	0.005	60	100
10 (1)	2.00	11.5	0.0004	90	140
15 (2)	2.00	7.32	0.00001	200	300

Table C.1: Counting rates in the Forward Angle Spectrometer. The numbers in parentheses are the angular openings, in degrees, assumed.

inclusive measurement can then be done in ≈64 hours. To cover up to p_t ≈2.0 GeV/c, 2.1 million events are needed corresponding to ≈ 15 hours for the high field settings. The total survey for one beam-beam combination can be done in ≃360 hours. The time at 90° to acquire 100,000 K^+ pairs for a correlation measurement is ≃200 hours, while at 30° 10 hours suffice. These estimates assume that the p_t spectra are binned in 20 MeV/c bins below 1.4 GeV/c and 50 MeV/c bins up to 2 GeV/c. The bins in rapidity are 0.2 units wide.

List of Figures

2.1 Net baryons from central Au+Au collisions 10
2.2 dn/dy for π^+ and K^+ in central Au+Au collisions 11
2.3 $d^2n/dpd\theta$ for several angle settings in central Au+Au collisions 13
2.4 Two-pion correlation function 14
2.5 Two-kaon correlation function 15
2.6 Distributions in (y,p_t) space of accepted ϕ mesons 16
2.7 The expected invariant mass distributions of K^+K^- pairs 17

3.1 Layout of the BRAHMS spectrometers 20
3.2 Acceptance of BRAMS spectrometers 22

4.1 Layout of the 4 o'clock area. 30
4.2 Steel design for D5. 31
4.3 Coil design for D5. 32
4.4 Field across the gap in D1. 33
4.5 Fringe field in D1. 33
4.6 Vertical field in D1. 34

5.1 Detail of BRAHMS at the 4 O'clock area. 38
5.2 Bird's eye view of BRAHMS at the 4 O'clock area. 39
5.3 Beam pipe profile for the BRAHMS intersection region 40
5.4 Layout of BRAHMS at the 2 O'clock area. 43

6.1 Variance due to multiple scattering over 4 meters of air. 47
6.2 Reconstructed momentum resolution, target position distributions for 10 GeV/c pions with an assumed position resolution of 200 μm 48
6.3 Top view of shielding for T2 51
6.4 T4 layout 53
6.5 Charged particle densities in TPC1 and TOFW 54
6.6 Hit multiplicities in TPC1, TPC2 and TOFW 55
6.7 Longitudinal and transverse diffusion constants for various gas mixtures as a function of drift field. 56

6.8 Schematic view of the pad-readout TPC. 57
6.9 Typical geometry of the anode wires and pad rows with clusters. 59
6.10 TPC readout electronics used by ALEPH and NA35. 60
6.11 Illustration of the steps used in track finding and reconstruction. 65

7.1 Schematic view of the C1 Čerenkov counter. 71
7.2 Pion acceptance in the midrapidity and forward arms 72
7.3 K/p separation in the midrapidity and forward arms 72
7.4 Arrangement for mid-rapidity TOF wall staves. 74
7.5 Schematic outline of RICH detector 78
7.6 Ring radius and number of photoelectrons vs. momentum 80
7.7 Typical RICH detector ring patterns 83
7.8 Position of the ring centers for particles in RICH detector 84

8.1 Schematic view of the two beam-beam counter arrays. 86
8.2 Beam-beam array efficiency 87
8.3 Charged particle $dN/d\eta$ for central Au+Au collisions 89
8.4 Coverage of the silicon strip multiplicity detector 90
8.5 True charged multiplicity distribution into the centrality detector 91
8.6 Layout of silicon wafers on the multiplicity detector barrel. 92
8.7 Simulated performance of the silicon strip multiplicity detector. 93
8.8 Fraction of channels hit versus multiplicity 95

A.1 Position dependence of PMT pulse height from an LED scan 110
A.2 Schematic view of the RICH test box. 111
A.3 Schematic flow-diagram for gas-handling system 113
A.4 Prototype RICH counter results with a Freon gas mixture 114
A.5 Prototype RICH counter results with 3 GeV/c particles 115
A.6 Ring radius versus momentum from the prototype RICH counter 116

List of Tables

4.1 Magnet parameters 29

6.1 Variance due to multiple scattering 48
6.2 Expected charged particle multiplicities for the 7.5-15 GeV/c setting at 2.1°. 49
6.3 Expected charged particle multiplicities for the 15-30 GeV/c setting at 2.1°. 49
6.4 Expected charged particle multiplicities for the 2-5 GeV/c setting at 2.1°. 50
6.5 Effect of shielding on rates in T1, T2 and H1 50
6.6 Detector characteristics for the forward arm components. 52
6.7 Average charged particle multiplicities in the midrapidity spectrometer. . 55
6.8 TPC parameters for the present prototype. 63

7.1 Performance of the various TOF detectors 70
7.2 Characteristics of different phototubes for the TOF. 75
7.3 Average charged particle hits in the RICH detector 77

10.1 Budget summary 104
10.2 Funding profile for subsystems 105

C.1 Counting rates in the Forward Angle Spectrometer 120